

ALMA MATER STUDIORUM
UNIVERSITA' DI BOLOGNA

SCHOOL OF ENGINEERING

- Forlì campus -

SECOND CYCLE MASTER'S DEGREE in AEROSPACE
ENGINEERING

Class LM-20

GRADUATION THESIS in Experimental Methods in Aerodynamics

Development and Validation of a Mathematical Model for a Monotube Automotive Damper

CANDIDATE:
Rithvik Magal

SUPERVISOR:
Dr. Gabriele Bellani

Academic year 2019/2020

Abstract

Automotive dampers involve complex flow physics that cannot be fully described by analytical models derived from first principles. Therefore, the development of a mathematical model based on semi-empirical laws that accurately describe the influence of each of the many design features would greatly help the design and optimization of automotive dampers. This thesis aims to develop a computationally efficient mathematical model capable to predicting damper performance with reasonable accuracy.

Lumped parameter mathematical models were developed and implemented using the MATLAB and Simulink environments. In order to solve for the structural dynamics of the shim stack, a force method based analytical model was developed. In order to solve for the internal flow field, fluid structure interaction simulations were necessitated due to the inherent coupling of fluid and structural dynamics.

Fluid-Structure Interaction (FSI) simulations were attempted using an open source setup consisting of OpenFOAM and CalculiX coupled by the preCICE coupling library. Coupled simulations on a trial simplified geometry produced physically consistent results. FSI simulations could not be performed on the real geometry due to lack of time and computational resources. The discharge coefficients were modelled as a linear function on the basis of CFD simulations performed on outputs from the force method model.

In order to validate the MATLAB mathematical model, experiments were carried out on a test automotive damper on a suspension dynamometer. The model showed good agreement in with experimental data at low bleed valve openings. The model accuracy was observed decrease for larger bleed valve openings due to unavailability of accurate model coefficients.

Acknowledgements

Being passionate about automobiles since childhood, it gave me great pleasure to work on this thesis. This thesis concludes my studies at Università di Bologna. I believe I have made good strides as an engineer and as a person and it would not be possible if not for the support of a lot of people.

Firstly, I would like to thank my supervisor: Dr. Gabriele Bellani. I thank you for giving me the freedom to explore my own ideas while being available to guide me. My apologies for the last minute submissions and bailouts.

I greatly thank Mr. Giuseppe Andreani, Mr. Tommaso Noccioli and Mr. Matteo Gaia at the Andreani Group for facilitating my experiments and providing me the opportunity to get hands-on experience with automotive dampers.

I consider myself very fortunate to have a cousin like Chirag, who basically lived the thesis with me, helping me throughout and making sure I was working well. I consider myself equally fortunate to be friends with Alvaro, who gave me free reign over his home/office space.

I sincerely thank my colleagues who have lent me their technical expertise - Pietro Basile, Luca Franceschelli, Darshan Kadijah, Ilaria Gatti and Simone Melchiorre.

I am grateful to my friends Adithya, Mukesh, Vivek, Aurelia and Guillaume (merci for the surprise Belgian chocolate eggs) for supporting me and for keeping me moving forward.

Last but not least, I thank my parents, grandparents and brother for always supporting my dreams. They gave me all their love and support even at times when I was too consumed with the thesis to reciprocate and I wouldn't be carrying out this thesis without them.

Contents

List of Tables	ix
List of Figures	x
1 Introduction	1
1.1 Automotive dampers	2
1.2 Thesis Objectives	4
1.3 Thesis outline	5
2 Damper Physics	6
2.1 Valving	6
2.1.1 Valve Types	6
2.1.2 Valve Performance	7
2.1.3 Valve Configuration	8
2.1.4 Role of Valve Friction	8
2.2 Fluid Dynamics of Damper Oils	8
2.2.1 Damper Oils - An Introduction	8
2.2.2 Multiphase Considerations	9
2.2.3 Compressibility Considerations	11
3 Damper Modelling	12
3.1 Overview of mathematical models	13
3.1.1 Damper Oil	13
3.1.2 Piston Dynamics	13
3.1.3 Pressure Dynamics	14
3.1.4 Flow Rates	15
3.1.5 Shim stack model	17
3.2 Model Coefficients	21
4 Implementation of the Mathematical Model	22
4.1 Software for modelling and Simulation	22
4.1.1 MATLAB	22
4.1.2 Simulink	22
4.2 MATLAB Scripts	23
4.2.1 MATLAB scripts for the Simulink model	23
4.2.2 MATLAB model	24
4.3 Simulink Model	24
4.3.1 Gas Piston Dynamics	25
4.3.2 Pressure blocks	25

4.3.3	Flow Rate blocks	26
4.3.4	Damping Force Computation	28
5	Numerical Analysis - An Introduction	29
5.1	Overview of Numerical Methods	29
5.2	Finite Element Methods	29
5.3	Computational Fluid Dynamics	30
5.4	Fluid Structure Interaction	30
5.4.1	Classes of FSI solvers	30
5.5	Performance of FSI Solvers	31
5.5.1	Performance of Monolithic Solvers	31
5.5.2	Performance of Partitioned Solvers	33
6	FSI Simulations - Setup	35
6.1	Geometry	35
6.2	The Solvers	36
6.2.1	OpenFOAM	36
6.2.2	CalculiX	37
6.2.3	preCICE	37
6.3	Mesh Convergence Studies	41
6.3.1	Geometry	41
6.3.2	Mesh Generation	42
6.3.3	Boundary Conditions	43
6.3.4	Solver Setup	43
6.3.5	Convergence Criterion	43
6.3.6	Results	44
6.3.7	Analysis	48
6.3.8	Conclusions	53
6.4	FSI trials using a simple geometry	54
6.4.1	Mesh	55
6.4.2	Simulation Setup	56
6.4.3	Coupling Setup	56
6.4.4	Results	57
6.5	FSI Trials on Real Geometry	62
7	Experimental Trials	64
7.1	Trial Damper	64
7.2	Experimental Setup	66
7.3	Data Acquisition Scheme	67
7.4	Data Points	67
8	Results	69
8.1	Mathematical Sub-Models	69
8.1.1	Shim Valve Discharge Coefficient	69
8.1.2	Shim Stack Displacement Model	71
8.2	Experimental Results	74
8.3	Simulink Model Results	75
8.3.1	Model Output	75
8.3.2	Comments on Simulink Model Results	77
8.4	MATLAB Model Results	77

CONTENTS

8.4.1	Model Output	77
8.4.2	Sensitivity Analysis	81
8.4.3	Results of Numerical Simulations of the Tests	86
8.5	Comparison of Experimental Results with Mathematical Model	90
8.5.1	Force-Velocity Plots	90
8.5.2	Analysis	95
9	Conclusions and Recommendations	96
9.1	Conclusions	96
9.2	Recommendations	97
	Bibliography	98

List of Tables

6.1	Details of meshes used for mesh convergence studies	42
6.2	Mesh convergence - volumetric flow rate results	44
6.3	Mesh convergence simulation times - 2 cores and 4 cores	44
7.1	Damper Valving Specification	65
8.1	Discharge coefficient look-up table for compression stroke	70
8.2	Discharge coefficient look-up table for rebound stroke	70
8.3	Equivalent Shim Stack Stiffnesses	73
8.4	Model coefficients used in numerical simulations of the tests	90

List of Figures

1.1	Cut section view of a typical automotive damper	3
2.1	Disc valve	6
2.2	Rod valve	6
2.3	Spool valve	7
2.4	Shim valve	7
3.1	Schematic of a generic monotube damper. Source: Talbott and Starkey [1] . .	12
3.2	Schematic of the displacements a generic shim stack. Source: Skačkauskas et al. [2]	18
3.3	Computational scheme of a shim stack. Source: Talbott and Starkey [1]	19
4.1	Simulink model of a generic automotive damper	24
4.2	Gas Piston Dynamics Block	25
4.3	Compression chamber Pressure Dynamics Block	25
4.4	Bleed Orifice Volumetric Flow Rate Block	26
4.5	Piston Seal Leakage Volumetric Flow Rate Block	27
4.6	Damping Force Computation Block	28
6.1	CAD assembly of the monotube damper	35
6.2	CAD assembly of the 1/8 th section of the monotube damper	36
6.3	An overview of the coupling between a fluid dynamics (CFD) solver and a structural mechanics (CSM) solver using preCICE. Source: Chourdakis [3] . .	37
6.4	Serial explicit coupling scheme Source: Chourdakis [3]	38
6.5	Parallel explicit coupling scheme Source: Chourdakis [3]	38
6.7	Parallel implicit coupling scheme Source: Chourdakis [3]	39
6.6	Serial implicit coupling scheme Source: Chourdakis [3]	39
6.8	Solver sub-cycling scheme Source: Chourdakis [3]	39
6.9	Consistent mapping scheme in preCICE Source: Chourdakis [3]	40
6.10	Conservative mapping scheme in preCICE Source: Chourdakis [3]	40
6.11	CAD assembly of the modified configuration with offset shim stacks	41
6.12	Details of generated mesh with an element size of 0.2 mm	42
6.13	Streamlines for mesh with element length of 0.2 mm	45
6.14	Streamlines for mesh with element length of 0.25 mm	45
6.15	Streamlines for mesh with element length of 0.3 mm	46
6.16	Streamlines for mesh with element length of 0.35 mm	46
6.17	Streamlines for mesh with element length of 0.4 mm	47
6.18	Streamlines for mesh with element length of 0.45 mm	47
6.19	Streamlines for mesh with element length of 0.5 mm	48
6.20	Error on imposed volumetric flow rate with mesh density	49

LIST OF FIGURES

6.21	Difference in averaged inlet pressure relative to finest mesh with mesh density	50
6.22	Ratio of Volumetric Flow Rates (C/R) with mesh density	51
6.23	Ratio of Averaged Pressures (C/R) with mesh density	52
6.24	Simulation time vs. number of cores	53
6.25	Geometry used for trial FSI simulations	54
6.26	Fluid mesh used for trial FSI simulations	55
6.27	Solid mesh used for trial FSI simulations	55
6.28	Fluid solver residuals for the trial FSI simulation	57
6.29	Structural solver residuals for the trial FSI simulation	58
6.30	Coupled solution at $t=1 \times 10^{-9}$ s	59
6.31	Coupled solution at $t=3 \times 10^{-6}$ s	59
6.32	Coupled solution at $t=3.5 \times 10^{-6}$ s	60
6.33	Coupled solution at $t=4 \times 10^{-6}$ s	60
6.34	Coupled solution at $t=4.5 \times 10^{-6}$ s	61
6.35	Coupled solution at $t=5 \times 10^{-6}$ s	61
6.36	Coupled solution at $t=5.5 \times 10^{-6}$ s	62
7.1	Test automotive monotube damper	64
7.2	Main Piston of the test damper	65
7.3	Test damper mounted on the UK4kw suspension dynamometer	66
7.4	Umbria Kinetics DynoSoft software graphical user interface	67
8.1	Streamlines obtained for a 10 MPa pressure differential using Force method predicted shim deflection	70
8.2	Shim deflections of the compression and rebound stack computed using the Force method vs. applied pressure difference	71
8.3	log-log plot of shim deflections of the compression and rebound stack computed using the Force method vs. applied pressure difference	72
8.4	Deflected compression shim stack shape for a pressure differential of 10 MPa as predicted by the Force method	73
8.5	Experimental Force-Velocity graph	74
8.6	Experimental Displacement-Force graph in the case of fully closed bleed valve	74
8.7	Main piston displacement, velocity, acceleration and velocity-based stroke detection flag for oscillation at 100 Hz	75
8.8	Shim valve volumetric flow rate vs main piston velocity for oscillation at 100 Hz	75
8.9	Force histories for oscillation at 100 Hz	76
8.10	Force - Displacement plot for oscillation at 100 Hz	76
8.11	Displacement History for sinusoidal input of 25 Hz	77
8.12	Velocity History for sinusoidal input of 25 Hz	78
8.13	Damping Force vs. Piston Velocity for a sinusoidal input of 25 Hz	78
8.14	Damping Force vs. Piston Displacement for a sinusoidal input of 25 Hz	79
8.15	Volumetric Flow Rates vs. Piston Velocity for a sinusoidal input of 25 Hz	79
8.16	Pressures vs. Piston Velocity for a sinusoidal input of 25 Hz	80
8.17	Damping Force vs. Velocity plot for the Baseline configuration used for sensitivity analysis	81
8.18	Damping Force vs. Velocity plots for sensitivity analysis of Opening Radius for Opening radius = 10 mm–16 mm for both shim stacks	82
8.19	Damping Force vs. Velocity plots for sensitivity analysis of Initial Gas Chamber Pressure for Initial Gas Chamber Pressure = 10 bar–20 bar	83

LIST OF FIGURES

8.20 Damping Force vs. Velocity plots for sensitivity analysis of Shim Valve Discharge Coefficient for $C_D = 0.5-1.0$ 84

8.21 Damping Force vs. Velocity plots for sensitivity analysis of Shim Stack Stiffness for factors of 0.5x - 1.5x applied to the stiffness obtained from the force method 85

8.22 Force - Velocity curves for numerical simulations of the test points 86

8.23 Force - Displacement curves for Bleed Fully Closed 87

8.24 Force - Displacement curves for Bleed at 1 click 87

8.25 Force - Displacement curves for Bleed at 5 clicks 88

8.26 Force - Displacement curves for Bleed at 10 clicks 88

8.27 Force - Displacement curves for Bleed at 20 clicks 89

8.28 Force - Displacement curves for Bleed Fully Open 89

8.29 Comparison of Force - Velocity curves from experiment and the developed mathematical model for Bleed Fully Closed 90

8.30 Comparison of Force - Velocity curves from experiment and the developed mathematical model for Bleed at 1 click 91

8.31 Comparison of Force - Velocity curves from experiment and the developed mathematical model for Bleed at 3 clicks 91

8.32 Comparison of Force - Velocity curves from experiment and the developed mathematical model for Bleed at 5 clicks 92

8.33 Comparison of Force - Velocity curves from experiment and the developed mathematical model for Bleed at 10 clicks 92

8.34 Comparison of Force - Velocity curves from experiment and the developed mathematical model for Bleed at 15 clicks 93

8.35 Comparison of Force - Velocity curves from experiment and the developed mathematical model for Bleed at 20 clicks 93

8.36 Comparison of Force - Velocity curves from experiment and the developed mathematical model for Bleed Fully Open 94

8.37 Comparison of Gas Chamber Pressure for Bleed Fully Closed 94

Nomenclature

Abbreviations

ALE	Arbitrary Lagrangian-Eulerian
CFD	Computational Fluid Dynamics
CHT	Conjugate Heat Transfer
FEA	Finite Element Analysis
FEM	Finite Element Method
FSI	Fluid Structure Interaction
ODE	Ordinary Differential Equation
OpenFOAM	Open Field Operation and Manipulation
preCICE	Precise Code Interaction Coupling Environment
WRC	World Rally Championship

Greek symbols

α	Coefficient of volumetric expansion
γ	Gas adiabatic constant
μ	Dynamic viscosity
ρ	Density

Notations

A_c	Area of the compression chamber
A_O	Area of the piston orifice
a_p	Acceleration of the main piston
A_S	Total cross sectional area of the piston orifices
A_{gp}	Area of the gas piston
a_{gp}	Acceleration of the gas piston
A_{rod}	Area of the piston rod
C_D	Drag coefficient
$C_{D_{bleed}}$	Discharge coefficient of the bleed orifice
$C_{D_{orifice}}$	Discharge coefficient of the piston orifice

NOMENCLATURE

$C_{D_{valve}}$	Discharge coefficient of the shim valve
C_{GA}	Gas absorption coefficient
D_b	Diameter of the bleed orifice
D_v	Diameter of the largest shim in the stack
E_0	Activation energy of the molecule
F_{fric}	Friction force
g	Gravitational acceleration
H_g	Initial height of the gas chamber
$H_{c_{ini}}$	Initial height of the compression chamber
$H_{r_{ini}}$	Initial height of the rebound chamber
k_{shim}	Stiffness of the shim stack
m_{GA}	Mass of gas
m_{gp}	Mass of the gas piston
N_{Bo}	Bond number
P_c	Pressure in the compression chamber
P_G	Partial pressure of the gas above the liquid
P_g	Pressure in the gas chamber
P_r	Pressure in the rebound chamber
$P_{g_{ini}}$	Initial pressure of the gas chamber
P_{surf}	Pressure at the surface of the shim valve
U_B	Rising speed
V_L	Volume of liquid
V_p	Velocity of the main piston
V_{gp}	Velocity of the gas piston
x_p	Displacement of the main piston
x_{gp}	Displacement of the gas piston
y_{shim}	Shim deflection
Re	Reynolds number
E	Bulk modulus of the damper oil

1

Introduction

Automotive dampers, or shock-absorbers as they are commonly referred to as, are found in all automobiles; from tiny three-wheeled "tuk-tuks" to purpose built race cars. From the earliest versions of the leaf spring suspension setup used on horse-drawn carriages in the mid-nineteenth century (C. Dixon [4]) to modern electronically controlled road-adaptive suspension setups, dampers have been crucial in ensuring safety and comfort. The stringency of this requirement is ever increasing with the rapid pace of development of internal combustion engines, leading to higher attainable speeds.

Dampers that perform well put a smile on the driver's face. This statement is as valid for a road-going average person looking to transport their family in comfort as it is to a Formula 1 or WRC driver looking to extract all the performance their vehicle is capable of providing. For an engineer, developing a damper optimal to a particular application is technically challenging and equally rewarding, more so if the damper in question plays a role in obtaining a successful result in competition.

In addition to the technical challenges, the design, development and production of dampers is an economically lucrative business. The estimated production numbers for automotive dampers worldwide is 50–100 million units per year with total retail value in excess of US \$1 billion per annum (C. Dixon [4]). Hence, there is great value for manufacturers in decreasing development costs; especially considering that for the most part, damper internals are developed and tuned "by feel" of experienced technicians and drivers/riders. The internal mechanism which produces the damping force is very complex and involves a strong interaction of the damper oil and flexible valves. These interactions are difficult to be characterised experimentally. Hence, until recently, not many attempts were made to produce simple models to mimic the complex internal fluid flow. With the recent advent of Fluid Structure Interaction (FSI) simulations, it is now possible to investigate the complex internal phenomena without the penalty of outrageous cost or equipment. Furthermore, automotive dampers experience a wide range of excitation velocities, ranging from 1 mm/s to 1 m/s for a competition off-road vehicle. It is not feasible to develop experimental setups to mimic such extreme velocities. Therefore, development of simple models that can predict damper behaviour with reasonable accuracy while being capable of running on a personal computer in a matter of minutes is hence a very welcome tool for damper manufacturers.

In addition to predicting damper performance without the need of producing a physical part, mathematical models and numerical simulations allow the study of the basic fluid and structural dynamic phenomena that take place inside dampers. This knowledge is essential for development of new and innovative valve designs. Also, quantifying

parameters related to the internal phenomena allows for development of dampers for a specified damping behaviour - an iterative, time consuming and costly process when done by experimental trial and error.

The scope of a mathematical model for dampers goes beyond just the design and development of the dampers themselves. The development of automobiles in general has greatly benefited from mathematical models and simulation tools. Much like the isolated case of dampers, vehicle performance and dynamic behaviour can be determined before designing a single part. To do so, however, requires a robust mathematical model for damper behaviour. This problem is more prominent in recent times with autonomous mobility considered as the future of transport. Autonomous driving is achieved using electronic feedback control systems relying on vehicle dynamic models that need to be computed in real-time with on-board processors. In order to develop safe autonomous vehicles, it is necessary for the vehicle dynamics to be modelled with a high degree of accuracy. Such a high fidelity vehicle dynamic model relies heavily on the fidelity of the damper model itself, creating a demand for accurate but computationally minimal models for damper dynamics.

1.1 Automotive dampers

The purpose of automotive dampers is to dissipate energy of the sprung and unsprung masses in the vertical direction. Vertical motion in automobiles is a result of body heave, pitch and roll and wheel hop (C. Dixon [4]). The most commonly used type of damper in production automobiles is the passive telescopic type, owing to its simple design and low manufacturing and maintenance costs. The telescopic damper consists of a hydraulic cylinder containing a piston through which fluid is forced to flow through restricted outlets and valve systems, generating hydraulic resistance and consequently converting kinetic energy into thermal energy [5]. A cut-section of a typical automotive damper is shown below in Fig.1.1

1.1. AUTOMOTIVE DAMPERS



Figure 1.1: Cut section view of a typical automotive damper

As the oil flows through orifices, it experiences a pressure loss due to throttling. This differential pressure is directly proportional to the damping force experienced by the piston (Satpute et al. [6]). In order to tune the damping force, shim valves are commonly used in automotive dampers. Shim valves are essentially elastic thin plates that cover

the orifices made in the piston. At low piston speeds, the deflection in the shim valve is low, and consequently a high damping force is obtained. As piston speeds increase, fluid pressure forces the shim to deflect further, producing a progressively larger flow area and controlled progression of the shocks damping force [7]. This model can be further extended by incorporating multiple shims stacked together, called shim stacks, to obtain a high level of control on the damping characteristics at every piston velocity.

It can now be appreciated that a high-fidelity numerical model of the transient behaviour of shim stacks and the consequent flow field is absolutely necessary in order to obtain accurate numerical models for the damping characteristics of automotive dampers.

To this end, multiple lumped parameter models have been proposed. One of the earliest works was a nonlinear parametric model by Reybrouck [8]. The mathematical model was expanded with the inclusion of a shim stack structural model by Talbott and Starkey [1]. Talbott's work was expanded upon by multiple researchers, such as Rhoades [9]. Talbott's model is mathematically simple, computationally inexpensive and has proven to be accurate by Rhoades [9] and Talbott and Starkey [1]. However, this model being a non-linear algebraic system, does not provide information of the transient processes in a damper. Skačkauskas et al. [2] proposed a dynamic model based on a coupled system of ODEs capable of modelling damper dynamics such as hysteresis. This model along with Talbott's model were major references for the formulation of the mathematical model in this thesis work.

All the models described above utilise constant model coefficients. The physics of dampers, however, are complicated in nature and in order to accurately model internal flow phenomenon, it is necessary to study both the fluid dynamics of the oil flow as well as the structural dynamics of shim valves. Such a work was performed by Nilsson [10] by performing Fluid-Structure Interaction (FSI) simulations on a spring-loaded check valve using the ANSYS multiphysics software package [11]. The goal of this thesis is to extend the application to more structurally complex shim stacks and in addition, to use open source software to do so. FSI simulations will afford a look into the intricacies of damper physics that are difficult to be modelled analytically and impractical to measure experimentally, thus enhancing the capabilities of analytical models with the implementation of dynamic model coefficients.

1.2 Thesis Objectives

The following were set as objectives for this thesis work:

- Study of the fundamental physics behind damper operation and performance
- Review existing mathematical models relating to damper physics
- Implementation of a mathematical model using the MATLAB and Simulink environment
- Perform experiments with a test damper to study correlation with the mathematical model

1.3 Thesis outline

This study is divided into nine chapters starting with the introduction, each of which focuses on a particular theme:

Chapter 2 : The fundamental physics of an automotive damper are presented in this chapter.

Chapter 3 : This chapter details the mathematical models required to model damper physics.

Chapter 4 : The details of the implementation of a lumped parameter model using MATLAB and Simulink is provided in this chapter.

Chapter 5 : This section provides an overview of numerical simulations to model structural, fluid and combined fluid-structural interaction dynamics.

Chapter 6 : This chapter provides complete detail of the solvers and setup for the fluid-structure interaction simulations carried out.

Chapter 7 : The experimental setup and data acquisition method are provided in this chapter.

Chapter 8 : The experimental results are presented and the validity of the lumped parameter model is evaluated against experimental data.

Chapter 9 : The conclusions and recommendations for future work, based on the results obtained during this thesis will be detailed in this chapter.

2

Damper Physics

Typical mono-tube automotive dampers provide damping forces that are highly dependent on the interactions between the damper oil and orifices built into the piston. During the rebound stroke, the oil above the piston is forced to flow downwards through a system of orifices and the oil experiences a pressure drop. Similarly, during the compression stroke, oil below the piston is made to flow upwards (Reybrouck [8]). The damping force provided by the damper is strongly related to the pressure differential between the top and bottom surfaces on the piston and the oil flow rate through the orifices. The oil flow rate, however, is dependent on piston velocity, which in turn is dictated by the damping force. Hence, it is of paramount importance to study the flow of oil through orifices in order to develop methods to accurately evaluate the steady and transient pressure field within the damper.

2.1 Valving

2.1.1 Valve Types

Commonly found types of valves in automotive dampers include - disc valves, rod valves, spool valves and shim valves (C. Dixon [4]). Schematics of these basic valves are illustrated in figures 2.1, 2.2, 2.3 and 2.4.

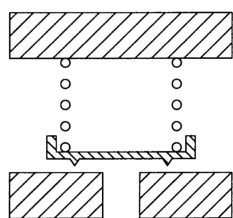


Figure 2.1: Disc valve

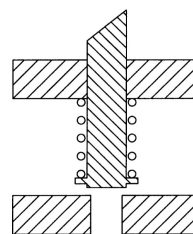


Figure 2.2: Rod valve

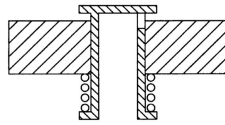


Figure 2.3: Spool valve

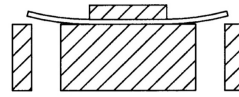


Figure 2.4: Shim valve

Disc valves

These valves consist of a simple disc with a coil spring. The valve is closed until an opening pressure difference is reached. The flow area is the disc circumference times the lift height. The valve behaviour can be tailored by varying the spring preload and spring stiffness. Practically, it is difficult to implement a progressive dynamic and disc valves are instead used as blow-off valves with a constant pressure characteristic (C. Dixon [4]).

Rod valves

In order to obtain a progressive pressure drop utilising a disc-type valve, a small circumference is mandatory, giving rise to the rod valve. Utilising the smallest hole permissible by manufacturing limits, a greater valve life and hence, a more progressive dynamic can be achieved. To increase the lift even further, a tapered rod may be used. Tapering solves the problem of achieving less effective flow area due to the exit area being equal to the hole area (C. Dixon [4]).

Spool valves

Spool Valves The spool or bobbin valve offers higher flexibility in pressure characteristics by designing the exit hole with a suitable profile to provide flow area varying with spool position. For example, a linear flow rate vs. pressure difference dynamic can be obtained by designing the flow area to increase with the square root of the opening length (C. Dixon [4]).

Shim valves

Shim valves or packs of shims are used with varying diameters because the damping characteristics can be changed and tailored easily. This is crucial for racing dampers. Shim stacks consist of up to 6 shims of decreasing diameters. Valve opening heights are fractions of millimeters, rendering the flow path to be quasi-bidimensional (C. Dixon [4]).

2.1.2 Valve Performance

Apart from the valve area-pressure relationship and the pressure-flow rate relationship, the following parameters are vital in assessing valve performance (C. Dixon [4]):

- Steady state pressure-flow rate
- Friction and hysteresis
- Transient response (flutter, overshoot)
- Temperature sensitivity
- Cavitation
- Wear
- Fatigue
- Consistency in production
- Required manufacturing precision
- Economy of production

2.1.3 Valve Configuration

In a real valve, the variable-area component will be combined with an orifice in parallel to give some flow even with the valve fully closed. Also, the valve will somehow be limited in maximum area, or a series orifice will be provided to control the flow at very high pressures (C. Dixon [4]).

2.1.4 Role of Valve Friction

For an ideal valve with no mechanical friction, there will be a unique pressure for a given flow rate, at least under steady flow conditions. For valves with moderate friction, mechanical friction does not pose problems and can in fact aid valve operation by preventing valve overshoot or valve oscillation due to positional instability. With high friction, however, for a given pressure or flow rate, the valve position is indeterminate within the friction band, depending strongly on recent operating history, i.e whether pressure was increasing or decreasing. Hence, valve friction is one of the causes of hysteresis and is additionally associated with valve wear (C. Dixon [4]).

2.2 Fluid Dynamics of Damper Oils

2.2.1 Damper Oils - An Introduction

Damper oil is generally a light mineral or synthetic oil with reduced change in viscosity with temperature with typical density of 850 kg/m^3 – 860 kg/m^3 and viscosity between 5 mPas – 100 mPas (Reybrouck [8]). Both the density and viscosity generally depend strongly on temperature. Viscosity is beneficial for lubrication but is detrimental to damping. Usage of low viscosity oils, however, is difficult since they are prone to cavitation due to higher vapour pressure. The compressibility of pure oil is very low $0.05 \text{ \%}/\text{MPa}$, but

practically, compressibility is higher due to absorbed gas and bubbles. However, damper oils can be considered incompressible without significant loss of accuracy in analysis. Damper oils are expected to function over a broad temperature range from -40°C – 130°C . Reduced damping force has been observed at high temperatures, which has been attributed due to change in both the density and the viscosity of the oil. Although the temperature rise has a higher effect on viscosity compared to density, the consequences of the density change are equally important. Oil temperature may also be influenced by the mounting environment of the damper, eg. presence of radiators, etc (C. Dixon [4]). A typical damper oil has a molecular weight of 350 kg/kmol and a molecular volume of approximately 0.676 nm^3 . The chemical formula is approximately $\text{C}_{25}\text{H}_{52}$ (C. Dixon [4]).

2.2.2 Multiphase Considerations

Absorption and Desorption

The amount of gas that can be absorbed in a liquid depends on the chemical affinity between the gas and the liquid. For non reacting materials, the maximum absorbable mass of gas m_{GA} can be modelled linearly by Henry's Law (C. Dixon [4]):

$$m_{GA} = C_{GA} \cdot V_L \cdot P_G \quad (2.1)$$

Where C_{GA} is the gas absorption coefficient, V_L is the volume of the liquid and P_G is the partial pressure of the gas above the liquid. The solubility reduces rapidly with temperature. For air in mineral oil, the absorption coefficient is about $1\text{ kg}/(\text{m}^3\text{ MPa})$. On absorption, the resultant mass and volume of the mixture may be determined as:

$$m_L = m_{L0} + m_{GA} \quad (2.2)$$

$$V_L = V_{L0} - \frac{V_{L0}}{K_L} \cdot P + \frac{C_{GLV} \cdot C_{GA} \cdot V_{L0}^2}{m_{L0}} \quad (2.3)$$

Where C_{GLV} is the gas absorption volume coefficient and is of the order of 1.0. It may be observed that the increase of volume due to gas absorption roughly offsets the reduction of volume due to compressibility of the liquid phase. This is exactly the case under the following condition:

$$C_{GLV} = \frac{\rho_{L0}}{K_L \cdot C_{GA}} \approx 1 \quad (2.4)$$

The time required for absorption is dependent on the area of the liquid surface exposed to the gas. If the liquid near the gas becomes saturated, agitation of the liquid will promote absorption by transporting unsaturated fluid to the interface. Absorption reduces the mass of free gas and has a significant effect on the density and compressibility of an emulsion. When the pressure is reduced, the solubility limit may fall below the actual absorbed gas mass. The initial configuration of a supersaturated solution. The surplus gas may exit the solution, causing cavitation issues. However, there might not be an energetically favourable route for the desorption to occur and the process may be delayed. If a

few gas molecules form a bubble, the high internal pressure due to surface tension would be sufficient to cause reabsorption. Desorption depends largely on nucleation points to provide an energetically favourable route to adequately sized bubbles (C. Dixon [4]).

Emulsification and Demulsification

Emulsions are combinations of two liquids that do not blend uniformly at the molecular level, in which one of the liquids is divided into very fine droplets suspended fairly uniformly in the other liquid. A mixture of finely dispersed gas bubbles may be regarded as an emulsion if the size of the bubbles is very small. However, in order to be considered an emulsion, the gas must not be absorbed by the liquid (C. Dixon [4]). If the volume of gas greatly exceeds that of the liquid, the emulsion is considered to be a foam/froth. This is best avoided because the emulsion compressibility inhibits the generation of chamber pressures and a drastic reduction in damping force is observed, especially for short strokes. Moderate emulsification, however, may be beneficial to ride quality, providing stroke sensitivity in an effect similar to rubber bushes (C. Dixon [4]). The four principal sources of bubbles in a damper are - boiling, cavitation, desorption and mechanical agitation. Models to calculate emulsion density, viscosity and bulk modulus are provided in C. Dixon [4] (Pg. 181). De-emulsification is a slow process due to the slow speed at which bubbles rise in a liquid. The shape of a rising bubble depends on the ratio of gravity to surface tension forces. The ratio of forces is represented by the Bond number:

$$N_{Bo} = \frac{(\rho_G - \rho_L) \cdot g \cdot D^2}{\sigma_S} \quad (2.5)$$

Large bubbles have high ratios of gravity to surface tension forces and are hence distorted. Small bubbles on the other hand are dominated mostly by surface tension effects and hence remain quasi-spherical. The distinguishing diameter between large and small bubbles is given by:

$$D = \sqrt{\frac{4 \cdot \sigma_S}{\rho \cdot g}} \quad (2.6)$$

In damper flows, slowly rising small bubbles are frequently encountered. In these types of flows, Re (based on liquid properties) is less than 1. Hence, the bubble may be analysed as translating through the liquid in a Stokesian regime (C. Dixon [4]):

$$C_D = \frac{24}{Re} \quad (2.7)$$

$$F_D = 3 \cdot \pi \cdot \mu \cdot D \cdot U_B \quad (2.8)$$

Where the rising speed U_B can be approximated using pure buoyancy effect as:

$$U_B = C_V \frac{\rho_L \cdot d \cdot D^2}{18 \cdot \mu} \quad (2.9)$$

Where the velocity coefficient C_V is introduced to account for the fact that the bubble is not solid. In case of gas bubbles, $C_V = 1.5$ and in case of liquid bubbles, it may be defined in terms of the internal viscosity μ_s as

$$C_V = \frac{3 \cdot \mu + 3 \cdot \mu_S}{2 \cdot \mu + 3 \cdot \mu_S} \quad (2.10)$$

2.2.3 Compressibility Considerations

Compressibility effects in a damper depend on the degree of emulsification. Dampers frequently exhibit characteristics which can be explained by fluid compressibility, especially at high stroke frequencies. Compressibility effects result in volume changes of the bulk fluid in the compression and rebound chambers, but they also affect flow in valves as gas expands at regions of low static pressure (C. Dixon [4]).

3

Damper Modelling

Consider the schematic of a generic monotube damper shown below:

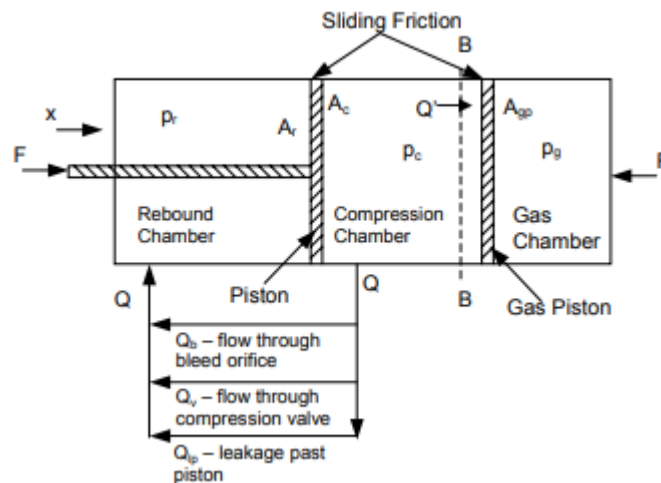


Figure 3.1: Schematic of a generic monotube damper. Source: Talbott and Starkey [1]

A damper comprises three main chambers - the compression chamber, the rebound chamber and the gas chamber. The compression and rebound chambers are separated by the main piston while the compression and gas chambers are separated by a floating gas piston. As the piston moves into the compression chamber, the velocity is assumed to be positive and such a motion is called the compression stroke. On the contrary, as the piston is withdrawn from the compression chamber, the velocity is considered to be negative and the motion is termed as the rebound stroke. The principal damping mechanism is by shearing the hydraulic fluid as it passes through restrictions, thus dissipating energy. Generally, there are three possible flow paths. The first is through a bleed orifice located at the end of the rod, which is usually tuned using an adjustable needle. The second path is through passages built into the piston governed by shim stacks. Shim stacks are essentially thin discs that deform under fluid loads to control the flow passing through the piston orifices. The final flow path is possible leakage between the piston seal and the cylinder wall. The gas chamber serves to keep the hydraulic fluid pressurised to avoid cavitation effects. Further, with the presence of a floating piston, the motion of the rod is accounted for. As the rod enters or leaves the cylinder, the gas piston moves to equalise the resulting volume change.

3.1 Overview of mathematical models

3.1.1 Damper Oil

Damper oil is generally a light mineral or synthetic oil with reduced change in viscosity with temperature with typical density of 850 kg/m^3 – 860 kg/m^3 and viscosity between $5 \text{ mPa}\cdot\text{s}$ – $100 \text{ mPa}\cdot\text{s}$ (Reybrouck [8]). Both the density and viscosity generally depend strongly on temperature. The compressibility of pure oil is very low 0.05 \%/MPa , but practically, compressibility is higher due to absorbed gas and bubbles. However, damper oils can be considered incompressible without significant loss of accuracy in analysis. For the present analysis, compressibility effects were included in the treatment and provision was made for implementation of the following temperature corrections: A Vogel-Tamman-Fulcher type equation was used to model the dynamic viscosity as:

$$\mu = \mu_0 \cdot e^{\frac{E_0}{R(T-T_\eta)}} \quad (3.1)$$

Where e is the Euler's number, E_0 is the oil molecules' activation energy and T_η is a reference temperature at which the reference dynamic viscosity μ_0 is defined (Skačkauskas et al. [2]). A similar correction for density is available, defined as:

$$\rho = \frac{\rho_0}{1 + \alpha \cdot (T - T_t)} \quad (3.2)$$

Where α is the coefficient of volumetric expansion and ρ_0 is a reference density defined at temperature T_t .

3.1.2 Piston Dynamics

The dynamics of the main piston and gas piston are modelled as second order ordinary differential equations (ODEs) considering the forces acting on them. The equation of motion for the gas piston is (Skačkauskas et al. [2]):

$$m_{gp} \cdot a_{gp} = (A_{gp} \cdot P_c) - (A_{gp} \cdot P_g) - F_{fric} \cdot (V_{gp} - V_p) - m_{gp} \cdot g \quad (3.3)$$

Where m_{gp} is the mass of the gas piston, a_{gp} is the acceleration of the gas piston, A_{gp} is the area of the gas piston, V_{gp} is the velocity of the gas piston, P_c is the compression chamber pressure, P_g is the gas chamber pressure, V_p is the velocity of the main piston, F_{fric} is the friction force and g is acceleration due to gravity. Similarly, the motion of the main piston is modelled as (Skačkauskas et al. [2]):

$$m_p \cdot a_p = (A_r \cdot P_r) - (A_c \cdot P_c) - F_{fric} \cdot V_p - m_p \cdot g \quad (3.4)$$

Where m_p is the mass of the main piston, a_p is the acceleration of the main piston, V_p is the velocity of the main piston, A_c and A_r are the areas of the main piston on the compression and rebound sides respectively, P_c and P_r are the pressures in the compression and rebound chambers respectively and g is acceleration due to gravity.

3.1.3 Pressure Dynamics

Gas Chamber

In modelling the gas chamber dynamic, the assumption of an adiabatic process is used and hence, the ideal gas law is utilised. The pressure dynamic inside the gas chamber may be expressed by the following ODE (Skačkauskas et al. [2]):

$$\frac{dP_g}{dt} = \frac{\gamma \cdot P_g \cdot (-A_{gp} \cdot V_{gp})}{(A_{gp} \cdot H_g) - (A_{gp} \cdot x_{gp})} \quad (3.5)$$

where γ is the gas adiabatic constant, P_g is the pressure in the gas chamber, A_{gp} is the area of the gas piston, V_{gp} is the velocity of the gas piston, H_g is the height of the gas chamber and x_{gp} is the displacement of the gas piston.

An alternate, simpler model for the pressure in the gas chamber is proposed by Talbott and Starkey [1]. Considering an isothermal expansion and applicability of the ideal gas law, the pressure in the gas chamber may be expressed as:

$$P_g = P_{g_{ini}} \cdot \frac{A_{gp} \cdot H_g}{A_{gp} \cdot H_g - A_{rod} \cdot x_p} \quad (3.6)$$

where $P_{g_{ini}}$ is the initial (filled) pressure in the gas chamber and A_{rod} is the cross sectional area of the piston rod.

Compression chamber

The pressure dynamic inside the compression chamber is modelled by the following ODE Skačkauskas et al. [2]:

$$\frac{dP_c}{dt} = \frac{E \cdot (-Q_{tot} - (A_{gp} \cdot V_{gp} - A_c \cdot V_p))}{(A_c \cdot H_{c_{ini}}) + (A_{gp} \cdot x_{gp}) - (A_c \cdot x_p)} \quad (3.7)$$

Where E is the oil bulk modulus, P_c is the pressure in the compression chamber, Q_{tot} is the total oil flow rate through all modelled flow paths, A_{gp} is the area of the gas piston, A_c is the area of the main piston on the compression side, V_p and V_{gp} are the velocities of the main and gas piston respectively, x_p and x_{gp} are the displacements of the main and gas piston respectively and $H_{c_{ini}}$ is the initial height of the compression chamber.

A simpler model is also proposed by Talbott under the assumption of an incompressible fluid Talbott and Starkey [1]. For an incompressible fluid, it can shown that

$$a_{gp} = a_p \cdot \frac{A_{rod}}{A_{gp}} \quad (3.8)$$

Considering the equilibrium of forces acting on the gas piston, the pressure in the compression chamber is obtained as:

$$P_c = P_g + \frac{m_{gp} \cdot a_{gp}}{A_{gp}} \quad (3.9)$$

3.1. OVERVIEW OF MATHEMATICAL MODELS

Substituting equation 3.8 in the above equation 3.9, we obtain the following simple expression for pressure in the compression chamber:

$$P_c = P_g + \frac{A_{rod} \cdot m_{gp}}{A_{gp}^2} \cdot a_p \quad (3.10)$$

Rebound chamber

The pressure dynamic inside the rebound chamber is modelled by the following ODE (Skačkauskas et al. [2]):

$$\frac{dP_r}{dt} = \frac{E \cdot (Q_{tot} - (A_r \cdot V_p))}{(A_r \cdot H_{r_{ini}}) + (A_r \cdot x_p)} \quad (3.11)$$

Where E is the oil bulk modulus, P_r is the pressure in the rebound chamber, Q_{tot} is the total oil flow rate through all modelled flow paths, A_r is the area of the main piston on the rebound side, V_p is the velocity of the main piston, x_p is the displacement of the main piston and $H_{r_{ini}}$ is the initial height of the rebound chamber.

3.1.4 Flow Rates

Shim valve flow rate

The flow through the shim valve is modelled considering the equivalence of flow between piston orifice flow and flow through the area exposed by valve deflection. This enables a mathematical model of two equations and hence a solution for the unknowns - the volumetric flow rate and the pressure at the valve surface. The two equivalent flow rate equations (for the compression stroke) are hence (Talbot and Starkey [1]):

$$Q_{valve} = \frac{\pi}{2} \cdot D_v \cdot y_{shim} \cdot C_{D_{valve}} \cdot \sqrt{\frac{2 \cdot (P_{surf} - P_r)}{\rho}} \quad (3.12)$$

Where Q_{valve} is the volumetric flow rate through the shim valve, D_v is the diameter of the largest shim in the stack, y_{shim} is the vertical deflection of the largest shim in the stack, ρ is the damper oil density, P_r is the rebound chamber pressure, P_{surf} is the pressure at the valve surface and $C_{D_{valve}}$ is a dynamic discharge coefficient which is to be modelled. For modelling of flow through during the rebound stroke, the applied pressure difference is modified to substitute rebound chamber pressure for compression chamber pressure in eqn 3.12.

The auxiliary equation necessary to obtain a closed system is (Talbot and Starkey [1]):

$$Q_{valve} = A_o \cdot C_{D_{orifice}} \cdot \sqrt{\frac{2 \cdot (P_c - P_{surf})}{\rho}} \quad (3.13)$$

3.1. OVERVIEW OF MATHEMATICAL MODELS

Where Q_{valve} is the volumetric flow rate through the shim valve, A_o is the total area of the piston orifices, ρ is the damper oil density, P_r is the rebound chamber pressure, P_{surf} is the pressure at the valve surface and $C_{D_{orifice}}$ is a dynamic discharge coefficient which is to be modelled. For modelling of flow through during the rebound stroke, the applied pressure difference is modified to substitute compression chamber pressure for rebound chamber pressure in eqn 3.13.

Bleed orifice flow rate

The flow through the bleed orifice is modelled as a generic orifice flow corrected by a dynamic discharge coefficient. For the compression stroke, this can be expressed as (Talbot and Starkey [1]):

$$Q_{bleed} = A_b \cdot C_{D_{bleed}} \cdot \sqrt{\frac{2 \cdot (P_c - P_r)}{\rho}} \quad (3.14)$$

Where Q_{bleed} is the volumetric flow rate through the bleed valve, A_b is the area of the bleed orifice, ρ is the damper oil density, P_c and P_r are the compression and rebound chamber pressures and $C_{D_{bleed}}$ is a dynamic discharge coefficient which is to be modelled. For modelling of flow through during the rebound stroke, the applied pressure difference is sign inverted. In order to account for the provision of a variable position needle to control the flow through the bleed orifice, the effective area is modified using the model below (Skačkauskas et al. [2]):

$$A_b = \frac{\pi}{2} \cdot D_b^2 \cdot \left(1 - \left(1 - \frac{n_{clicks}}{2 \cdot n_{maxclicks}} \right)^2 \right) \quad (3.15)$$

Where A_b refers to the effective area of the bleed orifice, D_b is the diameter of the bleed path, n_{clicks} refers to the current needle position and $n_{maxclicks}$ refers to the total available needle travel.

Piston leakage flow

The flow between the piston seal and the cylinder wall is unsuitable to be modelled as a generic orifice flow due to the length scales involved and hence, it is better modelled as laminar flow between two parallel plates using the Navier-Stokes equations. For the compression stroke (Talbot and Starkey [1]):

$$Q_{leak} = \left(\frac{(P_c - P_r) \cdot c^3}{12 \cdot \mu \cdot H_p} + \frac{V_p \cdot c}{2} \right) \cdot \pi \cdot D_p \quad (3.16)$$

Where Q_{leak} is the volumetric flow rate between the piston seal and damper wall, P_c and P_r are the pressures in the compression and rebound chambers respectively, H_p is the height of the main piston, c is the clearance between the piston seal and the cylinder

wall, μ is the dynamic viscosity of the oil, V_c is the velocity of the main piston and D_p is the diameter of the main piston. The imposed pressure difference is inverted for the rebound stroke.

3.1.5 Shim stack model

Stiffness based model

The following model suggested by Talbott and Starkey [1] was initially considered:

$$k_{shim} \cdot y_{shim} = \Delta P_{valve} \cdot A_v + \rho \cdot \frac{Q_{valve}^2}{A_o} \cdot C_f - F_{preload} \quad (3.17)$$

Where k_{shim} is the shim stiffness, y_{shim} is the shim deflection, δP_{valve} is the effective pressure difference across the shim valve, A_v is the area of the largest shim in the stack, ρ is the density of the damper oil, Q_{valve} is the volumetric flow rate through the shim valve, A_o is the total area of the piston orifices, C_f is an empirical modifier for the fluid momentum term and $F_{preload}$ is the preload force on the shim stack.

However, this model posed the following difficulties:

- The stiffness k_{shim} is not a material property and is geometry dependent. Hence, it would need to be determined from numerical simulations or from experiments.
- The constant C_f needs to be determined with bespoke experiments or numerical analysis and no literature data is available even for an order of magnitude estimate.

Hence, for the final implementation, the force method based model detailed in section 3.1.5 was used.

Force method based model

A force method based model solves the structural dynamic equations for the entire shim stack for the shim displacements. By doing so, this model negates the need to explicitly define a stiffness for the shim stack and avoids the use of empirical constants, hence leading to easy implementation and increased accuracy over the simpler stiffness-based model proposed above in 3.1.5.

3.1. OVERVIEW OF MATHEMATICAL MODELS

Consider the shim stack shown in figure 3.2:

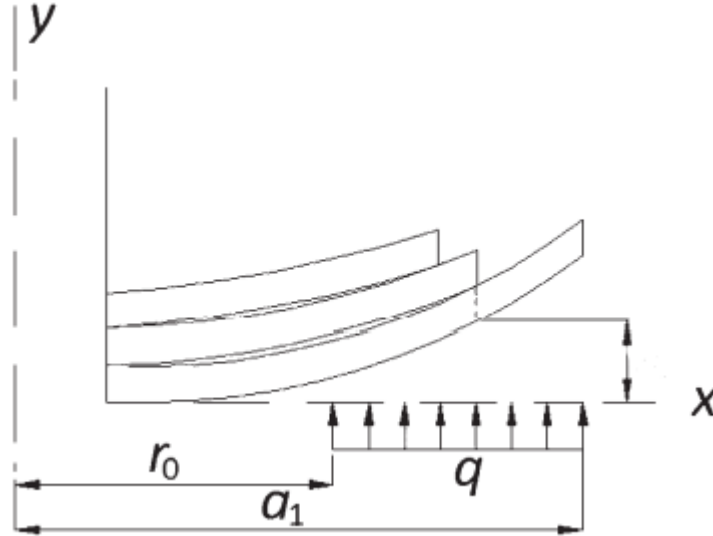


Figure 3.2: Schematic of the displacements a generic shim stack. Source: Skačkauskas et al. [2]

The shim stack is analysed as a statically indeterminate structure under the following assumption - the shims contact at their external radii only. This is a reasonable assumption since during operation, air gaps appear between shims.

The system of three shims may hence be reduced to analysis by the following two load cases:

1. Distributed load acting on the shim contacting the piston due to fluid flow through the piston orifices.
2. Concentrated load acting at the external radii of the successive shims as they pose reaction forces.

In order to model the distributed load due to the fluid, the distributed load is assumed to be acting along the shim from the external radius upto a defined opening radius. The following formula proposed by Skačkauskas et al. [2] is used to determine the opening radius considering an equivalence of area between the piston orifices and an annular shim with an inner radius as the opening radius and an outer radius as the external radius:

$$r_{op} = \frac{\sqrt{-\pi \cdot (A_s - \pi \cdot a_1^2)}}{\pi} \quad (3.18)$$

Where A_s is the total cross-sectional area of the piston orifices and a_1 is the external radius of the shim in contact with the piston.

3.1. OVERVIEW OF MATHEMATICAL MODELS

The modelled system is hence as shown below in fig 3.3:

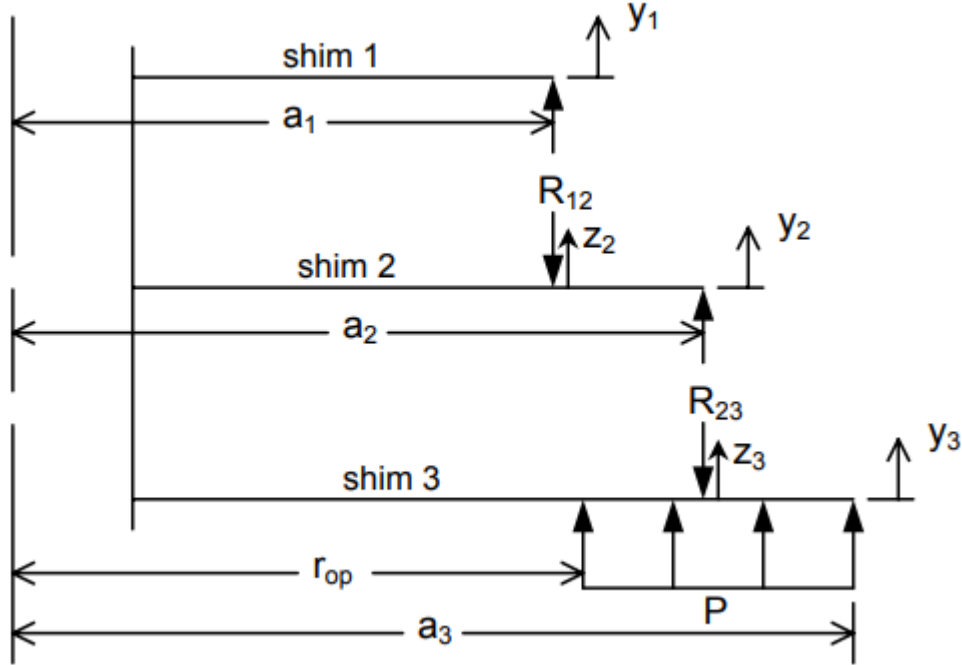


Figure 3.3: Computational scheme of a shim stack. Source: Talbott and Starkey [1]

This system may be solved using multiple approaches, for instance:

- Modelling shims as cantilever beams to generate equations for displacement, as performed by Skačkauskas et al. [2].
- Developing a 1D finite element model, as performed by Czop et al. [12].
- Utilising First-Order Shear Deformation Theory (FSDT) along with Rayleigh-Ritz approximation and Lagrange multipliers method to minimize total potential energy, as performed by Farjoud et al. [13].
- Using the method of consistent displacements, as performed by Talbott and Starkey [1]

For this work, the method of consistent displacements was used. Under the aforementioned assumption of contact at external radii, the principle of superposition may be applied at all the individual displacements and a system of equations is obtained to ensure consistency in the displacements. For the demonstrated stack of three shims, this system of equations is:

$$y_3 = (y_3)_P + (y_3)_{R23} \quad (3.19)$$

$$y_2 = (y_2)_{R23} + (y_2)_{R12} = (z_3)_{R23} + (z_3)_P \quad (3.20)$$

3.1. OVERVIEW OF MATHEMATICAL MODELS

$$y_1 = (y_1)_{R12} = (z_2)_{R12} + (z_2)_{R23} \quad (3.21)$$

Expressions for displacements for an annular plate are obtained using Budynas and Sadegh [14]. Hence, the system of equations is solved for $R12$, $R23$ and y_1 .

This method was implemented for a generic shim stack using the following MATLAB functions:

1. The following nomenclature is utilised: a = shim outer radius, b = shim inner radius, t = thickness, r_0 = position of the concentrated load, r_{op} opening radius for distributed load, r radial position at which displacement is evaluated, w = point load, q = pressure load and W_i = reaction force between shim i and shim $(i + 1)$.
2. Function `lineload(w,a,b,t,t_0,r)` which outputs the deflection at any given radial position due to a concentrated load.
3. Function `distload(p,a,b,t,r_{op},r)` which outputs the deflection at any given radial position due to a distributed load.
4. Function `Shim-stack-model()` which contains the geometrical details of the shim stack and solves the system of equations

Furthermore, the following approach was used to ease the implementation:

1. Shims were modelled as struct variables containing their geometrical parameters.
2. The nomenclature for shims was as follows - The shim in contact with the piston was assigned the index 1.
3. Reaction loads from a shim with a lower index, i.e previous shim were denoted with the notation ' w_p ' and reaction loads from a shim with a higher index, i.e next shim were denoted with the notation ' w_n '.
4. The deflection ' y ' of a given shim corresponds to deflection at the external radius while the deflection ' z ' corresponds to deflection at the point of contact with the next shim, i.e the external radius of the next shim.
5. In order to model the effect of a shim stop, a stiffer 'last' shim is created in the stack.

The following equations hence define all the displacements that are needed to assemble the system of equations: The first shim contains the following four displacements:

$$(y_1)_P = \text{distload}(p, a_1, b_1, t_1, r_{op}, a_1) \quad (3.22)$$

$$(z_1)_P = \text{distload}(p, a_1, b_1, t_1, r_{op}, a_2) \quad (3.23)$$

$$(y_1)_{w_n} = \text{lineload}(W1, a_1, b_1, t_1, a_2, a_1) \quad (3.24)$$

$$(z_1)_{wn} = \text{lineload}(W1, a_1, b_1, t_1, a_2, a_2) \quad (3.25)$$

Similarly, all intermediate shims are characterised by the following four displacements:

$$(y_i)_{wp} = \text{lineload}(W(i-1), a_i, b_i, t_i, a_i, a_1) \quad (3.26)$$

$$(z_i)_{wp} = \text{lineload}(W(i-1), a_i, b_i, t_i, a_i, a(i+1)) \quad (3.27)$$

$$(y_i)_{wn} = \text{lineload}(Wi, a_i, b_i, t_i, a(i+1), a_i) \quad (3.28)$$

$$(z_i)_{wn} = \text{lineload}(Wi, a_i, b_i, t_i, a(i+1), a(i+1)) \quad (3.29)$$

The last shim in the stack is characterised by a single displacement:

$$(y_{last})_{wp} = \text{lineload}(W(last-1), a_{last}, b_{last}, t_{last}, a_{last}, a_{last}) \quad (3.30)$$

Having generated expressions for the displacements, the system of equations to ensure consistency is hence: At the first shim,

$$y_1 = (y_1)_P + (y_1)_{wn} \quad (3.31)$$

At the second shim, a separate equation is formed due to the presence of the distributed load:

$$(z_1)_{wn} + (z_1)_P = (y_2)_{wn} + (y_2)_P \quad (3.32)$$

At all intermediate shims after the second,

$$(z_1)_{wn} + (z_1)_{wp} = (y_2)_{wn} + (y_2)_{wp} \quad (3.33)$$

At the last shim,

$$(z_{last-1})_{wp} + (z_{last-1})_{wn} = (y_{last})_{wp} \quad (3.34)$$

The resulting system of equations may then be solved for the array of reaction forces, W and the deflection at the first shim, y_1 .

3.2 Model Coefficients

Given the complexity of flow passages within a damper, the flow quantities computed using analytical means need to be corrected for by empirical coefficients such as dynamic discharge coefficients. Modelling of the necessary coefficients necessitates either extensive experimental data, which is not trivial given the length and time scales of the flow, or data from numerical simulations. In order to characterise the flow in a satisfactory manner, a class of numerical simulations called ‘‘Fluid Structure Interaction (FSI)’’ simulations need to be performed. This is necessary due to the coupling in the structural dynamics of the highly flexible shim valves and the fluid dynamics of the flow that is governed by these shim valves.

4

Implementation of the Mathematical Model

As detailed above in 3, the core mathematical model consists of three coupled first order ODEs to solve for pressures, two second order ODEs to solve for piston motions and four algebraic equations to solve for individual flow rates. However, the algebraic system is coupled with the pressure ODE system since pressure computations require solving for the total volumetric flow rate.

4.1 Software for modelling and Simulation

Two models were implemented using the MATLAB and Simulink software environment:

1. **Dynamic model using Simulink:** This model solved for true transient states using ODEs 3.7 for compression chamber pressure, 3.5 for gas pressure, 3.11 for rebound chamber pressure and ODEs 3.1.2 for piston dynamics. This model offered the highest flexibility of application in addition to modelling transient effects.
2. **Simple using MATLAB:** This model used simpler models by Talbott and Starkey [1] to solve for intermediate equilibrium states, viz 3.10 for compression chamber pressure, 3.6 for gas chamber pressure and implemented the 3.1.5 . This required the implementation of a nonlinear systems solver based on Newton's method, as performed by Rhoades [9].

4.1.1 MATLAB

MATLAB is a language for technical computing. It integrates programming, computation and post-processing in a single environment. The programming language is similar to conventional mathematical notation [15].

4.1.2 Simulink

Simulink is a tool provided by MATLAB. It is a block diagram environment for the design and simulation of models. Beyond simulation, it also supports automatic code generation.

It includes libraries of "blocks" to model physical systems [16].

4.2 MATLAB Scripts

4.2.1 MATLAB scripts for the Simulink model

The following scripts were developed in order to implement the damper Simulink model:

- **Init** -The geometric and functional parameters of the damper are initialised using this script.
- **Shim valve model** - This script solves the system of equations for the volumetric flow rate through the shim valve and pressure at the surface of the shim valve.
- **Friction model** - Implements a smooth friction model that takes velocity as an argument and outputs the friction force.

4.2.2 MATLAB model

The MATLAB model was implemented as a function with an input frequency as the argument. This frequency corresponds to the frequency of the sinusoidal motion imposed on the piston, thus replicating a suspension dynamometer. All geometrical parameters and coefficients were initialised by the Init script used for the Simulink model.

4.3 Simulink Model

The Simulink representation of the complete model is shown below in Fig 4.1

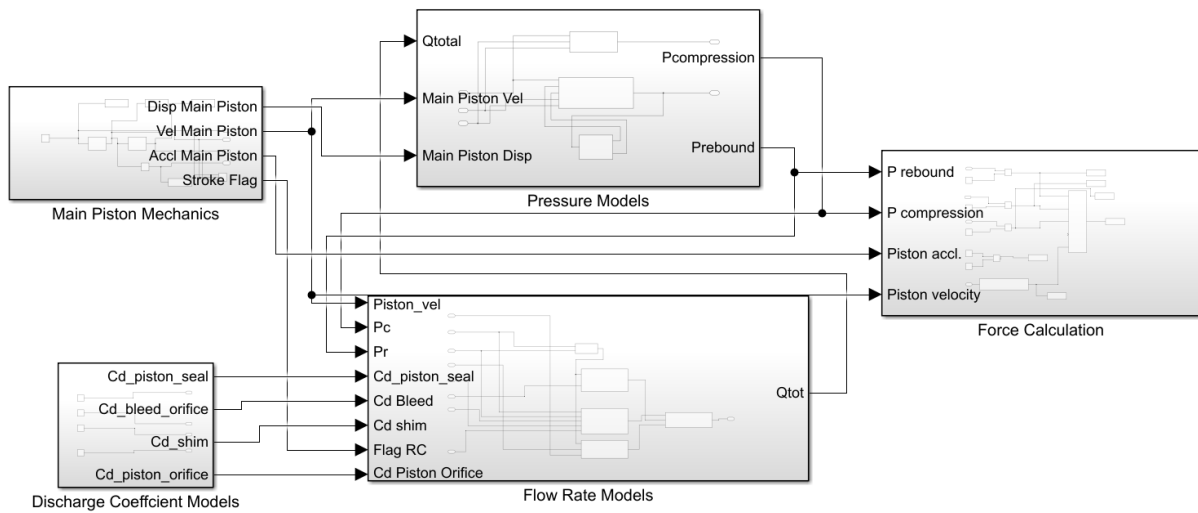


Figure 4.1: Simulink model of a generic automotive damper

Details of a few salient blocks are elaborated in the following sections:

4.3.1 Gas Piston Dynamics

This block implements the ODE for the dynamics of the gas piston described in 3.1.2 on page 13:

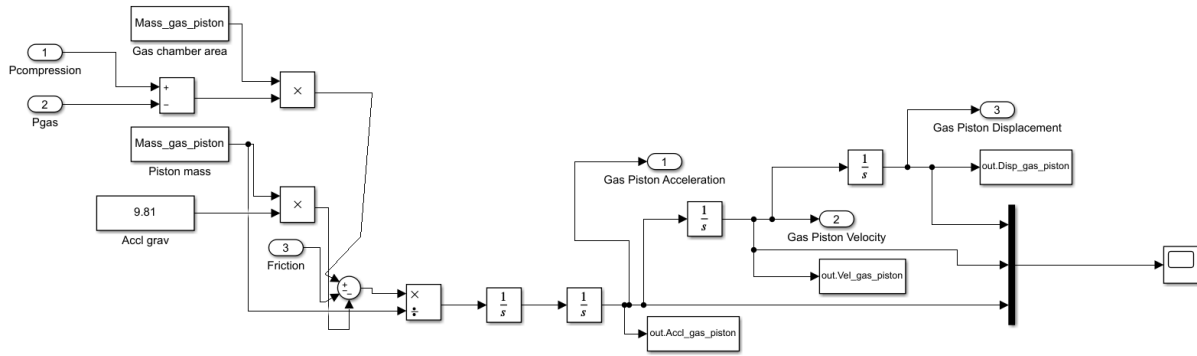


Figure 4.2: Gas Piston Dynamics Block

4.3.2 Pressure blocks

The following block illustrates the Simulink implementation of the ODE pertaining to pressure dynamics in the compression chamber described in 3.1.3 on page 14:

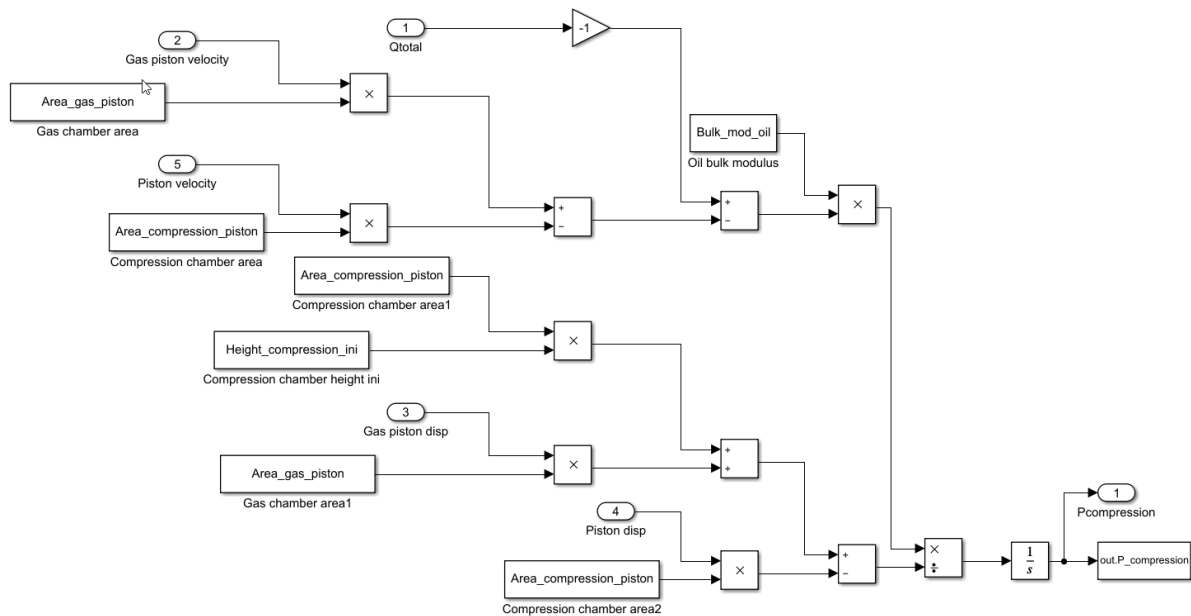


Figure 4.3: Compression chamber Pressure Dynamics Block

Similar blocks are implemented to model the pressure dynamics in the gas chamber and in the rebound chamber.

4.3.3 Flow Rate blocks

Bleed Orifice Flow Rate

The following block computes the volumetric flow rate through the bleed orifice and implements the algebraic analytical model demonstrated above in [3.1.4 on page 16](#):

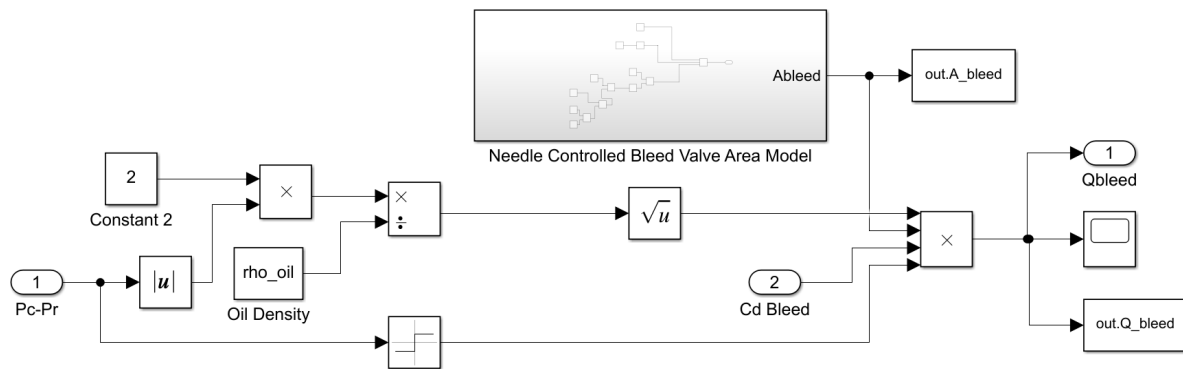


Figure 4.4: Bleed Orifice Volumetric Flow Rate Block

Piston Seal leakage Flow rate

The following block computes the volumetric flow rate by leakage through the piston seal and implements the algebraic analytical model demonstrated above in 3.1.4 on page 16:

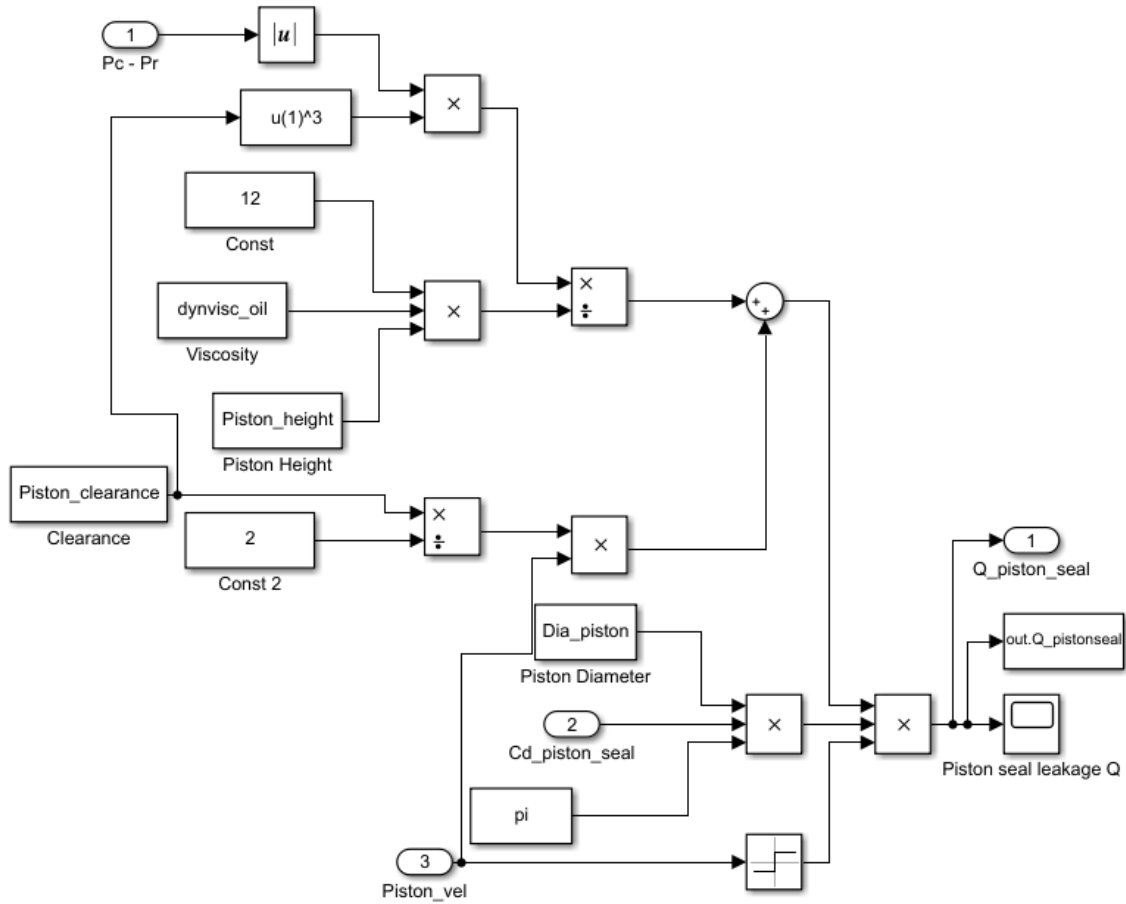


Figure 4.5: Piston Seal Leakage Volumetric Flow Rate Block

4.3.4 Damping Force Computation

The following block computes the damping force generated by the damper:

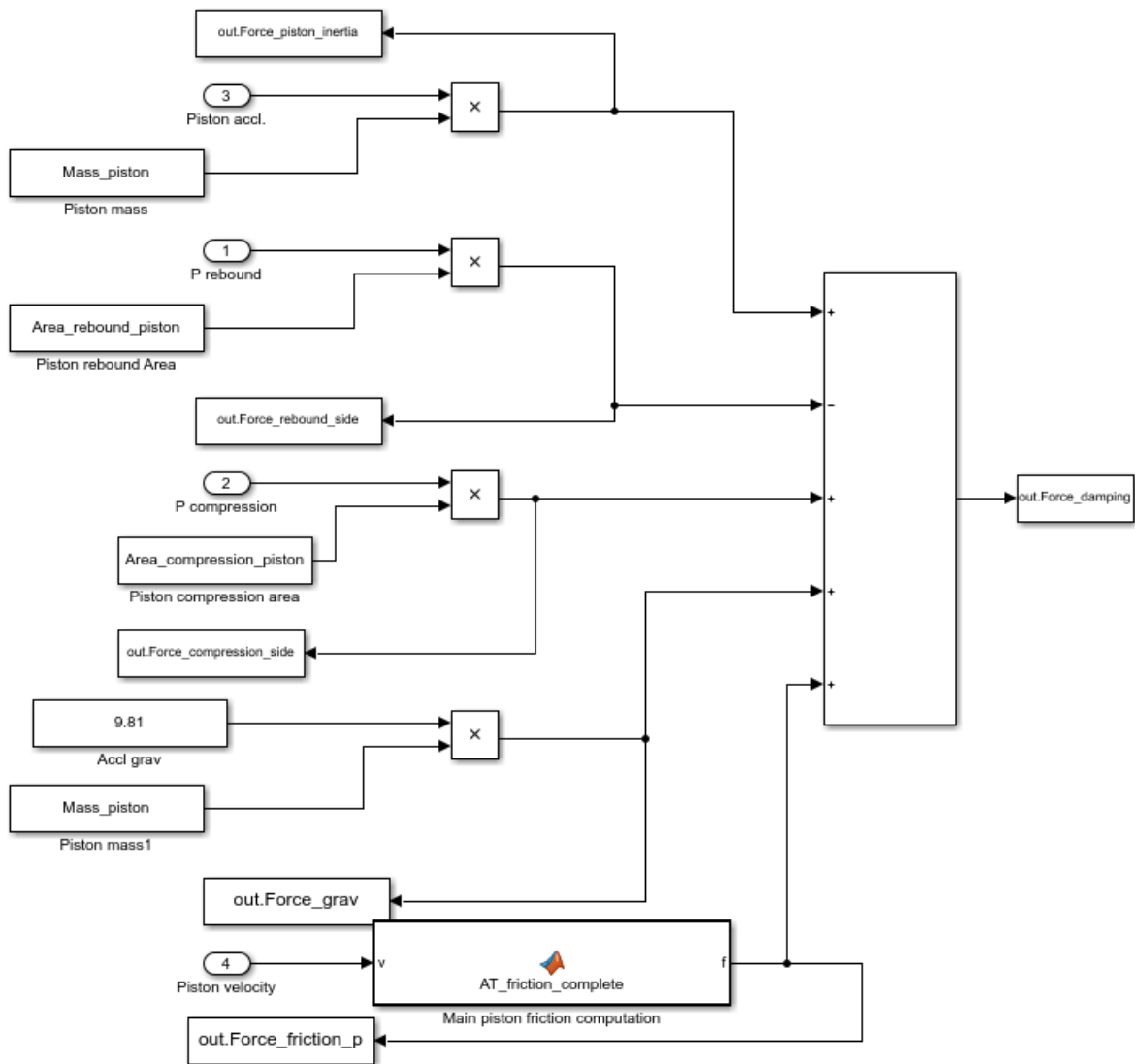


Figure 4.6: Damping Force Computation Block

5

Numerical Analysis - An Introduction

Numerical analysis is required to derive values for model coefficients for the lumped parameter model.

5.1 Overview of Numerical Methods

Engineers have striven from centuries to evaluate variables of engineering interest such as displacements, forces and pressures for a wide range of problems. Centuries of study have led to the development of physico-mathematical models that are applicable with acceptable margins of error over a wide range of commonly encountered problems. However, these physico-mathematical models do not prove to be readily applicable and provide closed-form analytical solutions only to the most basic of problems. Hence until recently, only experimental data was available to model complex phenomena. In the last couple of decades, with the advent of “cheap” computers, a third discipline of computational methods have emerged. While the legacy physico-mathematical models are based upon the continuum assumption, computational methods aim to solve the same systems of partial differential equations using a discretized “grid”. The three principal philosophies of discretization are the finite element, finite difference and finite volume methods. Without delving into details that are beyond the scope of this report, the finite element method is most commonly used for structural problems involving determination of the displacement field (FEA/FEM solvers), and the finite volume method is the popular method of choice for fluid dynamic problems involving determination of the velocity, pressure and temperature fields (CFD solvers).

5.2 Finite Element Methods

Finite Element Methods (FEM) is a discretization method used in structural solvers to solve for a range of variables. A discretization method is used to obtain solutions to continuous systems of differential equations on a discretized domain, leading to simpler systems of algebraic equations. This method is mainly employed to solve all classes of structural problems such as steady-state, transient and eigenvalue problems. While the

finite element method is primarily used to solve structural mechanics, it is also applicable for other engineering problems such as heat conduction, electromagnetism and even fluid dynamics (Rao [17]).

5.3 Computational Fluid Dynamics

CFD (Computational Fluid Dynamics) is a method of analysing flow cases using computational power, mainly using the finite volume method.. Just as in FEM, the basis for different flows are mathematically modelled as differential equations, which are then discretised in time and space into algebraic equations which a computer can then solve. Numerous turbulence models can be applied to the flow field cases to reproduce the cases as it were in real-life. The versatility of using CFD, makes it a powerful tool in an engineers hand. In recent years, its rise has lead to a decrease in very expensive testing and faster overall production times (Versteeg and Malalasekera [18]).

5.4 Fluid Structure Interaction

Fluid–structure interaction (FSI) is a class of problems with mutual dependence between the fluid and structural dynamics. The flow behavior depends on the shape of the structure and its displacement, and the motion and deformation of the structure depend on the fluid dynamic forces acting on it. The inherently nonlinear and time-dependent nature of FSI makes it very difficult to use analytical methods in this class of problems. Only a handful of cases have been studied analytically, where simplifying assumptions have been invoked to arrive at closed-form solutions of the underlying partial differential equations (Yuri Bazilevs [19]). While most engineering problems involve fluid-structure interactions, the coupling is mostly weak. The structural deformation can be assumed to be negligible with acceptable errors in the solution and hence, it is sufficient to solve the fluid dynamic problem using a CFD code. In addition, even with the presence of non-negligible coupling, it is sufficient to model a one-way data transfer in some cases. For example, the CFD solver solves a time step and sends information to the structural solver and then both solvers move to the next time step. It is then apparent that the shim stack is a strongly coupled FSI problem. The deformation of the shim stack is completely dependent on the pressure field imposed by the fluid and the fluid pressure and velocity fields are in turn highly dependent on the instantaneous configuration of the shim stack. It is imperative to solve both the structural dynamics and fluid dynamics in conjunction with each other. This is done using a two-way data transfer. For every time step, the CFD and structural solvers iterate in both directions to reach convergence before moving to the next step.

5.4.1 Classes of FSI solvers

Monolithic Solvers

Monolithic or direct-coupled FSI solvers contain a unique solver to solve both structural and fluid dynamics. The monolithic approach is based on the fully coupled discretization

of the governing equations. Both fluid and solid equations are solved in a single matrix using variants of Newton’s or Picard’s method. Monolithic approaches are more robust and efficient than the partitioned methods, particularly for unsteady problems (Ha et al. [20]) (Lozovskiy et al. [21]). One of the popular approaches to deal with the discrepancy between Eulerian and Lagrangian formulations for fluids and solids is the Arbitrary Lagrangian-Eulerian (ALE) method. In the ALE method, the structure is presented in Lagrangian coordinates while the fluid flow is considered in an artificial coordinate system (Lozovskiy et al. [21]). However, for large domains, the monolithic approach is “in general computationally challenging, mathematically and economically suboptimal, and software-wise unmanageable” (Piperno [22]).

Partitioned Solvers

Partitioned solvers contain two individual solvers coupled at the interface of the two domains. However, the partitioned approach has an advantage of modularity because the best available solver for each domain is employed. Moreover, they do not require a matched mesh at the interface (Ha et al. [20]). During each time step, information is transferred back and forth between the CFD and FEM solvers in coupling iterations until the coupling step is converged. This is the so called Conventional Serial Staggered procedure (Piperno [22]):

1. Transfer the motion of the FSI boundary in the structural domain to the fluid domain
2. Update moving mesh in the fluid domain,
3. Advance in time and compute fluid solution,
4. Convert pressure and fluid stress into structural loads,
5. Advance in time and compute the structural solution.

5.5 Performance of FSI Solvers

5.5.1 Performance of Monolithic Solvers

Lozovskiy et al. [21] analysed the stability and performance of a monolithic FSI finite element code utilising the Arbitrary Lagrangian-Eulerian method. It was observed that the constraint on the time step was dictated by requisite accuracy rather than stability. It was reported that the method could not deal with large structural displacements at the time of publication, but with the advent of new prolongation methods, the authors expressed hope that this shortcoming may be resolved in the near future. The number of grid points was not reported. Ha et al. [20] performed a comparative study between an in-house monolithic code and ANSYS Multiphysics partitioned code with a similar number of grid points ($\approx 85,000$). They found the monolithic solver to converge faster and that the number of iterations was almost similar regardless of the inlet pressure for both methods. However, in contrast to the monolithic code, the partitioned code did

not converge for the case of the highest inlet pressure. The error of the monolithic code was found to decrease monotonically with iteration, whereas that of the partitioned code slowly converged after a rapid decrease in the error in the first few iterations. The monolithic code exhibited a clear advantage in terms of CPU hours, by almost three orders of magnitude. The required system memory was found to be similar for both codes. Furthermore, the convergence behaviour of the monolithic code was found to be independent of the time step while the convergence behaviour of the partitioned code was found to be strongly dependent, necessitating smaller time steps. Finally, the partitioned algorithm had stagnated error when the structure was highly deformed, whereas the residual of the monolithic method was monotonically reduced during the nonlinear iteration regardless of the order of deformation. Heil et al. [23] performed similar comparisons within the open-source OOMP-LIB framework. The authors found the monolithic solver to be competitive with segregated solvers even with weak fluid-structure coupling. However, they stress the need to utilise an efficient preconditioner to handle the large linear systems that arise during computation. The authors utilised the Elman, Silvester and Wathen's LSC Navier-Stokes preconditioner, which produces mesh-independent convergence rates for transient problems and was proven to work with mesh refinement. Commercially available monolithic solvers include COMSOL [24] and ADINA [25].

Performance of ADINA

Leventhal [26] performed a FSI simulation of a ball check valve using ADINA. A 2 dimensional axisymmetric mesh was utilised. However, details such as the number of nodes, turbulence model, and mesh deformation strategy are not provided. While the paper includes some experimental results, they do not serve to validate the CFD analysis. Gherardi et al. [27] performed FSI simulations of a cubical fluid cavity with a flexible bottom using ADINA. They simulated the same problem using both the monolithic solver and the partitioned solver available in ADINA and compared the results with prior numerical analyses. Laplacian smoothing method was used for implementing a dynamic mesh. They used three CFD meshes, each of 13,824 elements, 46,656 elements and 110,592 elements respectively. The authors found the monolithic method to output lower oscillations, which was attributed to the intrinsic stability of the method and the different numerical discretization of the flow field. The partitioned method, however, proved to be much more efficient in terms of computational time. The results of the monolithic method were found to be in good agreement with prior numerical simulations while the authors did not provide a direct comparison between the results of the partitioned method and the benchmark studies.

Performance of COMSOL Multiphysics

Ramadan and Saichua [28] performed transient FSI simulations using COMSOL Multiphysics to simulate a semi submerged axisymmetric buoy. The study included two meshes of 2,791 and 3,512 nodes each. A moving mesh algorithm was used to impose a dynamic mesh. The PARADISO linear system solver was employed due to the coarse meshes. The total simulation time was 10s and the solver was reported to have converged with auto time-stepping. Although not explicitly reported, since this work is a student thesis, it may be assumed that the simulations were performed on a personal computer. No experiments were performed for validation. The numerical results were found to agree in

trend with analytical predictions. Yeh et al. [29] performed FSI simulations of a bileaflet mechanical valve. They used four meshes, each of 9,900 elements, 17,300 elements, 21,200 elements and 39,200 elements respectively. The finest mesh is reported to correspond to Kolmogorov's length scale, thus permitting a DNS. However, the authors proceeded with using a $k-\omega$ RANS model to model turbulence. While no experimental validation was performed, the authors reported very good agreement of the results with other numerical studies of the same problem.

Conclusions - Monolithic Solvers

While monolithic solvers provide a clear and significant performance advantage over partitioned solvers, there is no evidence to date of utilising monolithic solvers in meshes of the order of 100,000 nodes. It must also be noted that most FSI simulations performed with monolithic solvers comprise aortic valves. The length scales of such bio-medical problems are of the order of microns to millimeters and hence the flow field can be completely resolved with a reasonable mesh size. For the scope of the shim-stack dynamic problem, it is desired to resolve the flow field to a high resolution and hence a 3D mesh of the order of 500,000 elements at the very least is expected (considering a RANS simulation). Hence, for this class of problem, it would seem that monolithic solvers do not appear to be computationally viable at this point in time.

5.5.2 Performance of Partitioned Solvers

As indicated above, partitioned solvers lose out to monolithic solvers in terms of solution stability and performance. However, at this point of time, it is not computationally feasible to simulate large flow domains with sufficient accuracy/resolution using monolithic solvers and partitioned solvers have proven to be more viable. Partitioned solvers typically comprise of a FEA/FEM structural dynamics solver and a FVM fluid dynamics solver working iteratively with each other. Commercial packages offering this type of coupling include ANSYS and the pair of ABAQUS and Star CCM+. However, an open source solutions are now possible using a coupling library called preCICE, developed by the University of Stuttgart. It is capable of linking multiple open source structural and fluid dynamic solvers.

Performance of ABAQUS and StarCCM+

Gomes [30] performed a FSI simulation of a 2D geometry consisting of a cylinder and flat plate and compared the results to numerical benchmarks. Steady state simulations gave rise to errors within 3% of the benchmarks, while no comparison was performed for the transient simulation. Three meshes of 984 elements, 1,372 elements and 2,006 elements each were used. The simulations with ABAQUS and Star CCM+ were reported to be "difficult to accomplish" since the solution was highly dependent on mesh size and time-step. The author further reported that only one mesh/time-step combination produced results "free of wiggles".

Performance of ANSYS Mechanical and ANSYS Fluent

Nilsson [10] performed FSI simulations of a shock absorber check valve using ANSYS Mechanical + FLUENT and compared with results from steady-state experiments. Simulations of a 45° slice of the damper were performed on a personal computer while the complete geometry was simulated on a cluster. Multiple mesh configurations and turbulence models were tried and the author found negligible differences with turbulence modelling. Mesh studies were performed for the 45° slice with meshes of 293,000 cells, 312,000 cells, 824,000 cells and 861,000 cells. Correlation with experimental results was the criteria in mesh selection. Simulation results were found to be in good agreement with experimental results. Shams et al. [31] performed simulations of a damper valve using ANSYS. They used the `k-ε RNG turbulence model` with a fine mesh. The number of elements was not reported. They found good agreement with experimental results.

CalculiX + OpenFOAM

Risseuw [32] performed FSI simulations of a flexible flapping wing using a completely open source solver setup comprising of OpenFOAM for fluid dynamics and CalculiX for structural dynamics, coupled by the preCICE coupling library. The FSI setup was validated considering a cylinder-flap geometry and good agreement was found with experimental results. The flexing flapping wing, however, was not validated against experiments .

Conclusions - Partitioned Solvers

Simulations performed using partitioned solvers are found to be in good agreement with experimental results. Moreover, these solvers permit large mesh sizes of the order of 1,000,000 cells, hence permitting good spatial resolution even for large flow domains. Among commercial partitioned solvers, ANSYS appears to be the most popular for FSI simulations.

6

FSI Simulations - Setup

6.1 Geometry

The test damper was required to be recreated digitally in order for the FSI simulations to be performed. The shims were reconstructed using a CAD program with dimensions obtained from the manufacturer data sheet and assembled to create both compression and rebound stack sub-assemblies. The piston was recreated using caliper measurements. The piston rod was modelled using caliper measurements as well. All the above sub-assemblies were assembled to form a complete damper assembly as shown in fig 6.1.

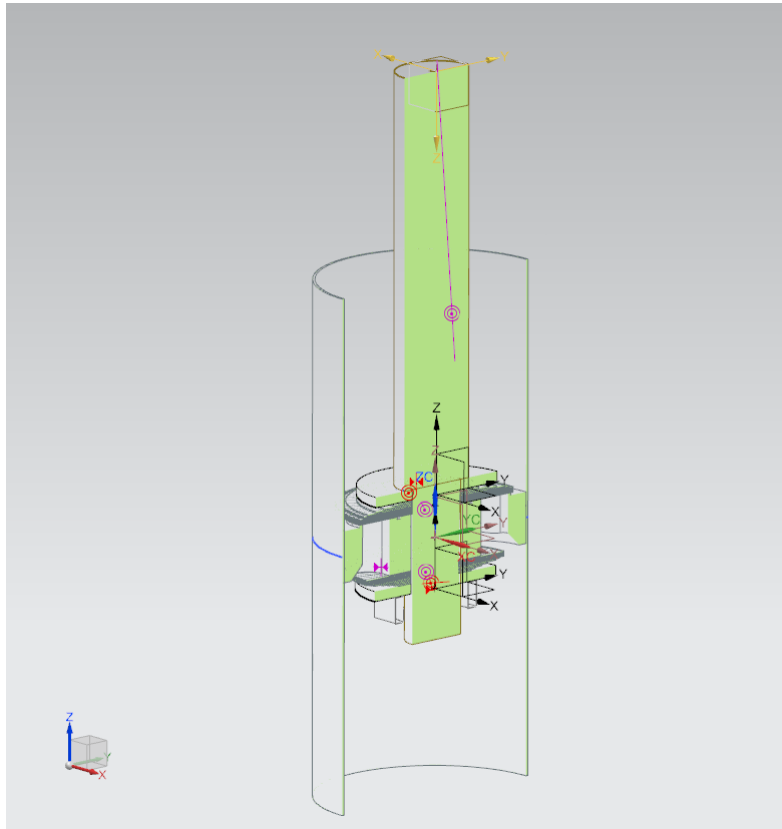


Figure 6.1: CAD assembly of the monotube damper

Since all respective orifices were identical, the model was sliced into $1/8^{\text{th}}$ so as to reduce the volume to be meshed, thus increasing spatial resolution for the same number of elements. The sliced geometry is shown in fig 6.2.

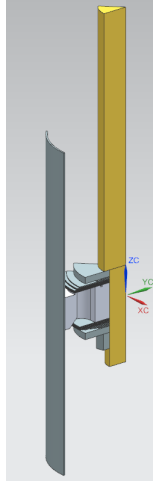


Figure 6.2: CAD assembly of the $1/8^{\text{th}}$ section of the monotube damper

6.2 The Solvers

The combination of OpenFOAM + CalculiX coupled with preCICE was opted for considering their open source distribution and the possibility to implement custom solvers. Details about the individual solvers may be found below:

6.2.1 OpenFOAM

OpenFOAM (Open-source Field Operation and Manipulation) is an open source Computational Fluid Dynamics software [33]. It is a collection of free tools that are primarily but not exclusively used for CFD problems. OpenFOAM consists of multiple solvers that each function as a stand-alone application (Chourdakis [3]). For the scope of this work, the following two solvers were used:

- **simpleFoam** - a steady-state, turbulent solver for incompressible flows utilising the Semi-Implicit Method for Pressure Linked Equations (SIMPLE) algorithm. [34].
- **pimpleFoam** - a transient, turbulent solver for incompressible flows using the PIMPLE algorithm, a combination of the SIMPLE and the Pressure Implicit with Splitting of Operators (PISO) algorithm. [35].

OpenFOAM is linked to the preCICE coupling library via an adapter developed by Chourdakis. The adapter connects the solver to preCICE during runtime, allowing preCICE access to simulation data and to steer the coupled simulation. The adapter is loaded by the controlDict file of the openFoam case. The adapter supports coupling of OpenFOAM

for Fluid Structure Interaction (FSI) and Conjugate Heat Transfer (CHT) simulations (Chourdakis [3]).

6.2.2 CalculiX

CalculiX is an open source package designed to solve finite element problems. The solver is capable of linear and non-linear calculations. CalculiX was developed by a team of enthusiasts of MTU Aero Engines (Munich) in their spare time [36].

The package is written mainly in C and Fortran and different solvers are invoked depending on the type of the problem. The solvers are implemented as C functions. For the scope of the present work, the dynamic implicit and explicit solvers were used.

An adapter was first developed by Yau [37] to couple CalculiX to preCICE for CHT applications. The adapter was subsequently extended for FSI applications by Uekermann et al. [38].

6.2.3 preCICE

preCICE (Precise Code Interaction Coupling Environment) is a coupling library that provides a "black-box" approach to coupling simulations that need to exchange information on shared boundaries. In order to couple two solvers, an additional adapter is required for each solver (Chourdakis [3]). A visual representation of these interactions is shown in Fig. 6.3 below:



Figure 6.3: An overview of the coupling between a fluid dynamics (CFD) solver and a structural mechanics (CSM) solver using preCICE. Source: Chourdakis [3]

This enables preCICE access to read and write data at the shared boundaries, as well as dictate the time step in order to synchronise both solvers.

Coupling Schemes

At shared boundaries involving multi-physics simulations, the values computed from both solvers need to be in agreement to ensure convergence and numerical stability. preCICE provides two types of equation coupling (Chourdakis [3]):

- **Explicit coupling** - Executes a specified number of iterations sans convergence checks or solution steering.

- **Implicit coupling** - Iteratively solves a fixed-point equation to ensure convergence. This utilises either an under-relaxation method or a more complex quasi-Newton method. This is more precise but expensive in terms of computational resources and time.

In addition, preCICE provides the following coupling schemes for the solvers:

- **Serial** - The solvers are run alternately and need to wait for each other to use the most current data.
- **Parallel** - Both solvers are run simultaneously using data from the previous run of the solvers.

Either equation coupling may be used with either solver coupling scheme, providing a possibility of four configurations. The configurations are elaborated visually below in Figs 6.4 to 6.7. Here, two solvers S_1 and S_2 map elements between vector spaces X_1 and X_2 , n denotes the time-step. Acc refers to the post-processing step. After every non-converged iteration, the latest stored state of the solver, called a checkpoint, is loaded (Chourdakis [3]). The four coupling schemes may hence be visually represented as:

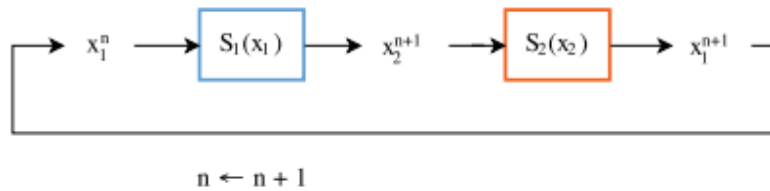


Figure 6.4: Serial explicit coupling scheme Source: Chourdakis [3]

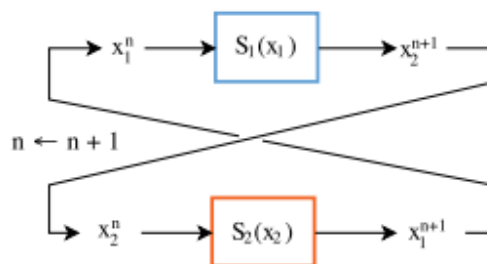


Figure 6.5: Parallel explicit coupling scheme Source: Chourdakis [3]

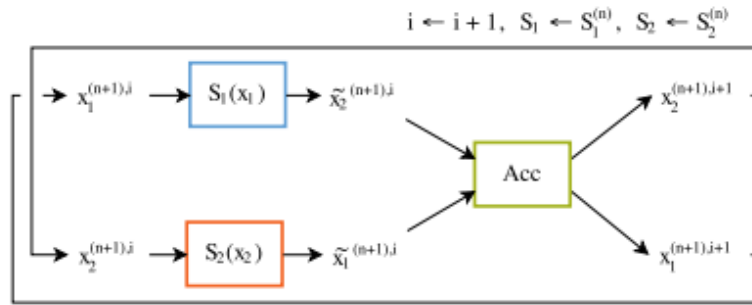


Figure 6.7: Parallel implicit coupling scheme Source: Chourdakis [3]

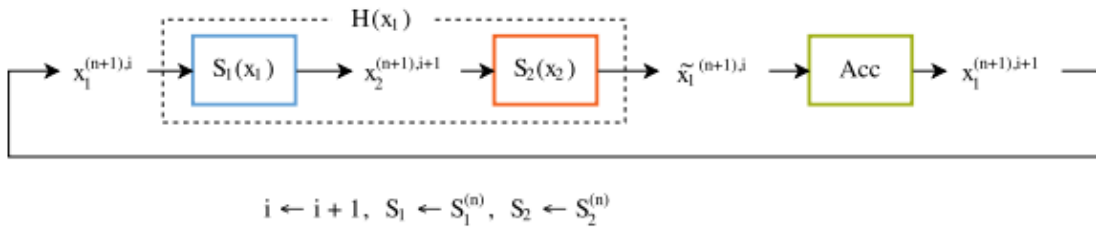


Figure 6.6: Serial implicit coupling scheme Source: Chourdakis [3]

In addition to the coupling schemes, preCICE also allows for sub-cycling, i.e preCICE permits one solver to run multiple smaller time steps within every coupling internal. However, this is not recommended for FSI simulations and may cause instabilities. A visual representation of sub-cycling is provided below in Fig.6.8

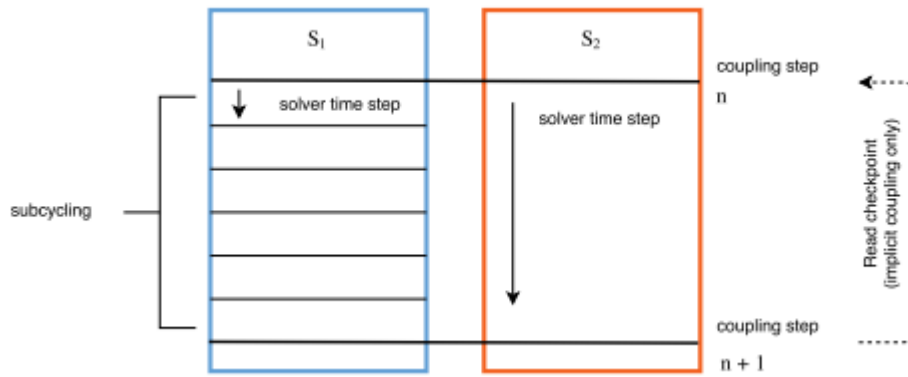


Figure 6.8: Solver sub-cycling scheme Source: Chourdakis [3]

Data Mapping

Multi-physics simulations often involve non-conforming meshes. It is a challenge to map data between these domains. The mapping not only needs to find the closest corresponding mesh point but also ensure that mass and energy balances are not violated. preCICE provides two mapping forms:

- **Consistent form** - Value at a node is mapped to the corresponding node on the other mesh. Fields such as velocity and temperature are mapped consistently.
- **Conservative form** - Ensures that integral values are preserved. Forces are mapped conservatively.

Figs 6.9 and 6.10 provides a visual representation of consistent and conservative mapping:

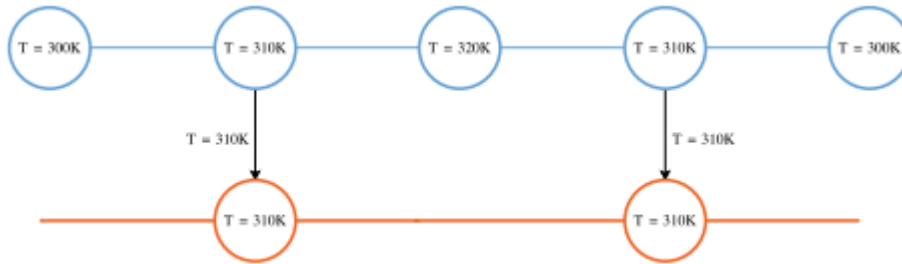


Figure 6.9: Consistent mapping scheme in preCICE Source: Chourdakis [3]

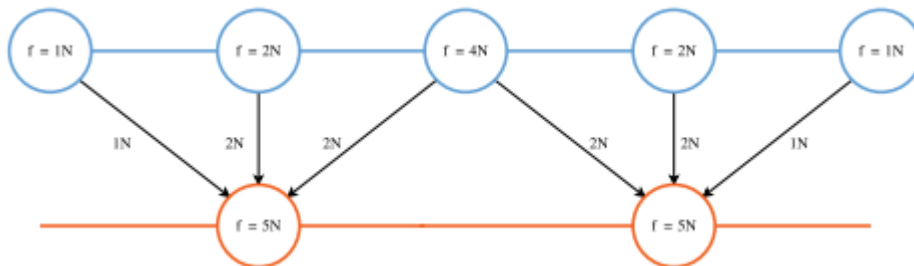


Figure 6.10: Conservative mapping scheme in preCICE Source: Chourdakis [3]

The following mapping methods are available (Chourdakis [3]):

- **Nearest neighbor** - Finds the closest point by Euclidian distance. It does not require any topological information and is first-order accurate.
- **Nearest projection** - Projects the target mesh points on the surface elements of the source mesh and assigns the interpolated values back on the target mesh. This method is second-order accurate. However, it requires topological information (surface mesh).
- **Radial Basis Function** - Constructs an interpolant on the source mesh using radial basis functions centered at the grid points and evaluates it at the target mesh. It requires no topological information. Installation of the PETSc library is necessary.

These mapping methods are available for both consistent and conservative mapping between meshes.

6.3 Mesh Convergence Studies

Mesh convergence studies were carried out primarily to analyse the required mesh density to capture orifice flow with sufficient accuracy. During this analysis, observations were also made regarding simulation time as a function of mesh size. The details of the simulation case are provided below:

6.3.1 Geometry

Given the fact that mesh convergence studies were performed to analyse the effect of mesh density on the flow through the piston orifice, it was decided to perform steady-state CFD simulations. However, the real piston geometry was unsuitable for this process due to the fact that the shims would always completely seal the piston orifices and a FSI simulation would be necessary to model shim deflection and hence obtain flow through the piston orifices. In order to work around this limitation, an alternate damper geometry was designed with the shims placed at a distance of 1.5 mm from the piston face, thus allowing for flow through the piston orifices. This modified configuration may be observed in Fig 6.11.

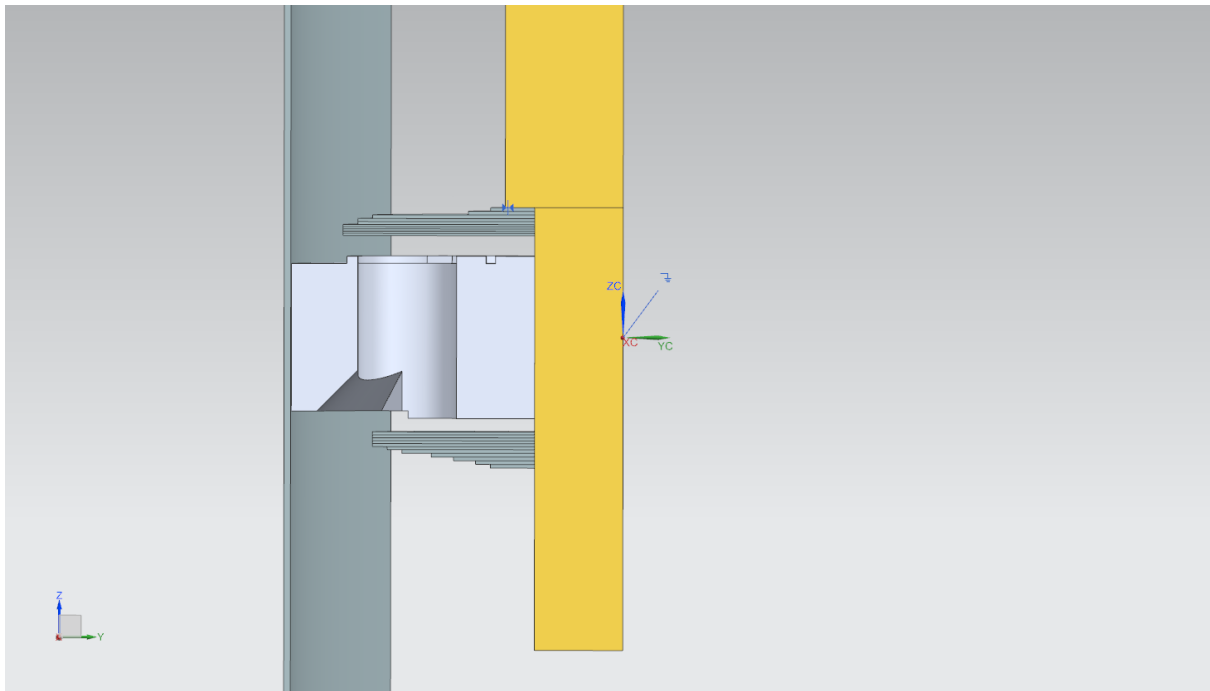


Figure 6.11: CAD assembly of the modified configuration with offset shim stacks

6.3.2 Mesh Generation

Seven meshes were generated on the basis of nodal spacing ranging from 0.2 mm–0.5 mm in increments of 0.05 mm. Uniform spacing was employed throughout the domain and tetrahedral volume meshes were generated. Details of the meshes are provided in Table 6.1:

Mesh Name	Nodal Spacing (mm)	Surface Trias	Volume Tetras
MC _{ele20}	0.20	382688	6540285
MC _{ele25}	0.25	244628	3860820
MC _{ele30}	0.30	170738	1932312
MC _{ele35}	0.35	125982	1177801
MC _{ele40}	0.40	96302	910558
MC _{ele45}	0.45	76336	616285
MC _{ele50}	0.50	62342	399686

Table 6.1: Details of meshes used for mesh convergence studies

Fig 6.12 shows the MC-ele20 mesh:

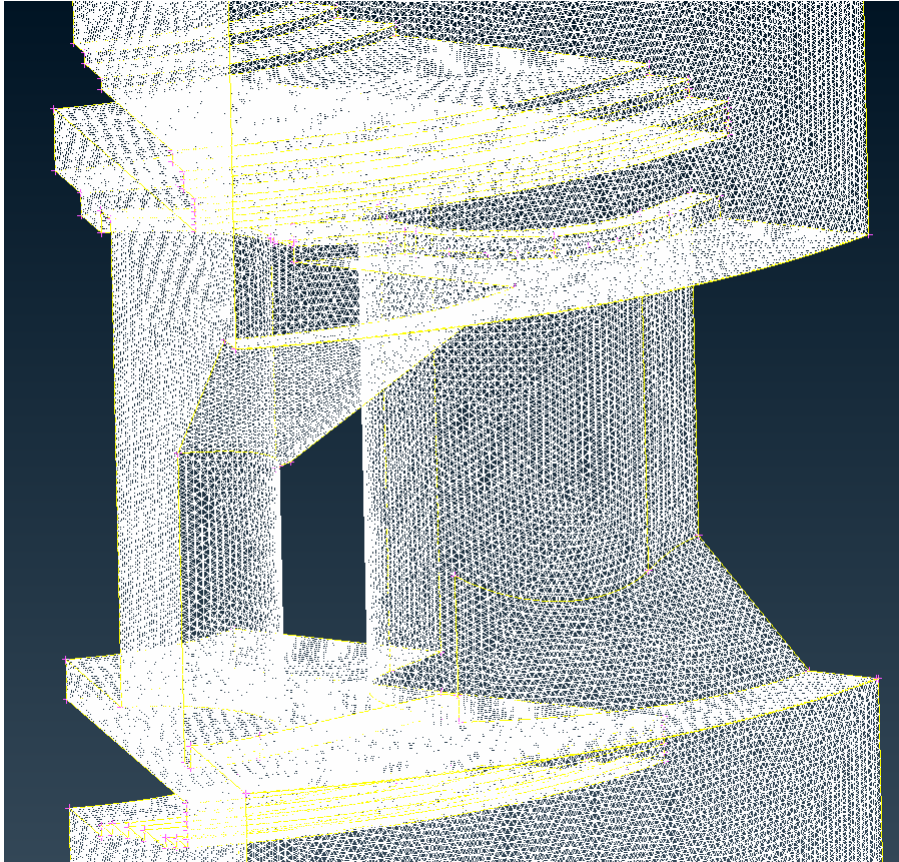


Figure 6.12: Details of generated mesh with an element size of 0.2 mm

6.3.3 Boundary Conditions

The damper was simulated for the case of the piston moving in rebound stroke. Thus, the end on the compression side of the damper was assigned a pressure of 14 MPa (as per the initial gas chamber pressure) with a zeroGradient (Dirichlet) boundary condition. The end on the rebound side of the damper was assigned a velocity inlet condition with a uniform velocity of 0.000 029 55 m/s with a zeroGradient (Dirichlet). This velocity was chosen under the assumption of an incompressible damper fluid and typical values for rod velocity and damping force from damper tests. The applied inlet velocity corresponds to a rod motion of 20 mm/s with a damping force of 100 N.

6.3.4 Solver Setup

Materials Setup

The damper fluid was modelled with a density of 843 kg/m³ and a kinematic viscosity of 14.443 m²/s.

Turbulence Modelling

The $k-\omega$ SST turbulence model was chosen considering the necessity of accurately simulating near-wall flow at the shim stack.

Solver

The OpenFOAM standard solver simpleFOAM was utilised. The simpleFOAM solver is an incompressible flow solver working with the SIMPLE algorithm for pressure-velocity coupling. The solver was run in all cases for 500 iterations.

6.3.5 Convergence Criterion

The principal goal of performing numerical simulations for this work is to obtain models that describe the flow rate through the piston orifice under various working states of the piston. Hence, the total flow rate through the piston orifices was considered as primary convergence criteria for mesh density.

6.3.6 Results

Volumetric Flow Rate through Piston orifices

The volumetric flow rate obtained by each mesh is detailed in Table 6.2:

Name	Tetrahedral Elements	Volumetric flow rate (m ³ /s)	Relative Perc. Error
MC _{ele20}	6540285	0.0000293596	0
MC _{ele25}	3860820	0.0000292805	-0.269418
MC _{ele30}	1932312	0.0000290975	-0.892723
MC _{ele35}	1177801	0.0000288965	-1.57734
MC _{ele40}	910558	0.0000288162	-1.85084
MC _{ele45}	616285	0.0000286296	-2.48641
MC _{ele50}	399686	0.0000283414	-3.46803

Table 6.2: Mesh convergence - volumetric flow rate results

Simulation time

In order to assess the dependence of simulation time on mesh size, all simulations were carried out on two computers - one equipped with a 2-core processor and the other equipped with a 4-core processor. The simulation times required by each machine for each mesh case is detailed in Table 6.3:

Mesh Name	Tetrahedral Elements	2 Core Sim time (s)	4 Core Sim time (s)
MC _{ele20}	6540285	12931	4749
MC _{ele25}	3860820	8708	2616
MC _{ele30}	1932312	3420	1171
MC _{ele35}	1177801	1918	658
MC _{ele40}	910558	1432	466
MC _{ele45}	616285	928	296
MC _{ele50}	399686	736	178

Table 6.3: Mesh convergence simulation times - 2 cores and 4 cores

Flow features

All simulations showed very similar flow features as can be observed in Fig. 6.13 to 6.19:

6.3. MESH CONVERGENCE STUDIES

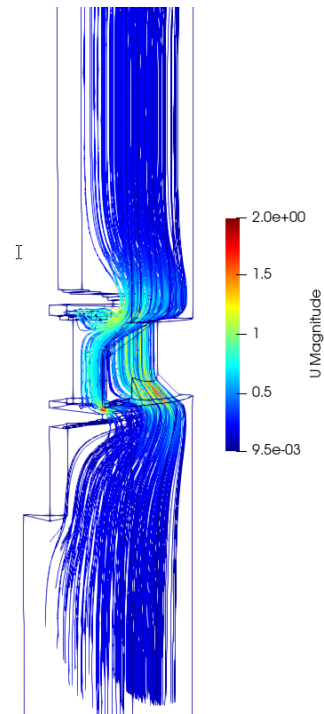


Figure 6.13: Streamlines for mesh with element length of 0.2 mm

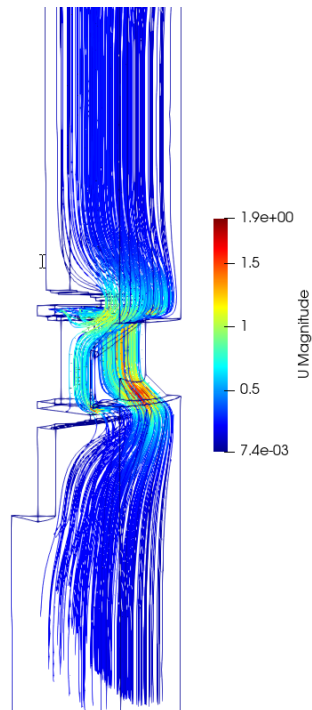


Figure 6.14: Streamlines for mesh with element length of 0.25 mm

6.3. MESH CONVERGENCE STUDIES

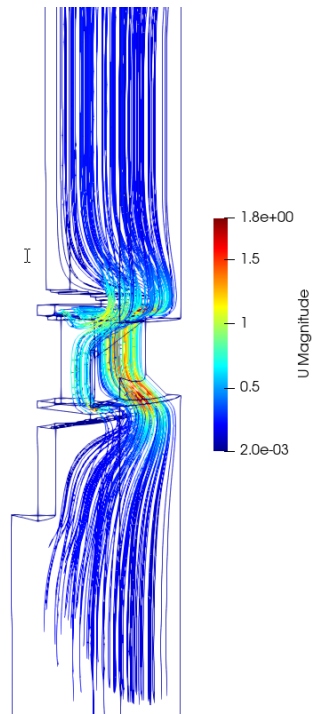


Figure 6.15: Streamlines for mesh with element length of 0.3 mm

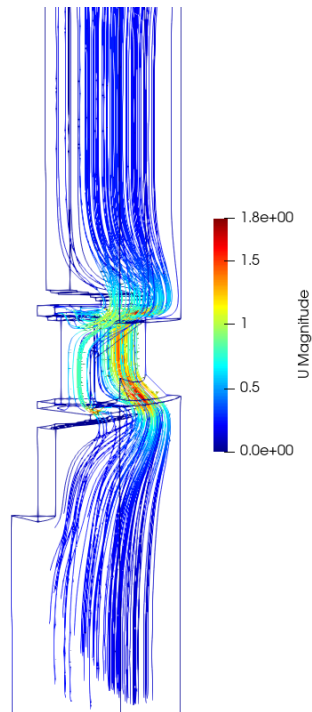


Figure 6.16: Streamlines for mesh with element length of 0.35 mm

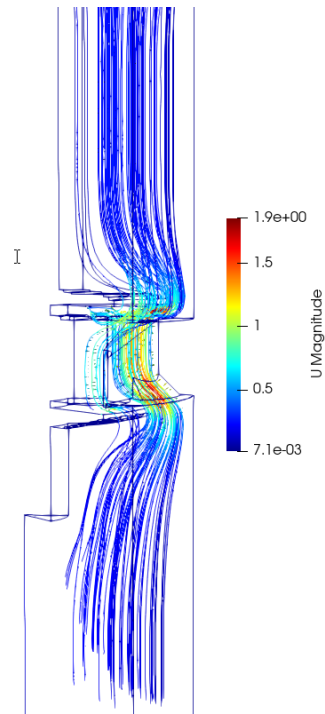


Figure 6.17: Streamlines for mesh with element length of 0.4 mm

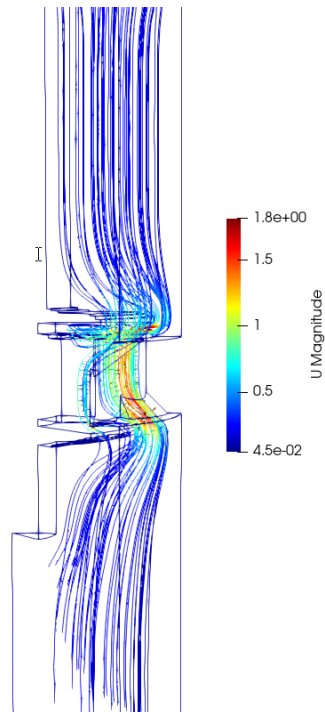


Figure 6.18: Streamlines for mesh with element length of 0.45 mm

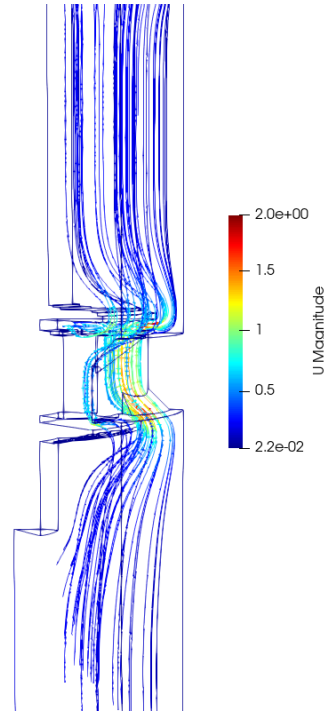


Figure 6.19: Streamlines for mesh with element length of 0.5 mm

6.3.7 Analysis

The simulation results were analysed according to the following criteria to determine an optimal mesh density for the final simulations. All the meshes showed very good agreement with each other on evaluation of the volumetric flow rate through the orifices and averaged pressure at the inlet. In order to better understand the smaller variations in flow fields between the meshes and to quantitatively capture the flow features resulting from the different meshes, it was decided to consider two additional criteria to gauge convergence: the ratio of volumetric flow rates between the compression and rebound orifice and the ratio of averaged pressures at the throats of the compression and rebound orifices.

Once convergence behaviour was studied, simulation time was used as a measure of the requisite computational power. During FSI simulations, the fluid solver is called upon to converge for multiple times for every time step and hence minimising the requisite computational resources is pivotal to executing practicable FSI simulations. An optimal mesh size was hence defined considering both the convergence criteria and the required computational resources per simulation.

Volumetric Flow Rate

The total volumetric flow rate through the piston orifices were determined and compared against the imposed volumetric flow rate. Fig 6.20 displays a graph of the percentage difference in flow rate with mesh density:

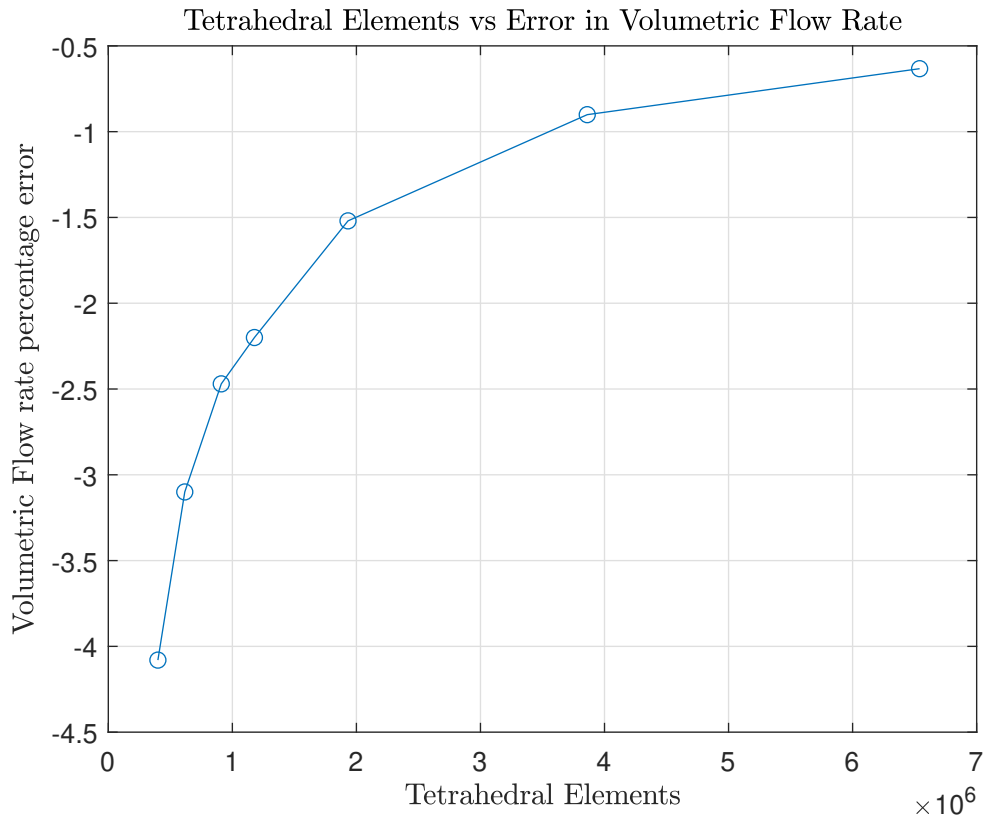


Figure 6.20: Error on imposed volumetric flow rate with mesh density

The maximum error was found to occur at the coarsest mesh as expected and was approximately 4%. It is observed that there is no significant gain in accuracy at mesh densities beyond 4 million elements. The error at 4 million elements is less than 1%.

Averaged Inlet Pressure

The imposed boundary condition for pressure at the inlet patch was a zeroGradient condition and hence it was decided to analyse the trend of averaged inlet pressures for all the meshes. A significant difference in inlet pressure would point to a big difference in the evaluated flow field and hence, it was decided to use averaged inlet pressures as one of the convergence criteria. Fig 6.21 shows a graph of the percentage difference in pressures with reference to the finest mesh:

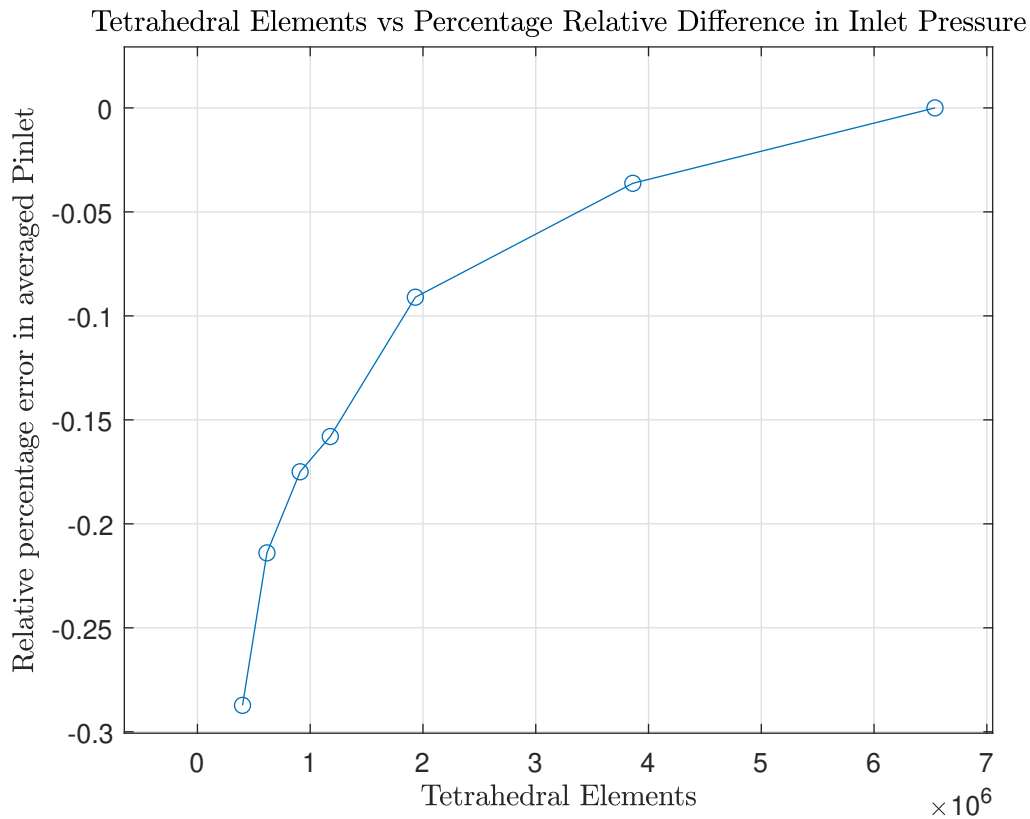


Figure 6.21: Difference in averaged inlet pressure relative to finest mesh with mesh density

The maximum error was found to occur at the coarsest mesh as expected with an error of 0.3%. It is observed that for all mesh densities above 2 million elements, the percentage difference was less than 0.1%.

Ratio of Volumetric Flow Rates

The volumetric flow rates through the compression and rebound piston orifices were evaluated. Fig 6.22 shows a graph of the ratio of volumetric flow rate through the compression orifice to that of the rebound orifice with respect to mesh density:

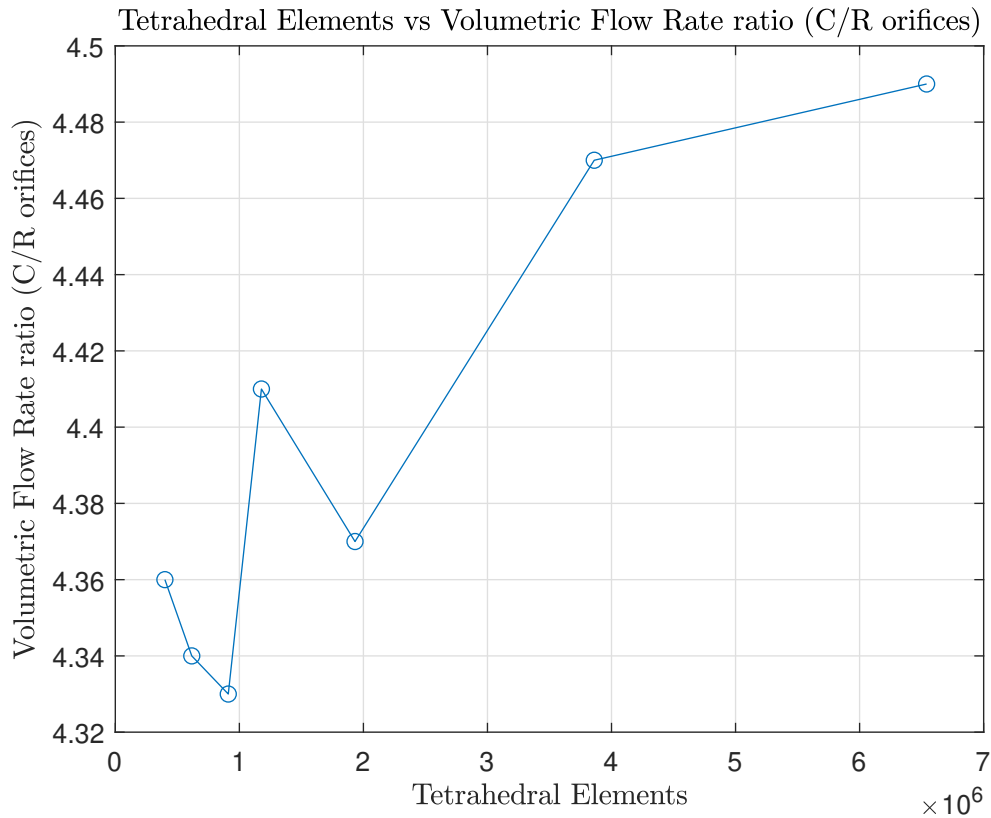


Figure 6.22: Ratio of Volumetric Flow Rates (C/R) with mesh density

The trend of the ratio displayed some oscillations for mesh sizes upto 2 million elements but was found to stabilise for mesh sizes of 4 million elements and above. This indicated possible variation in flow features in the coarser meshes. The stabilisation post 4 million elements is a good indicator of convergence.

Ratio of Averaged Pressures

The averaged pressures through the compression and rebound piston orifices were evaluated at the piston mid-plane. Fig 6.23 shows a graph of the ratio of pressure at the mid-plane of the compression orifice to that of the rebound orifice with respect to mesh density:

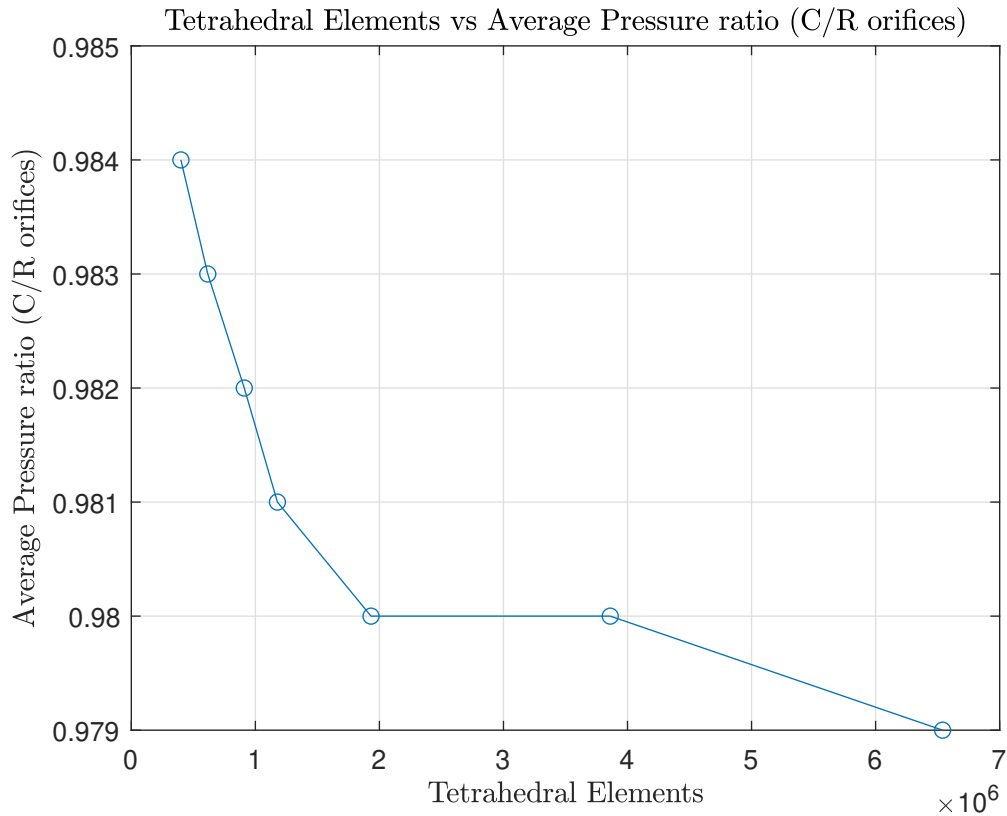


Figure 6.23: Ratio of Averaged Pressures (C/R) with mesh density

The trend of the ratio displayed some oscillations for mesh sizes upto 2 million elements but was found to stabilise for mesh sizes of 4 million elements and above. This indicated possible variation in flow features in the coarser meshes. The stabilisation post 4 million elements is a good indicator of convergence.

Simulation Time

Find below a graph of CPU time for the mesh convergence trials as a function of the number of cores:

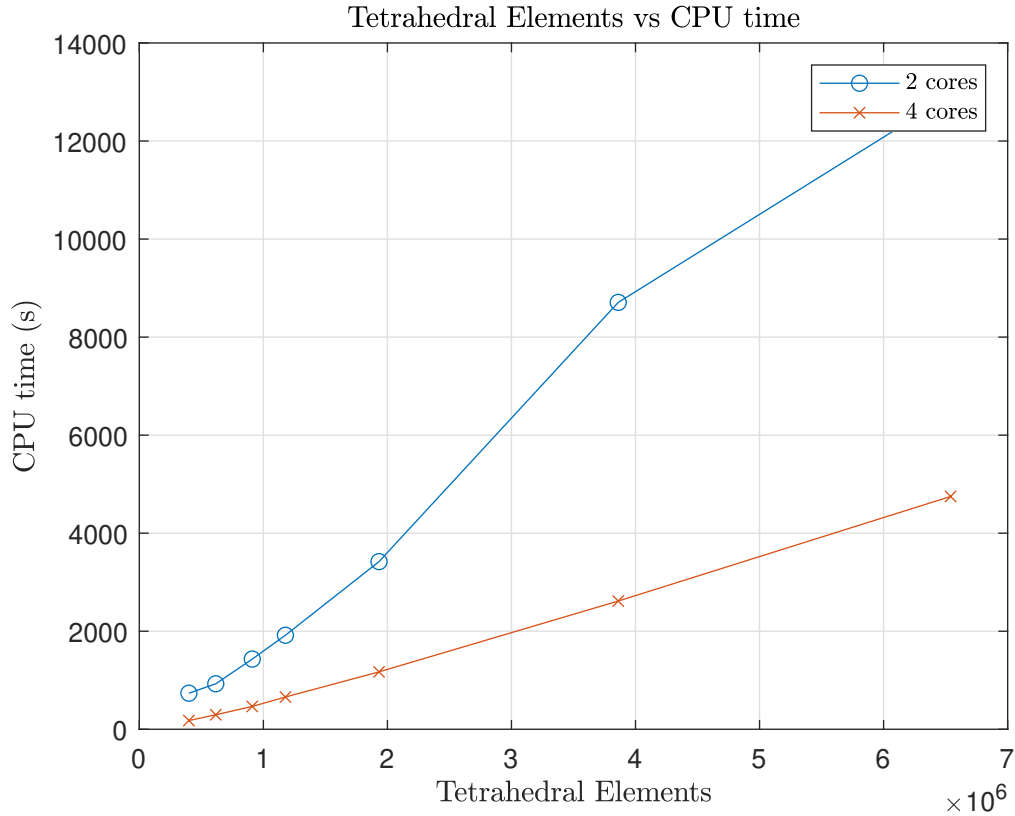


Figure 6.24: Simulation time vs. number of cores

The simulation times were found to converge to a quasi-linear trend for the 4-core machine while the 2-core machine displayed non-linearity. Since a 4-core machine was available for all simulations for this work, the choice of mesh density was based on data only from the 4-core machine.

6.3.8 Conclusions

An optimal mesh density of 4 million elements was determined considering the convergence criteria based on flow properties as well as simulation time. This translates to a nodal spacing of 0.25 mm. Such a mesh provides acceptable accuracy while affording practical run-time for convergence.

6.4 FSI trials using a simple geometry

In order to finalise the solver coupling scheme and relevant parameters and to gauge computational requirements, FSI simulations were initially carried out with a simple geometry. The simple geometry consisted of compression and rebound chambers identical to the real geometry, a simple piston with planar piston faces, a single piston orifice and a single shim offset 2 mm from the piston face. This simplified geometry is shown in fig 6.25.

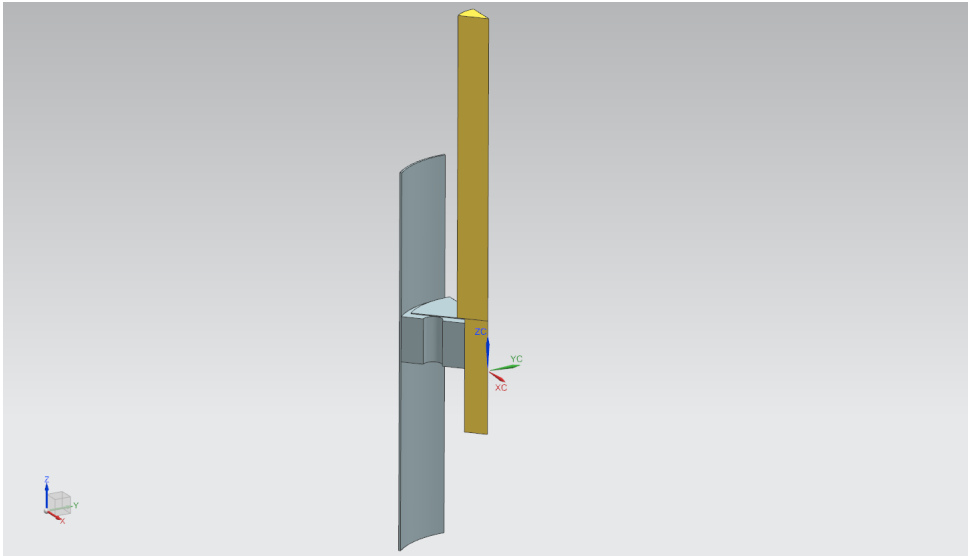


Figure 6.25: Geometry used for trial FSI simulations

6.4.1 Mesh

The fluid mesh for the simple geometry consisted of $\approx 100,000$ tetrahedral elements. An image of the mesh is provided in fig 6.26.

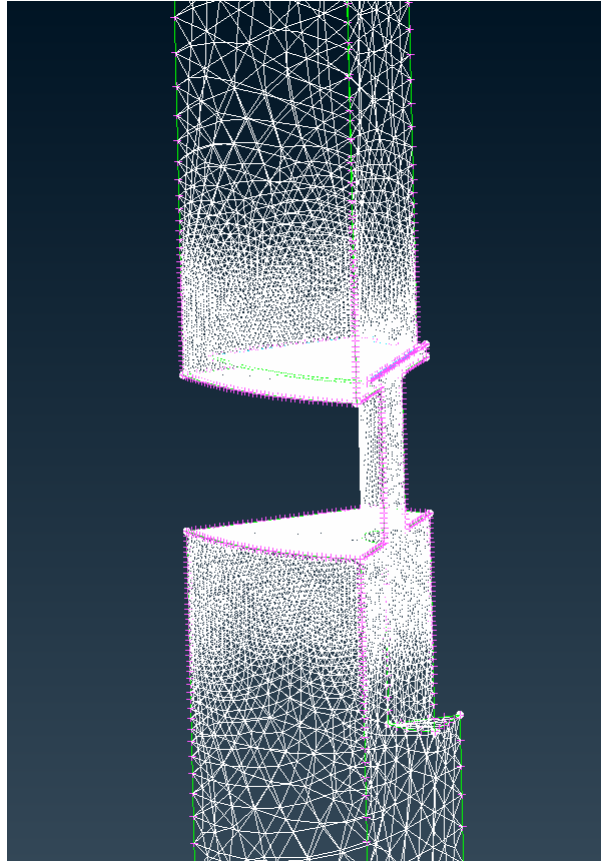


Figure 6.26: Fluid mesh used for trial FSI simulations

The fluid mesh for the simple geometry consisted of $\approx 4,000$ tetrahedral elements. An image of the mesh is provided in fig 6.27.

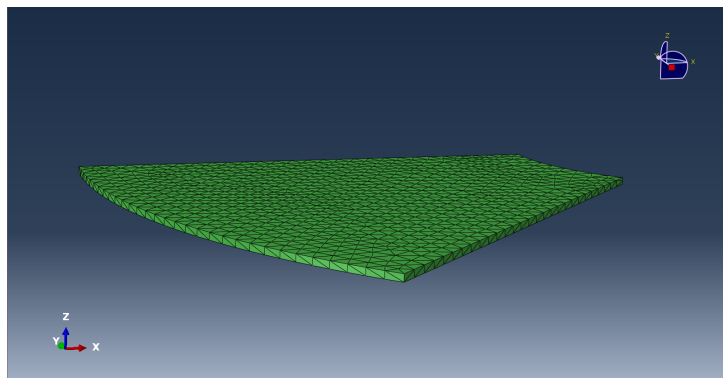


Figure 6.27: Solid mesh used for trial FSI simulations

6.4.2 Simulation Setup

Boundary Conditions

The following boundary conditions were imposed on the flow domain:

Boundary	Velocity	Pressure
Inlet	fixedValue = 0.05 m/s	zeroGradient
Outlet	zeroGradient	fixedValue = 1.5×10^7 Pa

Solver Parameters

The pimpleFoam solver was used with a time step of 1×10^{-9} s with the following parameters:

- nOuterCorrectors = 30
- nCorrectors = 3
- nNonOrthogonalCorrectors = 1
- momentumPredictor = true

The forward Euler scheme was used for time stepping. The case was solved for laminar flow in order to minimise computational time. The simulation was run for 5,500 iterations.

6.4.3 Coupling Setup

Coupling Scheme

The parallel-implicit scheme described in [6.2.3 on page 37](#) was found to result in a stable and convergent simulation. Both the serial-explicit and parallel-explicit schemes resulted in coupling divergence. The serial-implicit scheme was not used since it is inferior in performance to the parallel-implicit scheme [\[39\]](#).

An absolute convergence measure of 1×10^{-2} was imposed on both forces and deflections as convergence criteria. In order to minimise computational time, the nearest-neighbor mapping scheme was used for data exchange between the domains.

Acceleration Scheme

In order for implicit coupling to be effective, it is necessary to use an acceleration scheme [\[40\]](#). The Constant Under-Relaxation, Dynamic Aitken Under-Relaxation and quasi-Newton Anderson acceleration schemes resulted in coupling divergence. A stable simulation was obtained by using the quasi-Newton generalized Broyden acceleration scheme with a QR2 filter. The acceleration scheme setup used was:

```

1 <acceleration:IQN-IMVJ>
2     <data name="Displacements" mesh="Calculix_Mesh"/>
3     <preconditioner type="residual-sum"/>
4     <filter type="QR2" limit="1e-3"/>
5     <initial-relaxation value="0.1"/>
6     <max-used-iterations value="100"/>
7     <time-windows-reused value="10"/>
8 </acceleration:IQN-IMVJ>

```

6.4.4 Results

Simulation Convergence

The residual plots for the fluid simulation is shown in Fig. 6.28:

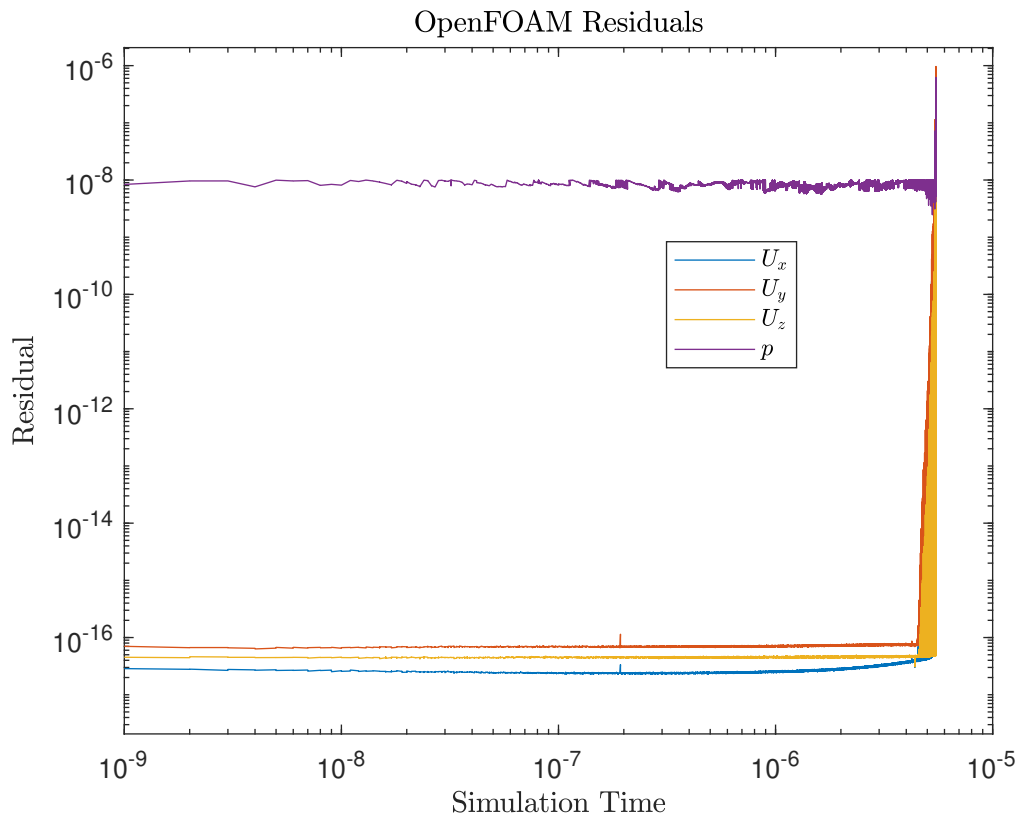


Figure 6.28: Fluid solver residuals for the trial FSI simulation

CalculiX ensures convergence at every coupling run with internal convergence criteria [41]. The plot for number of iterations to satisfy the convergence criteria at each time step for the structural simulation is shown in Fig. 6.29:

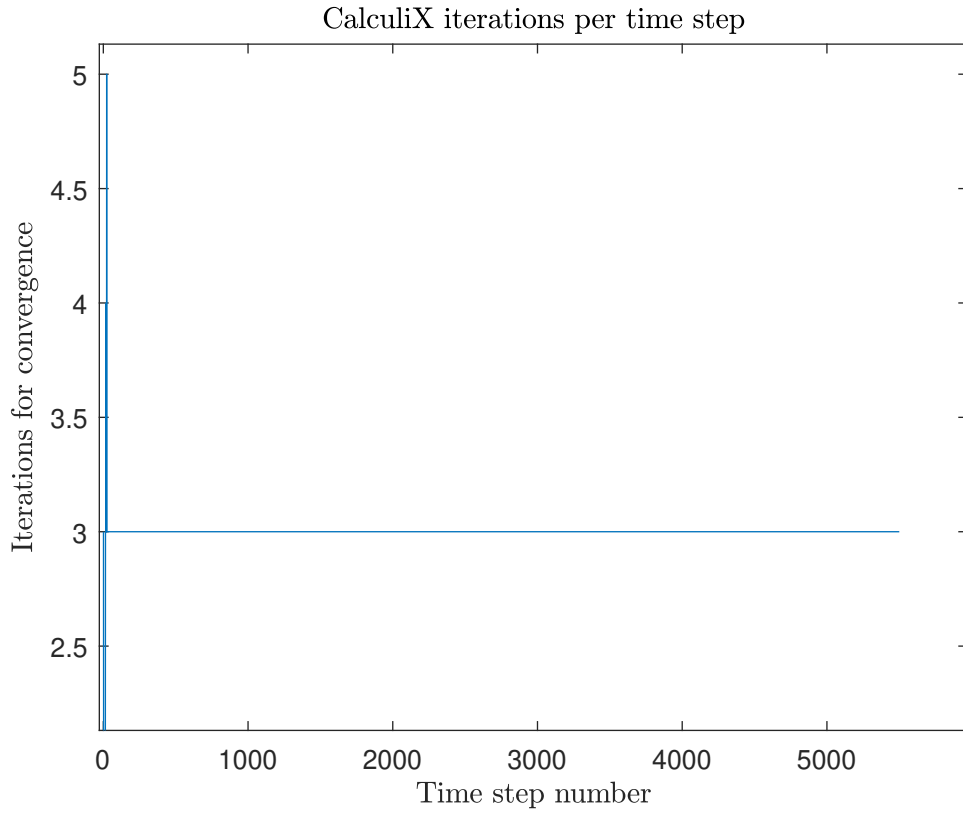
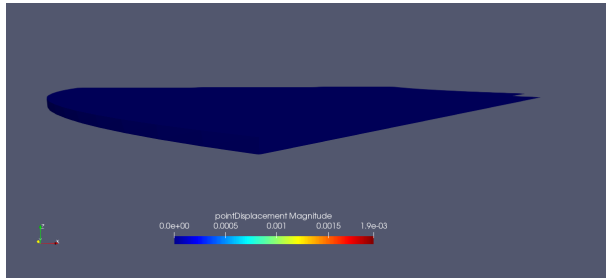


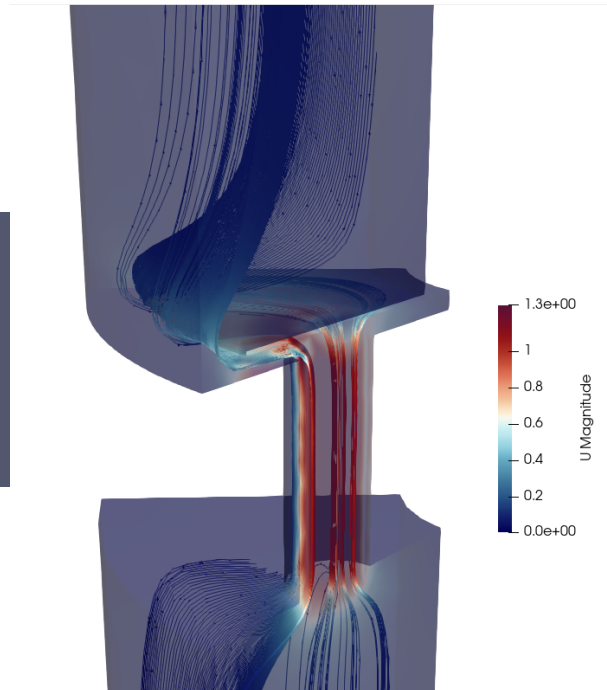
Figure 6.29: Structural solver residuals for the trial FSI simulation

Streamlines and Shim Deflection

Streamlines and the shape of the deformed shim are displayed for the first time iteration ($t = 1 \times 10^{-9}$ s) and then at an interval of 50 iterations after iteration 3,000 ($t = 3 \times 10^{-6}$ s), when the fluid-structure coupling is evident.

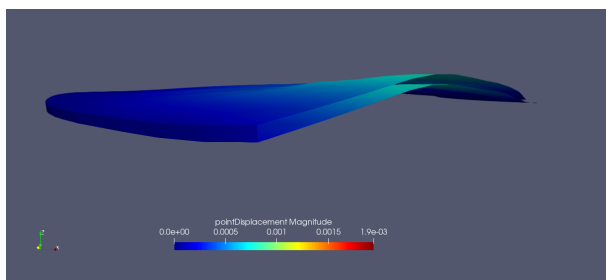


(a) Shim deformed shape at $t = 1 \times 10^{-9}$ s

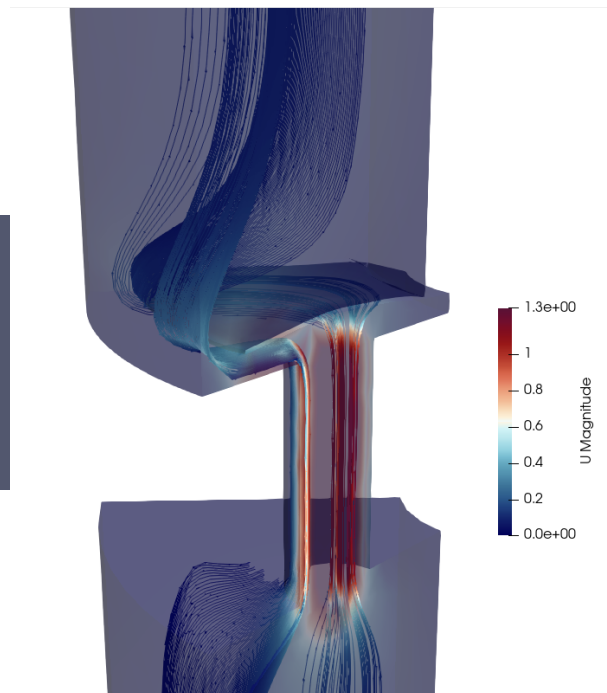


(b) Streamlines at $t = 1 \times 10^{-9}$ s

Figure 6.30: Coupled solution at $t = 1 \times 10^{-9}$ s

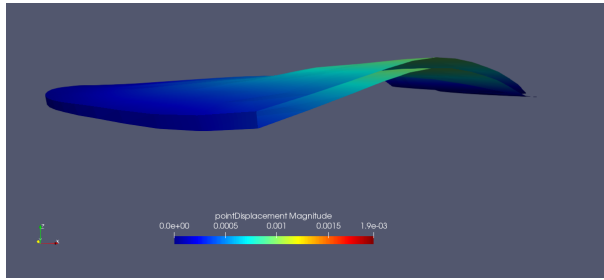


(a) Shim deformed shape at $t = 3 \times 10^{-6}$ s

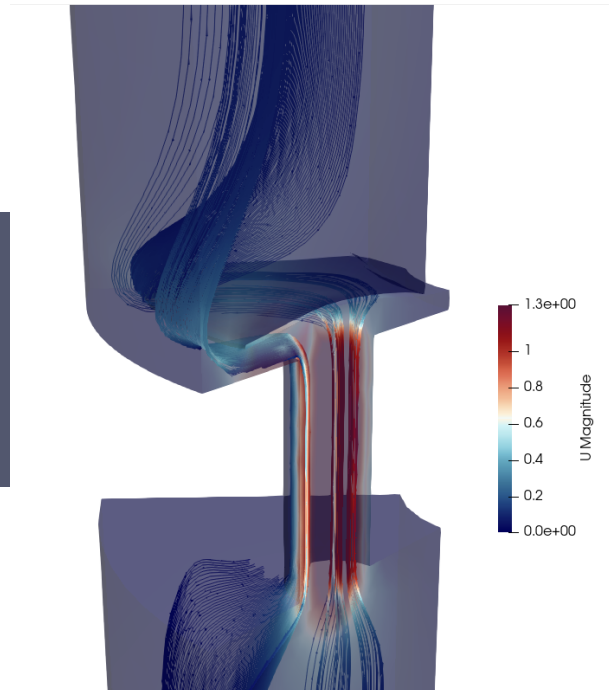


(b) Streamlines at $t = 3 \times 10^{-6}$ s

Figure 6.31: Coupled solution at $t = 3 \times 10^{-6}$ s

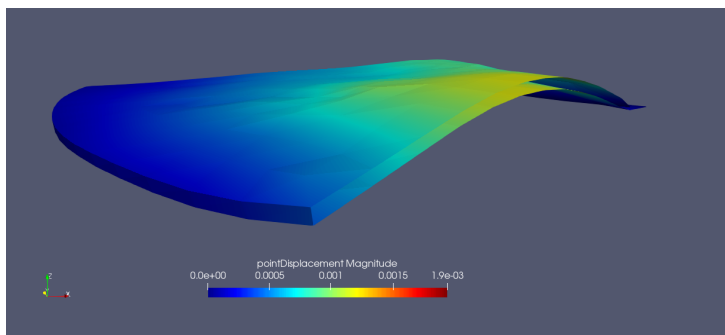


(a) Shim deformed shape at $t=3.5 \times 10^{-6}$ s

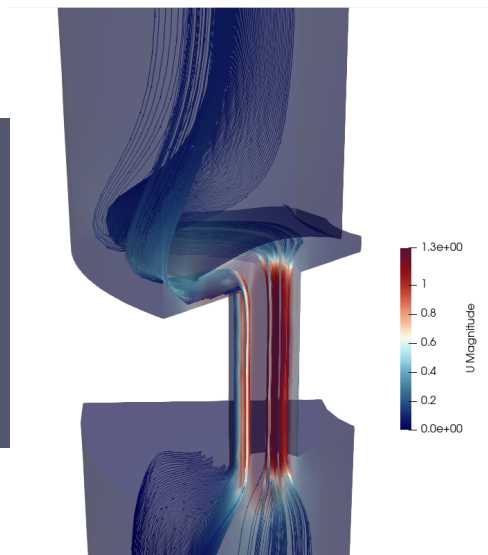


(b) Streamlines at $t=3.5 \times 10^{-6}$ s

Figure 6.32: Coupled solution at $t=3.5 \times 10^{-6}$ s

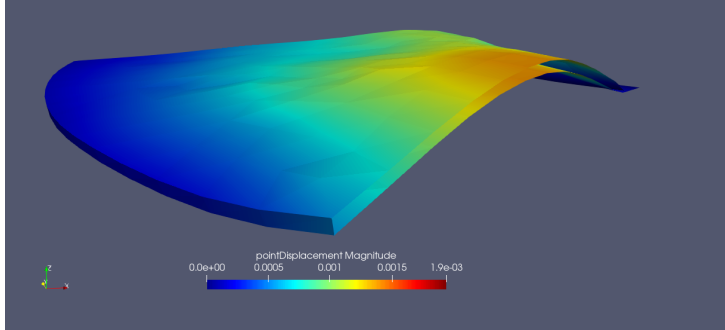


(a) Shim deformed shape at $t=4 \times 10^{-6}$ s

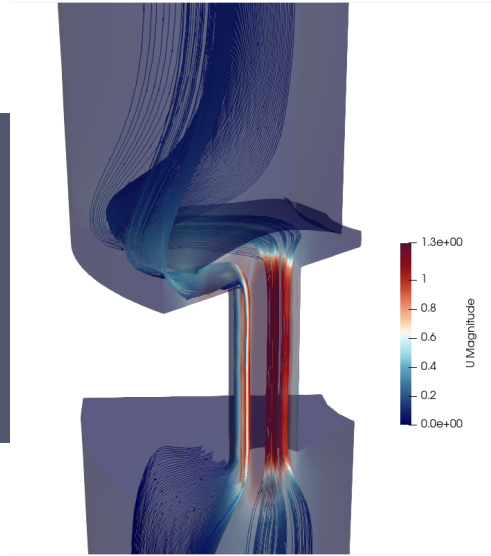


(b) Streamlines at $t=4 \times 10^{-6}$ s

Figure 6.33: Coupled solution at $t=4 \times 10^{-6}$ s

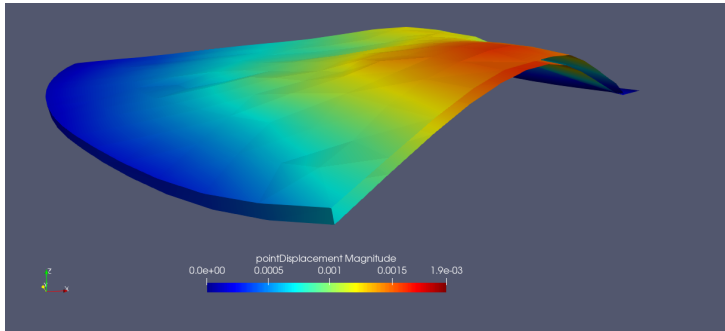


(a) Shim deformed shape at $t=4.5 \times 10^{-6}$ s

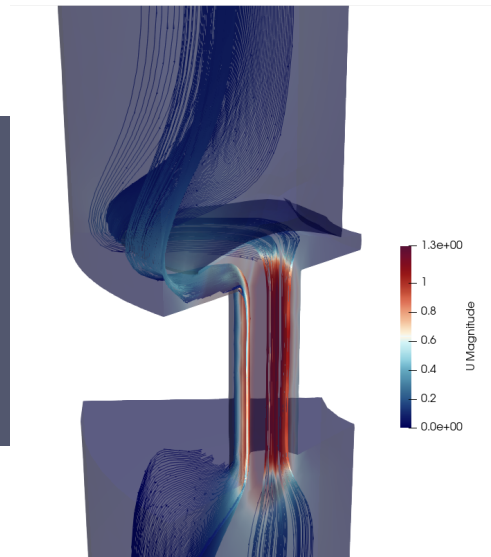


(b) Streamlines at $t=4.5 \times 10^{-6}$ s

Figure 6.34: Coupled solution at $t=4.5 \times 10^{-6}$ s

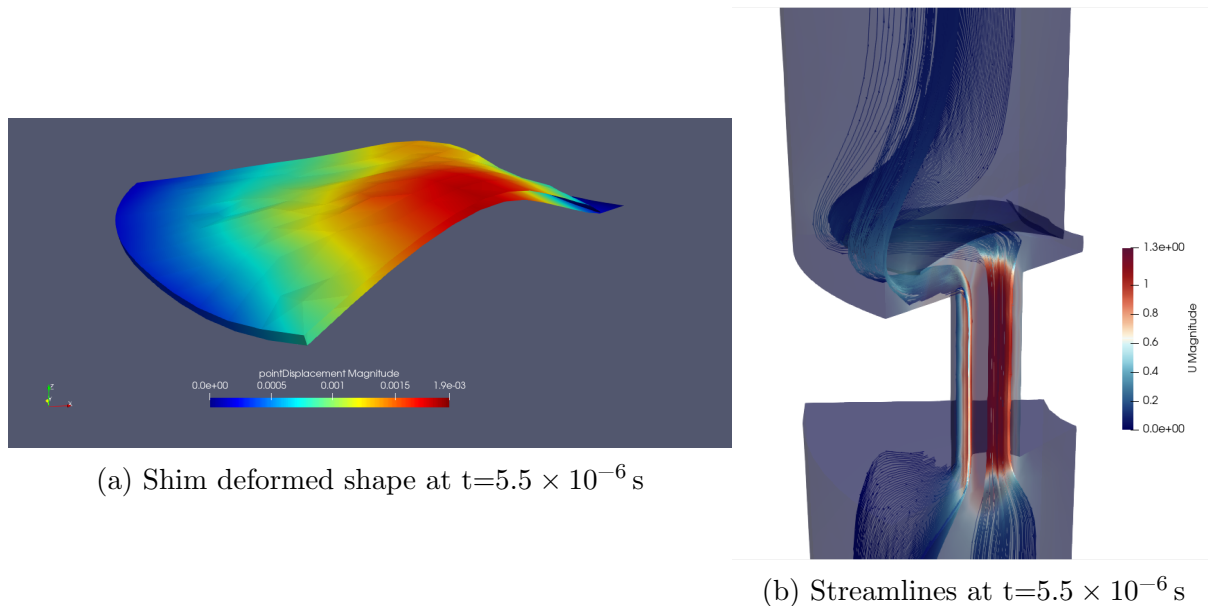


(a) Shim deformed shape at $t=5 \times 10^{-6}$ s



(b) Streamlines at $t=5 \times 10^{-6}$ s

Figure 6.35: Coupled solution at $t=5 \times 10^{-6}$ s

Figure 6.36: Coupled solution at $t=5.5 \times 10^{-6}$ s

6.5 FSI Trials on Real Geometry

On attempting to perform FSI simulations on the real damper geometry, the following observations were made:

- **Coupling Scheme:** The coupling scheme and parameters for the quasi-Newton acceleration scheme that were stable for the trial geometry were observed to induce divergence in the coupled simulation. It is hence required to find the optimal acceleration scheme and tuning parameters.
- **CalculiX EXPLICIT Solver:** During operations, shims slide over each other in addition to deflecting and this phenomenon must be simulated in order to obtain realistic behaviour. If the sliding is not considered, the shim stack would be treated as a solid block of the same volume and such a structure would provide a greater stiffness. In order to simulate sliding contact in a numerically stable manner, it is necessary to utilise the CalculiX EXPLICIT dynamic solver, which, on account of its conditional stability, limits the simulation time-step. In addition, the definition of sliding contact pairs at every shim interface greatly increases the time and effort required for pre-processing the structural case.
- **Simulation Time:** Due to the use of the explicit dynamics solvers and due to higher mesh sizes, the simulation time for the real geometry was found to be significantly higher than that required for the trial geometry.
- **Development of a custom OpenFOAM solver:** The current simulation setup employs the transient solver pimpleFoam as the CFD solver. However, for the current mathematical model, the dynamics of the shim stack are not necessary and the final equilibrium state would suffice, thus reducing simulation time and

computational resources. Obtaining such a solution requires the use of a steady-state CFD solver (simpleFoam, for example). This proved to be an issue since steady-state OpenFOAM solvers do not support dynamic meshes which is necessary to impose the motion of the shim stack. Therefore, for this mathematical model, it would be greatly advantageous to develop a custom steady-state CFD solver capable to handling dynamic meshing.

Due to a combination of lack of time and computational resources, and the above mentioned factors, FSI simulations on the real damper geometry could not be performed.

7

Experimental Trials

7.1 Trial Damper

A test monotube damper developed for road-going automobile application was used for experimental validation. A photo of the damper is found in Fig. 7.1:



Figure 7.1: Test automotive monotube damper

7.1. TRIAL DAMPER

The test damper uses the piston shown below:



(a) Piston - Rebound chamber side (b) Piston - Compression chamber side

Figure 7.2: Main Piston of the test damper

The valving configuration for the test damper was as below:

Shim Stacks			
Compression Stack		Rebound Stack	
Diameter (mm)	Thickness (mm)	Diameter (mm)	Thickness (mm)
38	0.15	34	0.20
38	0.15	34	0.20
38	0.15	34	0.20
38	0.15	34	0.20
38	0.15	34	0.20
38	0.15	32	0.20
36	0.20	30	0.25
36	0.20	26	0.25
34	0.25	23	0.25
30	0.25	20	0.25
26	0.25	18	0.25
21	0.25		
18	0.25		

Table 7.1: Damper Valving Specification

7.2 Experimental Setup

The UK4kw suspension dynamometer provided by Umbria Kinetics was used for experimental trials [42]. The dynamometer consists of a 4 kW electric motor driving a crankshaft and a kinematic chain that translates rotary motion of the crankshaft into alternating linear motion. This linear motion is transmitted to the lower mounting fixture to which the damper is anchored. The damping force generated by the damper is measured using load cells placed in the upper mounting fixture. The displacement and instantaneous velocity of the system is calculated using an external set of sensors and relayed to an electronic control unit. The dynamometer is capable of producing damper excitation velocities up to 2 m/s. A photo of the UK4kw dynamometer with the test damper mounted is shown in Fig. 7.3:



Figure 7.3: Test damper mounted on the UK4kw suspension dynamometer

7.3 Data Acquisition Scheme

The data acquired by the on-board sensors can be accessed via the proprietary Umbria Kinetics DynoSoft software. The suspension dynamometer is capable of connecting to a PC via either a serial port or a USB port using the provided USB/Serial converter. A schematic of the Umbria Kinetics DynoSoft software graphical user interface is shown below in Fig. 7.4:



Figure 7.4: Umbria Kinetics DynoSoft software graphical user interface

7.4 Data Points

The damper was tested over the following velocity stencil :

- 20 mm/s
- 50 mm/s
- 75 mm/s
- 100 mm/s
- 150 mm/s
- 200 mm/s
- 250 mm/s
- 300 mm/s

7.4. DATA POINTS

The damper was tested for the following bleed valve positions:

- Fully closed bleed valve
- 1 click from fully closed position
- 3 clicks from fully closed position
- 5 clicks from fully closed position
- 10 clicks from fully closed position
- 15 clicks from fully closed position
- 20 clicks from fully closed position
- Fully open bleed valve (≈ 40 clicks from fully closed position)

In order to delay cavitation, a critical phenomenon while operating at low bleed valve openings, the damper was allowed sufficient time to dissipate heat post every run.

8

Results

8.1 Mathematical Sub-Models

8.1.1 Shim Valve Discharge Coefficient

Steady state CFD simulations were performed using the OpenFOAM solver simpleFoam in order to evaluate the discharge coefficient in the absence of FSI data. The structural solver detailed in 3.1.5 was used to obtain the axis-symmetric deformed shape of the shim stack, which was then reproduced as 3-dimensional geometry and assembled with the rest of the damper CAD model. The C_D was modelled as a linear function of the pressure differential between the compression and rebound chambers in order to obtain a look-up table for the discharge coefficient as a function of the pressure differential. The discharge coefficient was then evaluated as:

$$C_D = Q_{CFD}/Q_{Ideal} \quad (8.1)$$

where Q_{Ideal} is the ideal flow rate through the orifice, defined as:

$$Q_{Ideal} = A_{orifice} \cdot \sqrt{\frac{2 \cdot \Delta P}{\rho}} \quad (8.2)$$

where ΔP is the pressure differential across the compression and rebound chambers, ρ is damper oil density and $A_{orifice}$ is the total available orifice flow area.

Streamlines obtained for a pressure differential of 10 MPa may be found below in Fig. 8.1

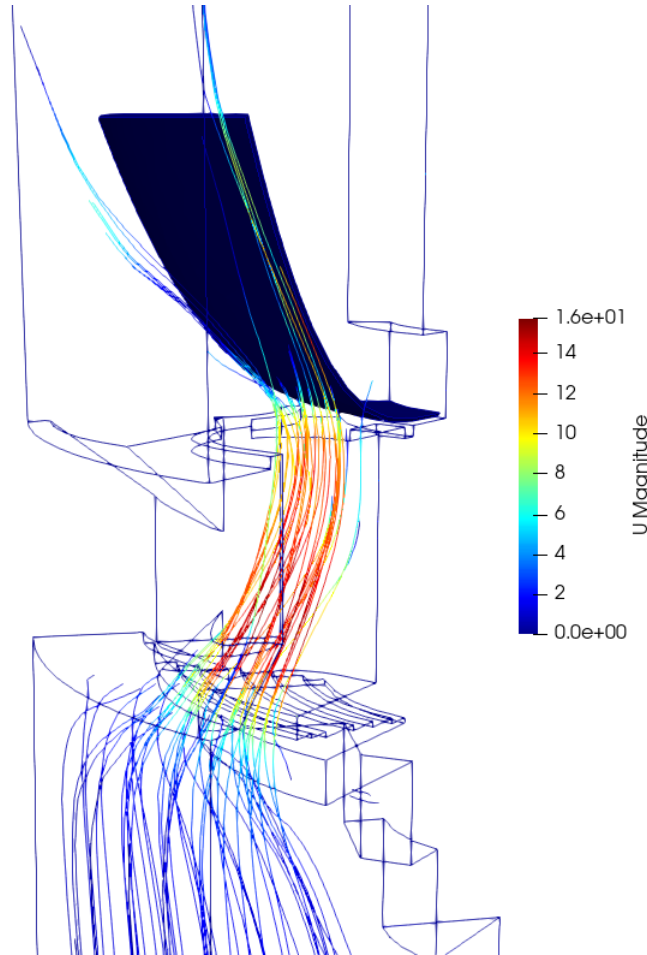


Figure 8.1: Streamlines obtained for a 10 MPa pressure differential using Force method predicted shim deflection

The following look-up tables were hence generated for the compression and rebound strokes respectively:

Pressure Differential	C_D
0 MPa	0
10 MPa	0.95

Table 8.1: Discharge coefficient look-up table for compression stroke

Pressure Differential	C_D
0 MPa	0
10 MPa	0.85

Table 8.2: Discharge coefficient look-up table for rebound stroke

In addition, the mathematical model was also analysed with a constant C_D of 0.7 as suggested by Talbott and Starkey [1].

8.1.2 Shim Stack Displacement Model

The force method model described in 3.1.5 was used to study the shim deflection behaviour as function of the applied pressure differential. Typical values of steel were used as material properties. viz. Young's modulus (E) = 200 GPa and Poisson's ratio (ν) of 0.3. A plot of the obtained result is shown below in Fig. 8.2

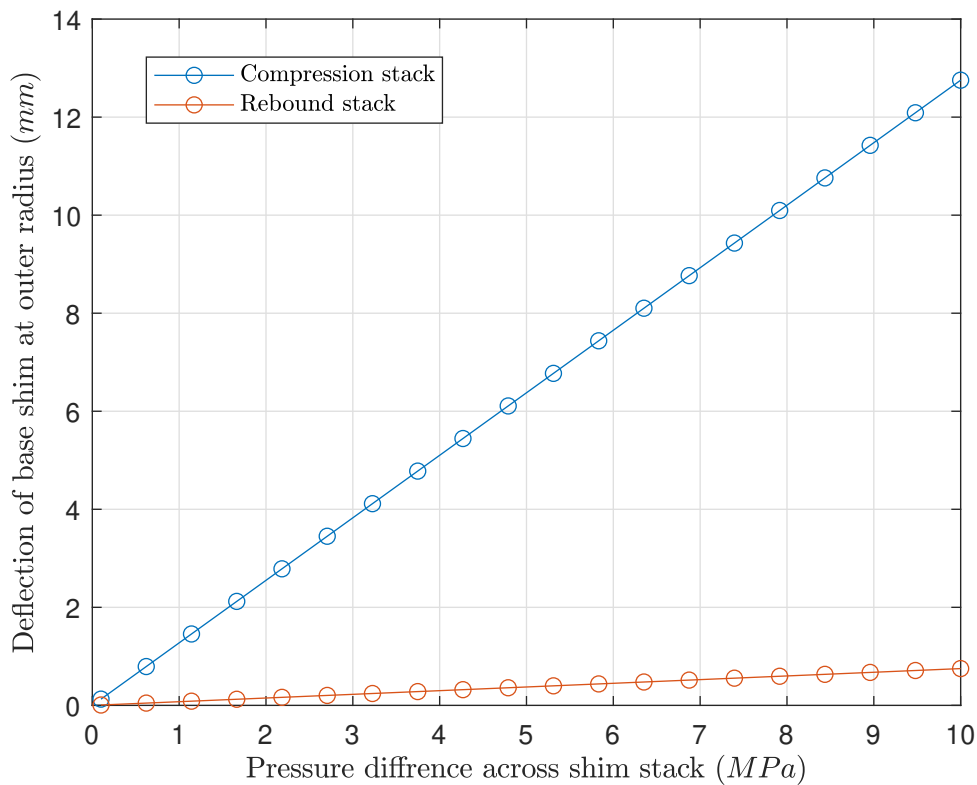


Figure 8.2: Shim deflections of the compression and rebound stack computed using the Force method vs. applied pressure difference

The shim deflections display a linear trend with respect to the applied pressure differential. In order to visualise the deflections for pressure differentials of the order 0.1MPa , the data is plotted on a log-log scale in Fig. 8.3 below:

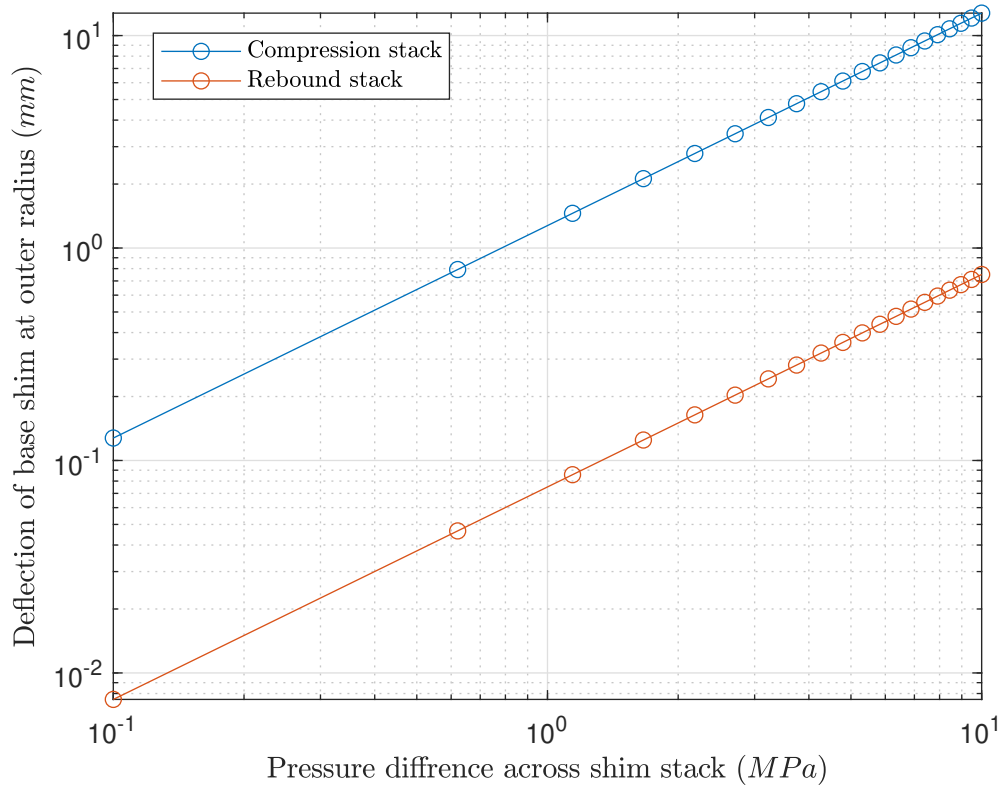


Figure 8.3: log-log plot of shim deflections of the compression and rebound stack computed using the Force method vs. applied pressure difference

It is observed that in the general case, the deflections fit exponential functions, i.e. functions of the form $y = a \cdot \Delta P^n$, thus lending to be modelled in a convenient manner and a simple function may be used instead of a time and computational resource consuming solver. The stacks can be modelled by the same value for the exponent (n) but differing in the value of the constant (a) as evidenced by the difference in y-intercepts. In this case, it is observed that $n \approx 1$. It is also observed that the rebound shim stack is much stiffer than the compression shim stack.

However, it was also observed that, due to incompatibility in boundary conditions between successive plates, nonphysical behaviour was reported by the solver. Consider the deflected compression shim stack for an applied pressure differential of 10 MPa. Note: The vertical positions of the shims in Fig. 8.4 is not to scale.

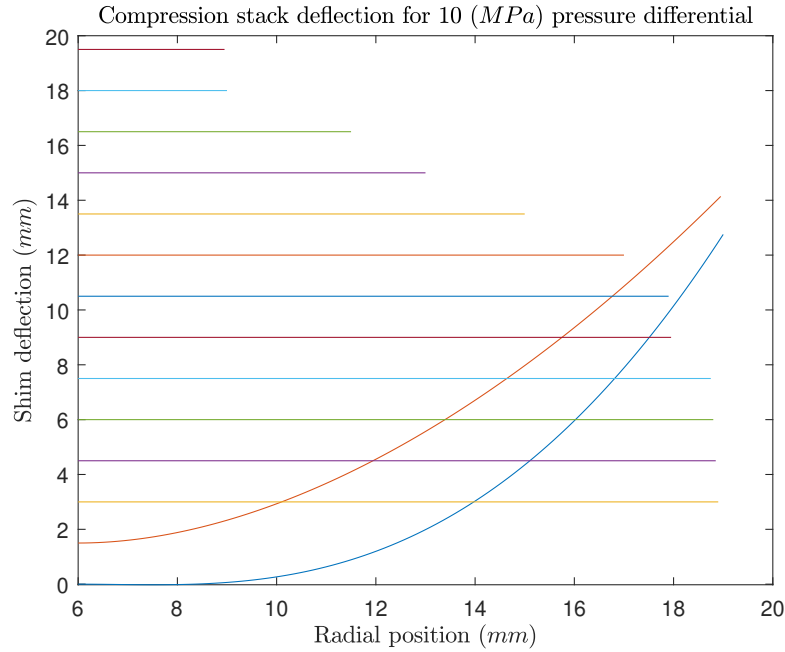


Figure 8.4: Deflected compression shim stack shape for a pressure differential of 10 MPa as predicted by the Force method

This nonphysical behaviour arises from the fact that displacement compatibility is enforced only at the point of contact of two shims and the fact that boundary conditions are applied to each shim individually. Hence, the model must be considered for improvement to be capable of modelling the deflection of the entire stack in a homogeneous manner.

For the purposes of the current mathematical model, however, only the deflection of the base shim at its outer radius is the extracted parameter and this deflection exhibits a trend that would appear physical. However, it is recommended to validate the complete force method model with either well resolved FSI simulations or experiments.

For application in the MATLAB model, it was required to specify a single equivalent stiffness for each shim stack. According to the deflection trend in Fig. 8.2, a single value per stack was sufficient to characterise the stack stiffnesses. These values were computed as:

$$k_{stack} = \frac{\Delta P \cdot A_{firstshim}}{y_{stack}} \quad (8.3)$$

The resultant stiffness values are shown in Table 8.3 below:

Shim Stack	Stiffness N/m
Compression Stack	1.778×10^5
Rebound Stack	2.419×10^6

Table 8.3: Equivalent Shim Stack Stiffnesses

8.2 Experimental Results

The obtained Force-Velocity curves for the test damper are shown below in Fig.8.5:

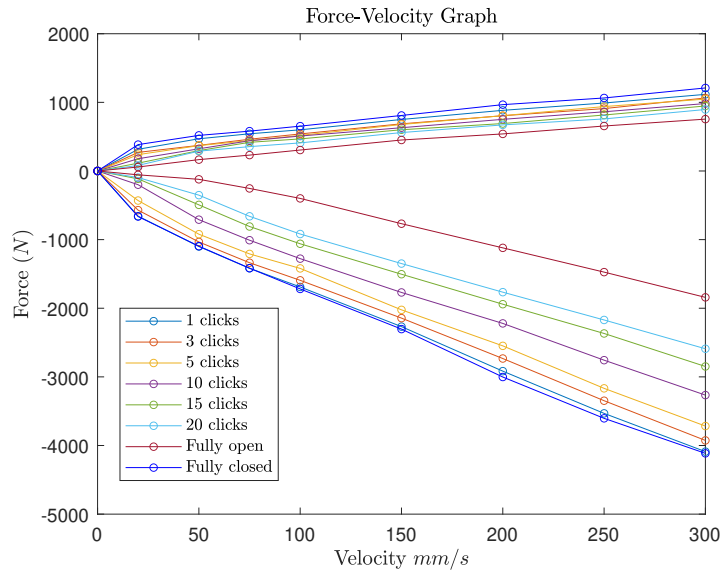


Figure 8.5: Experimental Force-Velocity graph

The obtained Displacement-Force curves for the test damper in the case of the bleed valve being fully shut is shown in Fig. 8.6

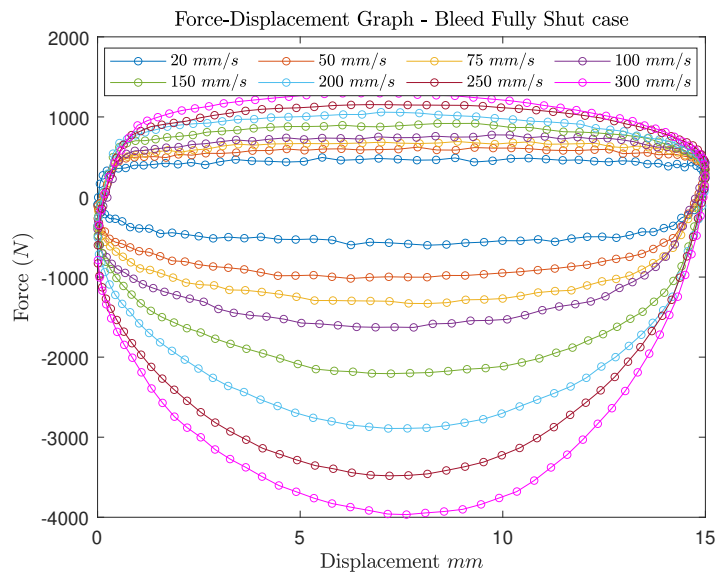


Figure 8.6: Experimental Displacement-Force graph in the case of fully closed bleed valve

8.3 Simulink Model Results

8.3.1 Model Output

The Simulink model was run for a sinusoidal forcing amplitude of 15 mm at a frequency of 100 Hz and the results are as shown below:

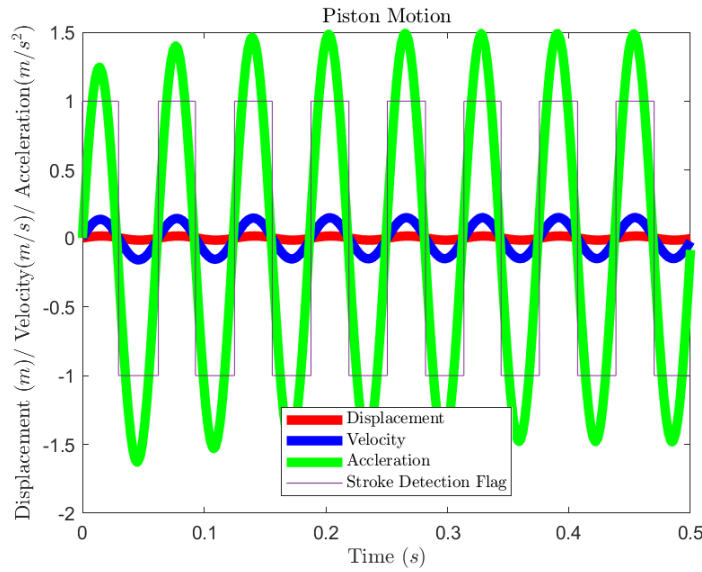


Figure 8.7: Main piston displacement, velocity, acceleration and velocity-based stroke detection flag for oscillation at 100 Hz

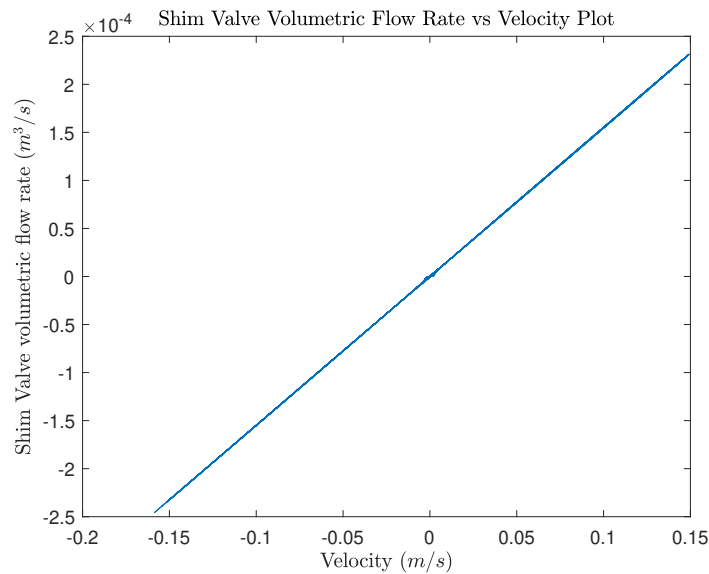


Figure 8.8: Shim valve volumetric flow rate vs main piston velocity for oscillation at 100 Hz

8.3. SIMULINK MODEL RESULTS

The piston is observed to undergo alternating linear motion as unexpected.

The volumetric flow rate through the shim valves exhibits a linear trend with main piston velocity as expected.

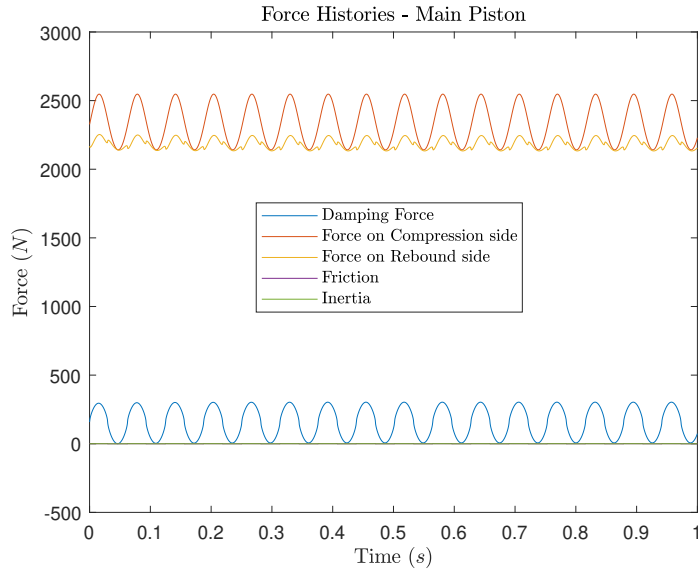


Figure 8.9: Force histories for oscillation at 100 Hz

It is observed that the inertia and friction forces are significantly lower than the forces due to oil pressure on either side of the piston which contribute the majority of the damping force.

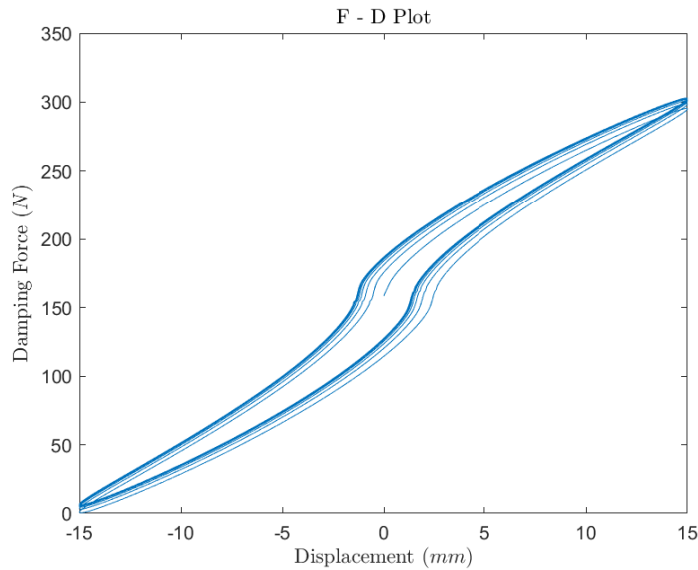


Figure 8.10: Force - Displacement plot for oscillation at 100 Hz

8.3.2 Comments on Simulink Model Results

The Simulink model was set up to simulate the experimental tests conducted on the test damper. The mathematical model, however, did not converge to a solution. The pressure in the compression chamber was found to increase exponentially while rebound chamber pressure remained relatively constant. This is contrary to damper physics. As noted by Talbott, it is the compression chamber pressure that must remain relatively constant while the damping force is generated due to variations in the rebound chamber pressure (Talbott and Starkey [1]).

Due to the high degree of coupling within the model, it is not a straight forward task to isolate the source of the perturbation. In addition, the source may not be an error in the mathematical model itself, but a singularity with the numerical values of the parameters or the solution scheme itself. The failure of this model to reach a solution requires investigation since a transient model such as this one is critical to implement dynamic model coefficients, study hysteresis or even test hardware-in-loop control.

8.4 MATLAB Model Results

8.4.1 Model Output

The MATLAB model was run for a sinusoidal forcing amplitude of 15 mm at a frequency of 25 Hz with a completely open bleed valve and the results are as shown below:

The displacement and velocity histories are plotted below in Fig. 8.11 and Fig. 8.12 respectively:

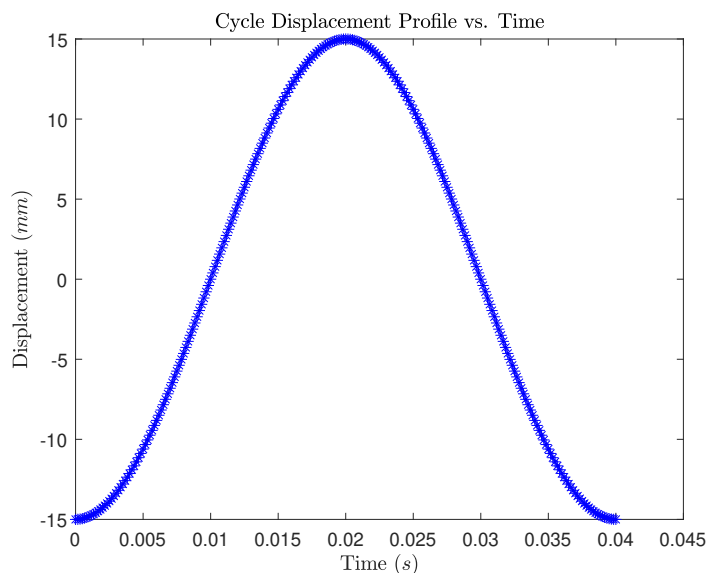


Figure 8.11: Displacement History for sinusoidal input of 25 Hz

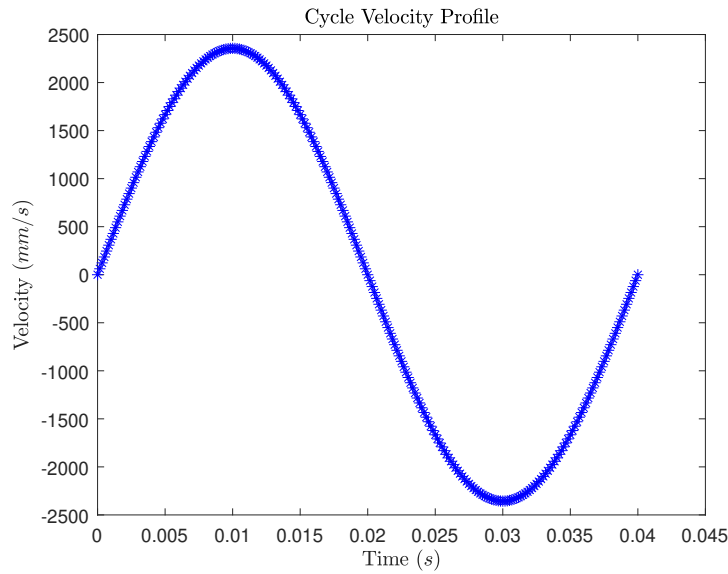


Figure 8.12: Velocity History for sinusoidal input of 25 Hz

The piston is observed to attain a velocity of approximately 2.5 m/s during its stroke of 15 mm

Plots of damping force as a function of piston velocity and piston displacement are displayed below in Fig. 8.13 and Fig. 8.14 respectively:

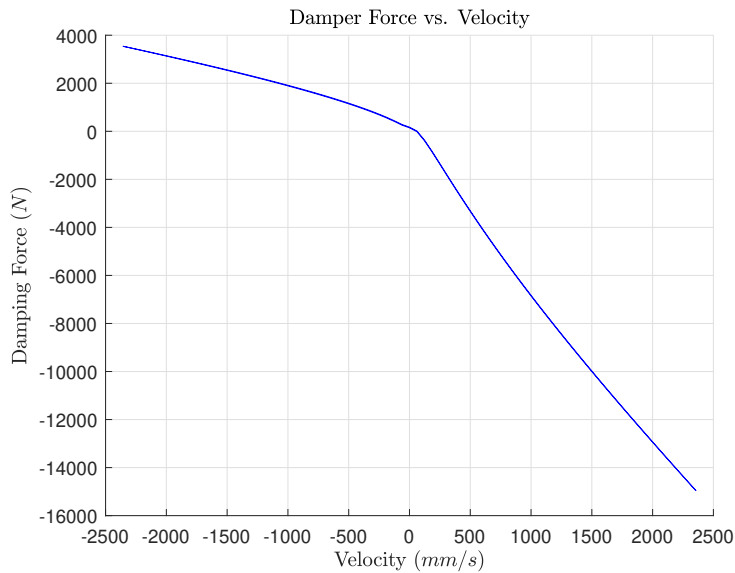


Figure 8.13: Damping Force vs. Piston Velocity for a sinusoidal input of 25 Hz

It must be noted that the maximum attainable rebound damping is determined by the pressure in the gas chamber. As the pressure in the rebound chamber tends to reach 0, cavitation occurs. The operational range of rebound chamber pressure and hence, the maximum rebound damping is therefore determined by the pressure in the gas chamber.

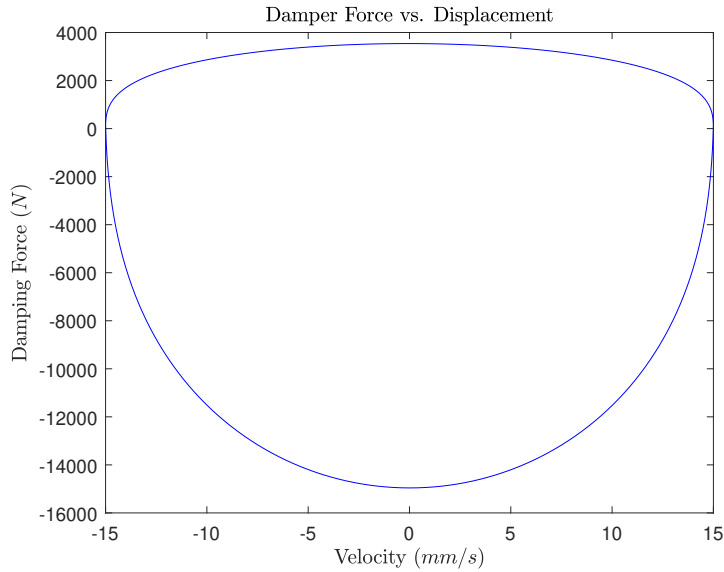


Figure 8.14: Damping Force vs. Piston Displacement for a sinusoidal input of 25 Hz

The Force-Velocity and Force-Displacement curves show an expected profile. The Force-Velocity trend is fairly linear with the knee region around the zero velocity point caused due to the dominance of bleed orifice flow. In the high speed regions, the flow is predominantly through the shim valves and a linear trend is resumed. A plot of all the volumetric flow rates as a function of piston velocity is shown below in Fig. 8.15:

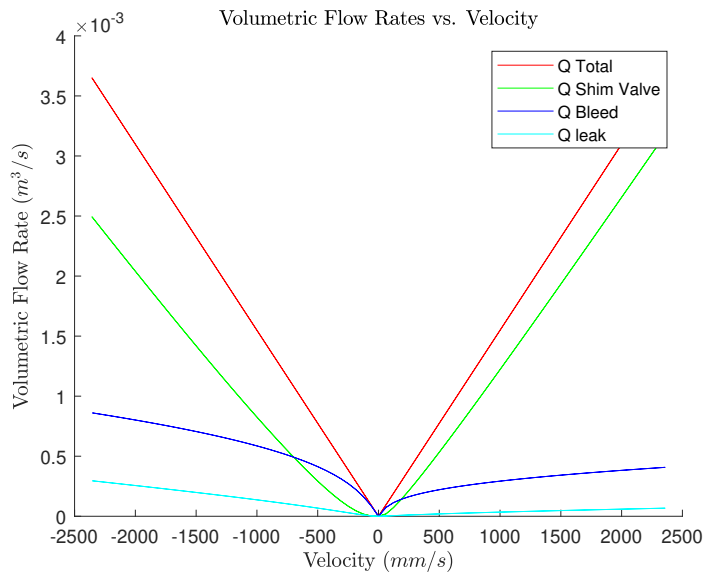


Figure 8.15: Volumetric Flow Rates vs. Piston Velocity for a sinusoidal input of 25 Hz

The trend of the total flow rate with piston velocity is nearly linear as expected, due to the large effect of the shim valve flow path. The shim valve flow rate is linear with piston velocity, as is intended for the tested damper. The bleed flow path shows non-linear

8.4. MATLAB MODEL RESULTS

behaviour, acting heavily around the zero velocity region but quickly reaching asymptotic behaviour away from the zero velocity region. The behaviour of the piston seal leakage is observed to be linear as well, as can be expected from equation 3.16.

A plot of all the pressures as a function of piston velocity is shown below in Fig. 8.16:

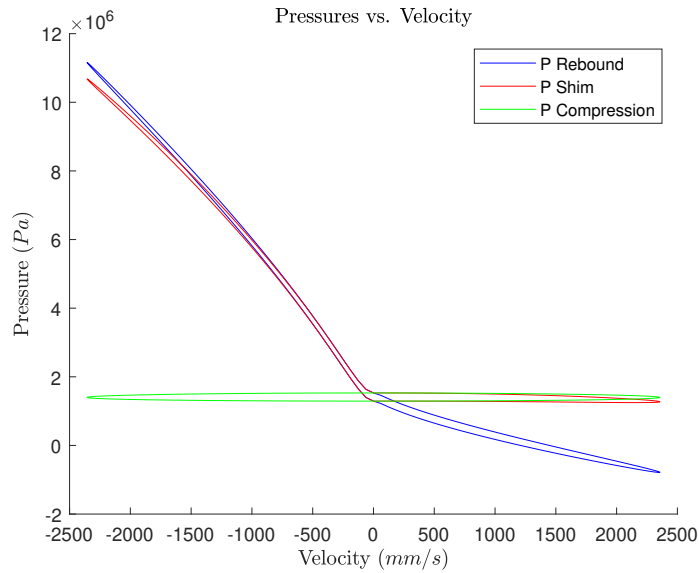


Figure 8.16: Pressures vs. Piston Velocity for a sinusoidal input of 25 Hz

It is observed that the compression pressure remains relatively constant throughout both strokes and it is the changes in rebound pressure that are the primary cause of pressure differentials across the piston and hence generation of the damping force. A similar observation was made by Talbott and Starkey [1]. In addition, it is noted that the pressure at the shim valve surface approximately matches the pressure in the chamber upstream of the valve.

8.4.2 Sensitivity Analysis

In order to study the effect of the various model parameters on damper performance, sensitivity studies were carried out. The studies were performed with a closed bleed valve in order to minimise sources of error. The MATLAB model was used to simulate the velocities openings that the physical damper was subjected to, as described in Section 7.4 and the following parameters were varied:

1. Opening Radius - 10 mm–16 mm (refer Fig. 3.3)
2. Initial Gas Chamber Pressure - 10 bar–20 bar
3. Shim Valve Discharge Coefficient - 0.5–1.0
4. Shim Stack Stiffnesses - Factor of 0.5x - 1.5x applied to the stiffness obtained from the force method

The baseline values for these parameters were as follows:

- Opening radius = 16 mm for both shim stacks
- Initial Gas Chamber Pressure = 14 bar
- Shim Valve Discharge Coefficient = 0.7
- Shim Stack Stiffnesses as determined by the Force method (refer 8.3)

The plot of Damping Force vs. Velocity for the baseline configuration is as shown below in Fig. 8.17:

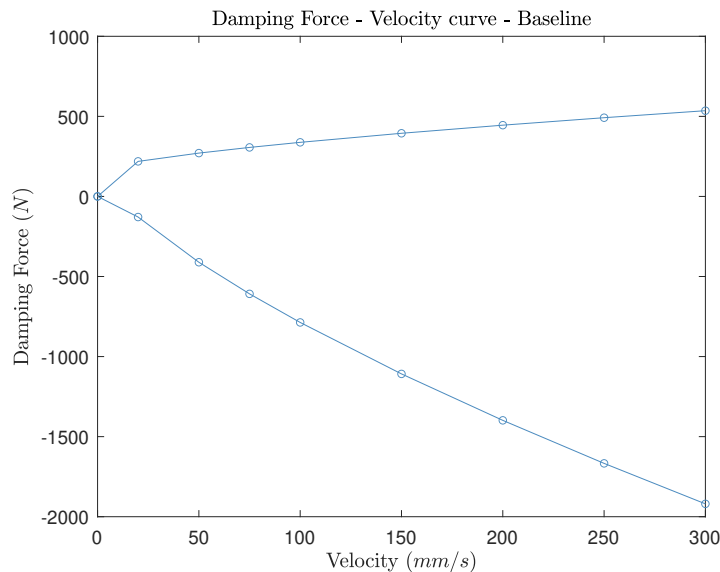


Figure 8.17: Damping Force vs. Velocity plot for the Baseline configuration used for sensitivity analysis

Obtained Damping Force vs. Velocity curves are shown below from Fig. 8.18 to 8.21

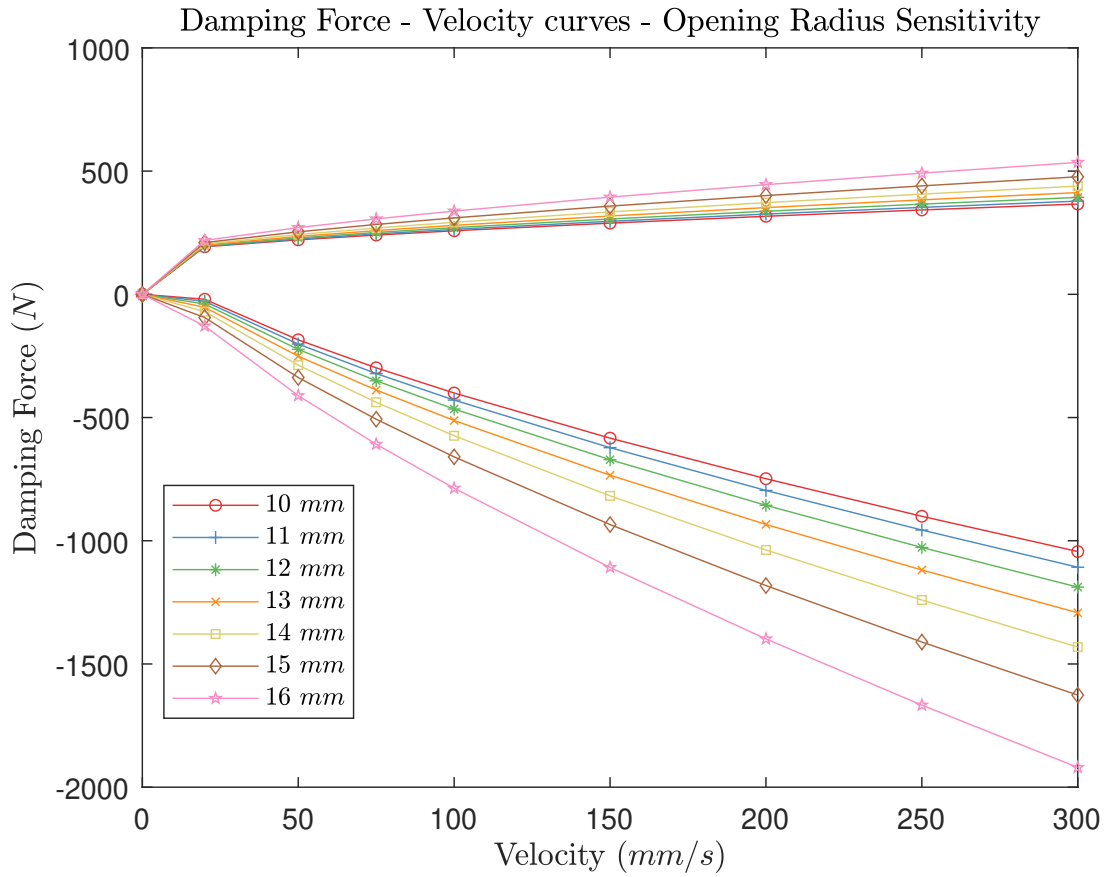


Figure 8.18: Damping Force vs. Velocity plots for sensitivity analysis of Opening Radius for Opening radius = 10 mm–16 mm for both shim stacks

The opening radius is observed to affect damper performance significantly in both compression and rebound strokes. The damping forces in both compression and rebound strokes and observed to increase with increasing opening radius.

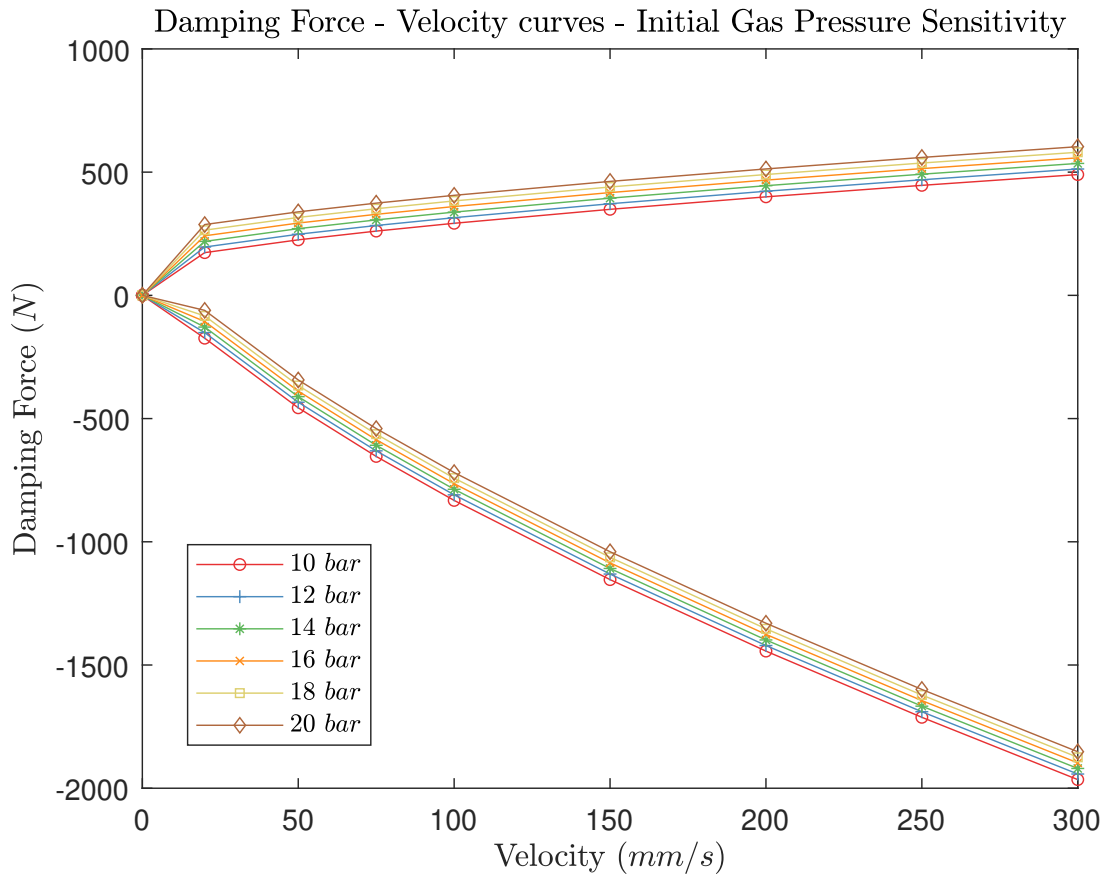


Figure 8.19: Damping Force vs. Velocity plots for sensitivity analysis of Initial Gas Chamber Pressure for Initial Gas Chamber Pressure = 10 bar–20 bar

The initial pressure in the gas chamber is found to have negligible effect on damper performance, thus the solitary role of the initial pressure in the gas chamber may be considered as being to avoid cavitation, with negligible spring effect.

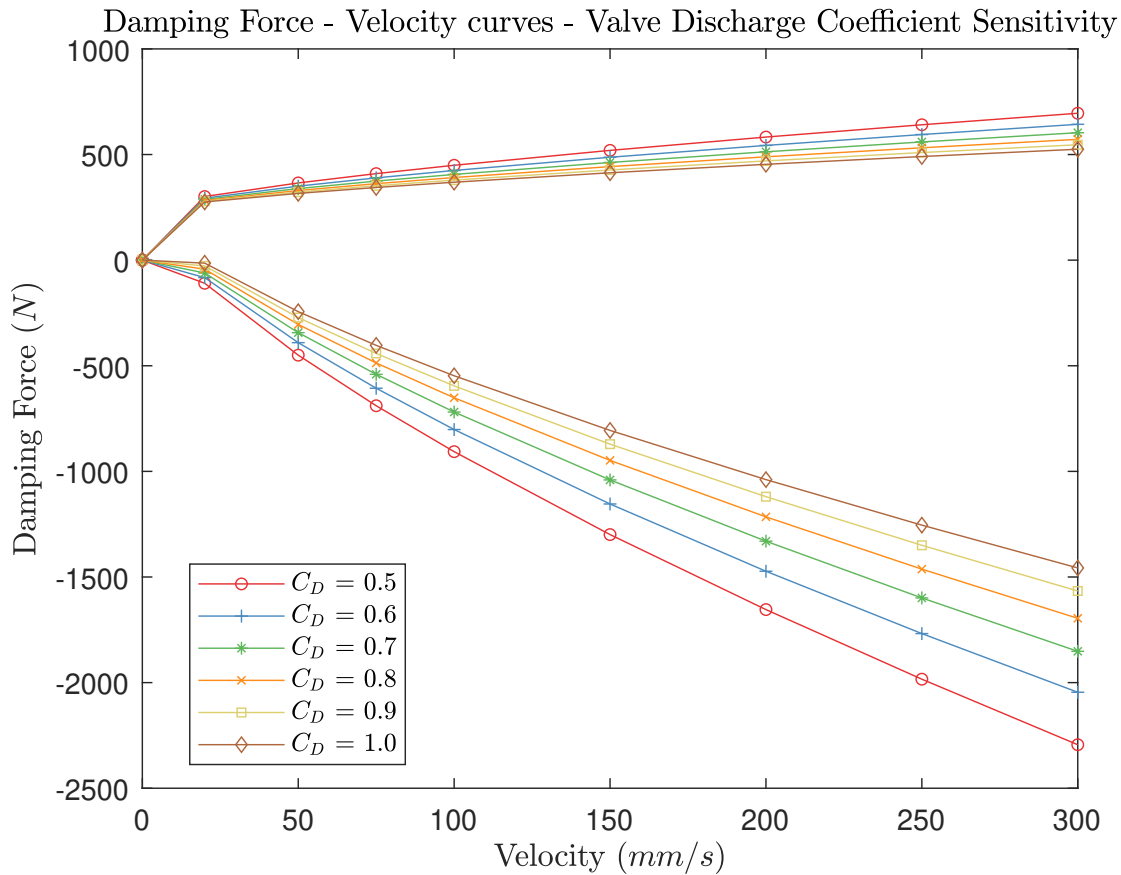


Figure 8.20: Damping Force vs. Velocity plots for sensitivity analysis of Shim Valve Discharge Coefficient for $C_D = 0.5-1.0$

The discharge coefficient is observed to affect damper performance significantly in both compression and rebound strokes. The discharge coefficient of both shim stacks in a damper are rarely equal. Hence, the effects need to be analysed independently for each stroke. The damping forces in both the compression and rebound strokes are observed to increase with decreasing discharge coefficients.

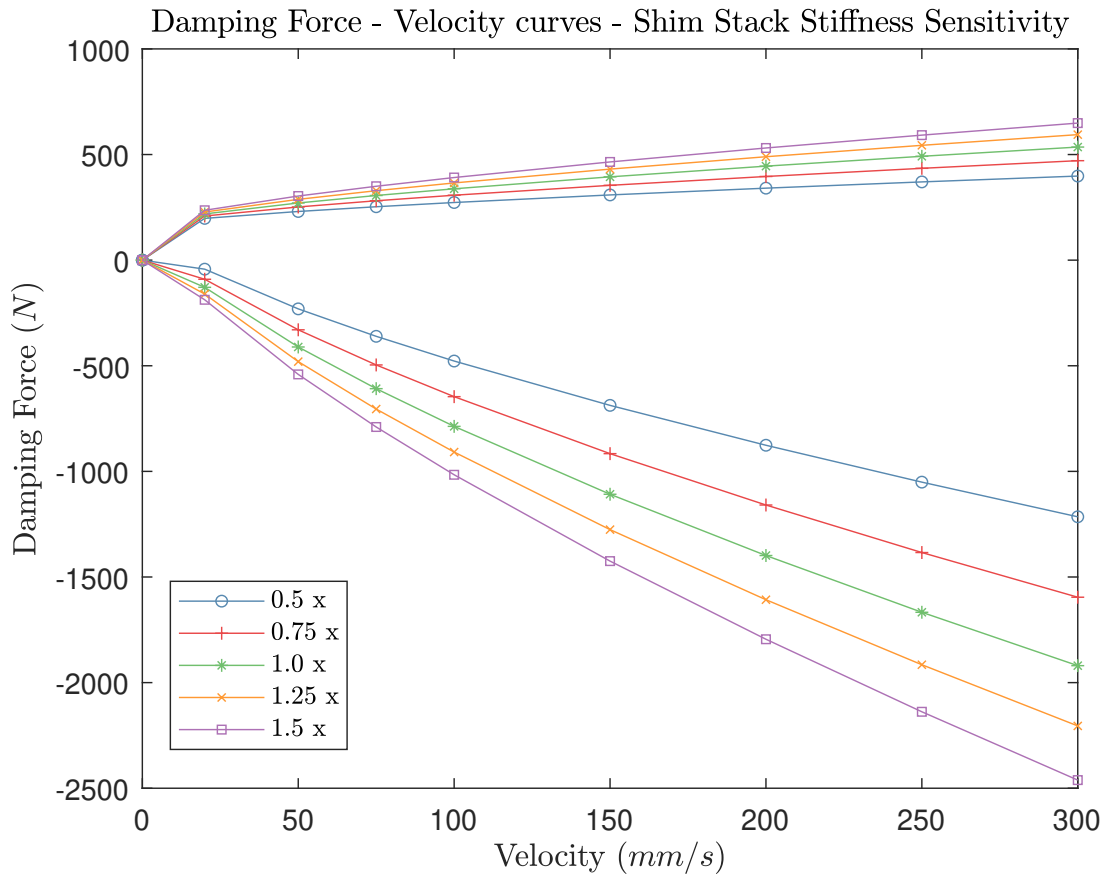


Figure 8.21: Damping Force vs. Velocity plots for sensitivity analysis of Shim Stack Stiffness for factors of 0.5x - 1.5x applied to the stiffness obtained from the force method

The stiffness of the shim stacks is observed to have the greatest effect among the tested parameters. The stiffness for both stacks are rarely equal. On the contrary, they may differ by up to an order of magnitude (refer Table 8.3). The damping forces in both the compression and rebound strokes are observed to increase with increasing shim stack stiffness. The effect of stiffness is more apparent than the other parameters for the chosen ranges of variation.

Discussion of Results from Sensitivity Analysis

- An increase in opening radius reduces the area of the shim exposed to the orifice flow, thus giving a reduced actuating force for the same upstream pressure. This reduced force leads to a lower deflection and a greater resistance to flow, resulting in increased damping force in both the compression and rebound strokes.
- An increase in damping force on decrease of the shim valve discharge coefficient is as expected, since a valve with a low discharge coefficient provides a greater resistance to flow, thus allowing a larger pressure differential to develop between the two sides of the piston.

- An increase in damping force with an increase in shim stack stiffness is as expected, since a stiffer stack will exhibit a lower deflection for the same applied pressure load, thus providing resistance to the flow and enabling the development of a larger pressure differential across the piston.

8.4.3 Results of Numerical Simulations of the Tests

The MATLAB model was used to simulate the velocities and bleed openings that the physical damper was subjected to, as described in Section 7.4. A value of 0.5 was chosen as an estimate of the discharge coefficient of the shim valves for both strokes based on data obtained in Section 8.4.2. A value of 0.7 was chosen as the discharge coefficient for the bleed valve, as suggested by Rhoades [9]. The shim stiffnesses used were as reported in Table 8.3. The results of these simulations are shown below: The damping force vs. velocity plots for all bleed positions are shown below in Fig. 8.22:

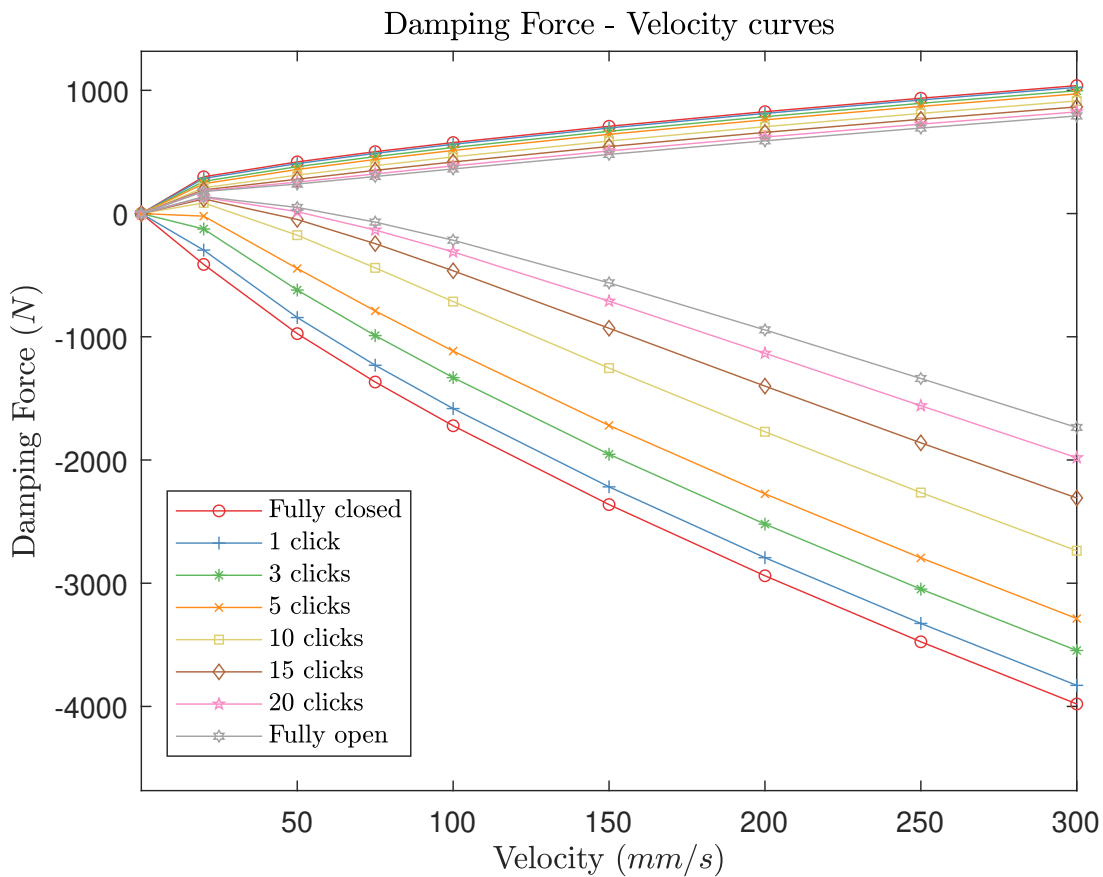


Figure 8.22: Force - Velocity curves for numerical simulations of the test points

Damping force vs displacement curves for all bleed positions are shown below in Figs. 8.23 to 8.28

8.4. MATLAB MODEL RESULTS

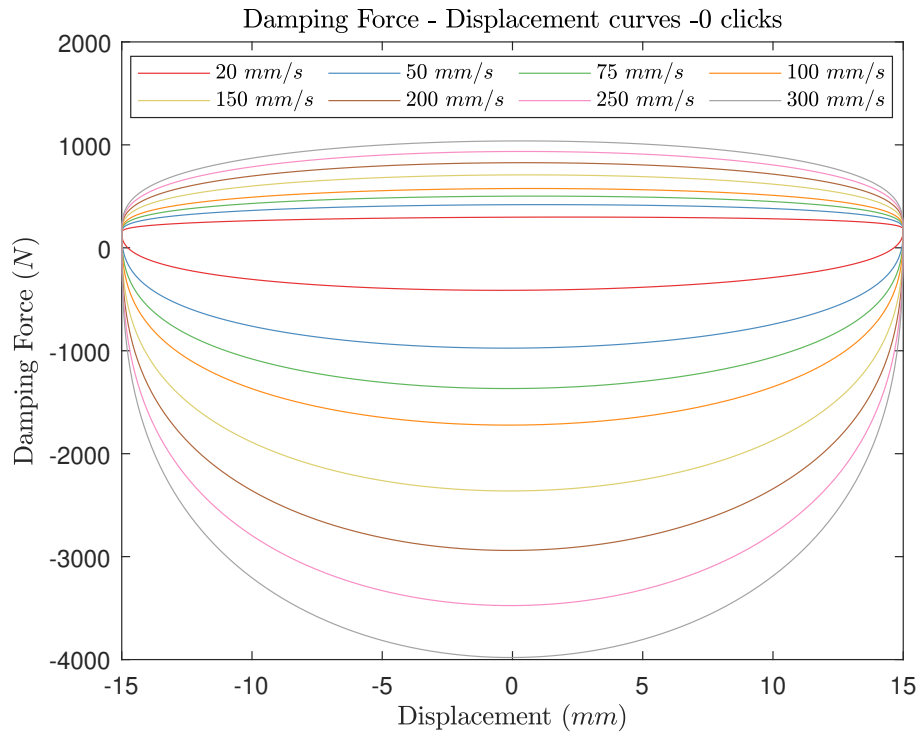


Figure 8.23: Force - Displacement curves for Bleed Fully Closed

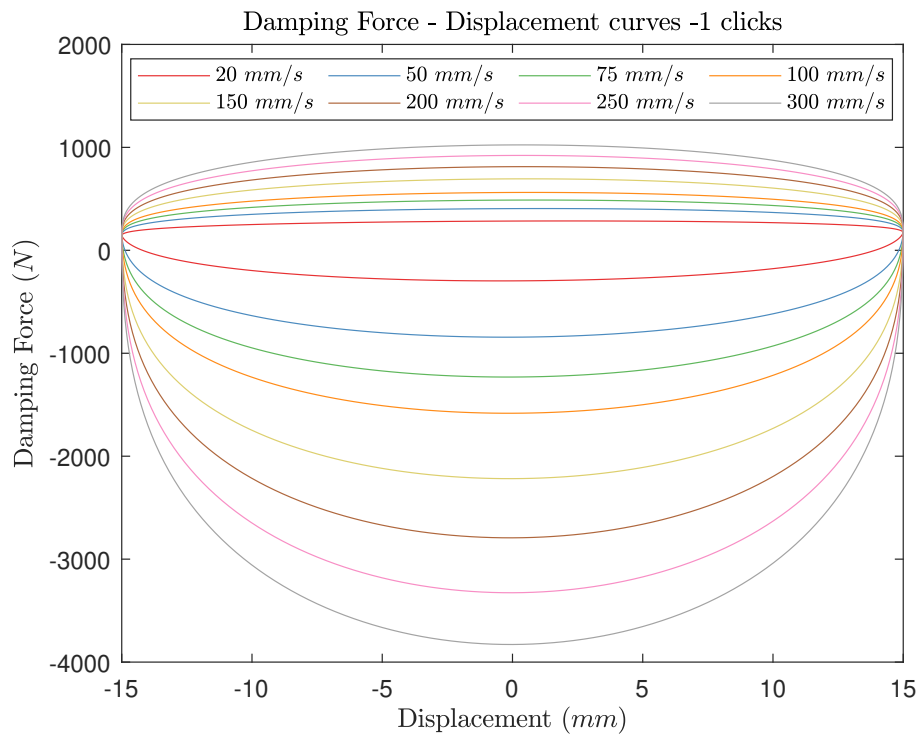


Figure 8.24: Force - Displacement curves for Bleed at 1 click

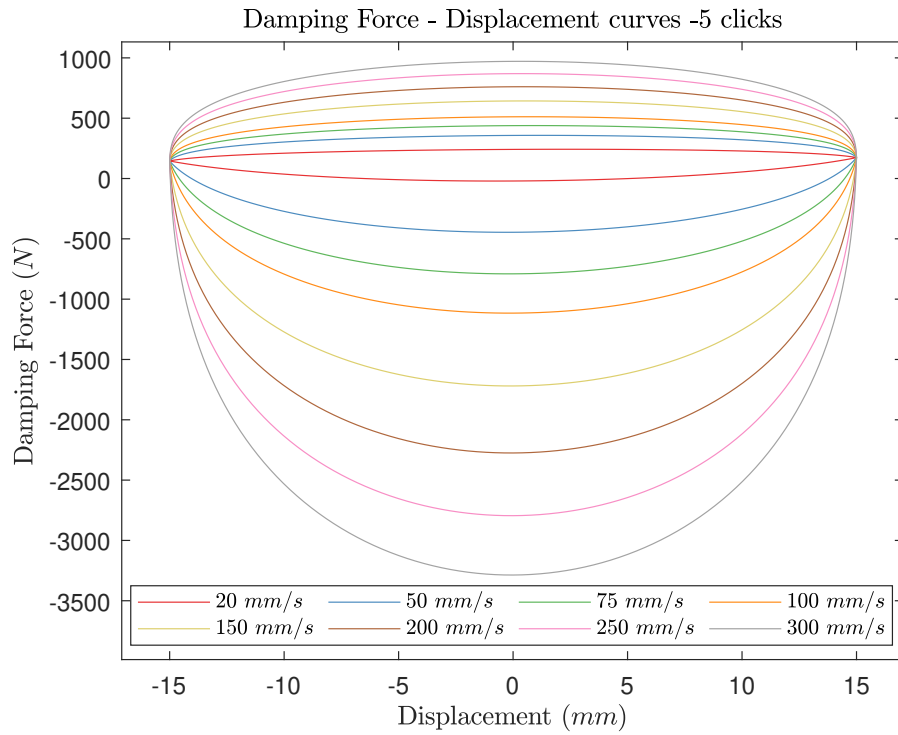


Figure 8.25: Force - Displacement curves for Bleed at 5 clicks

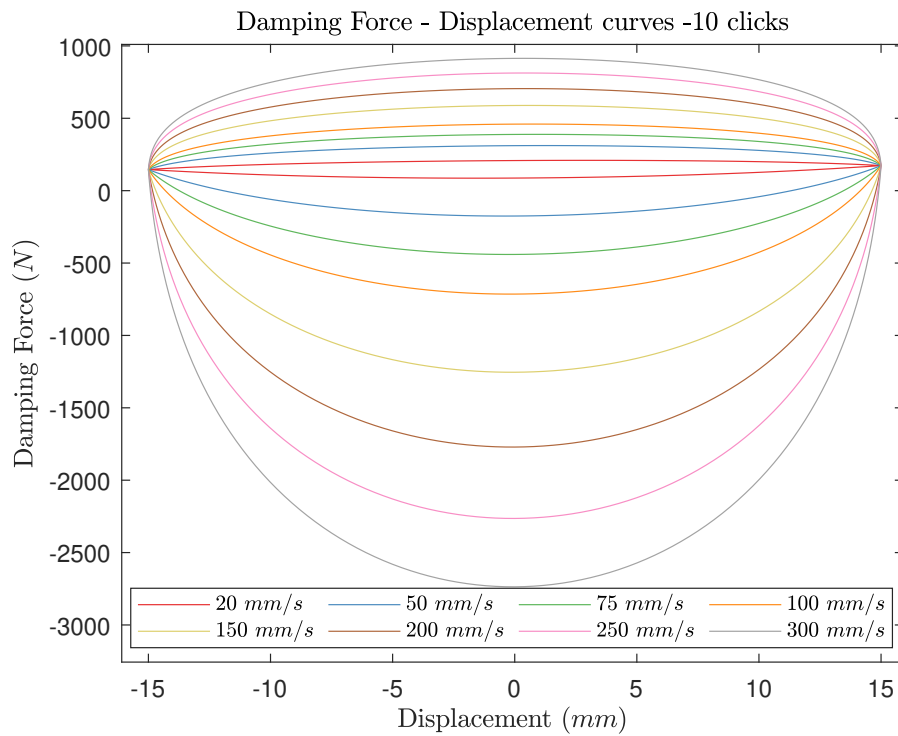


Figure 8.26: Force - Displacement curves for Bleed at 10 clicks

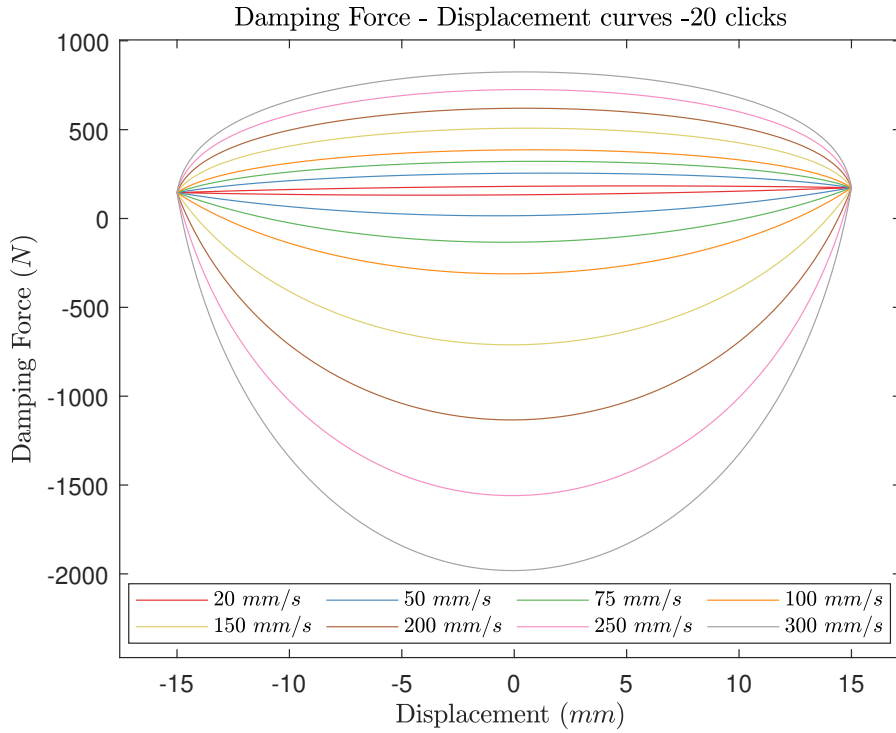


Figure 8.27: Force - Displacement curves for Bleed at 20 clicks

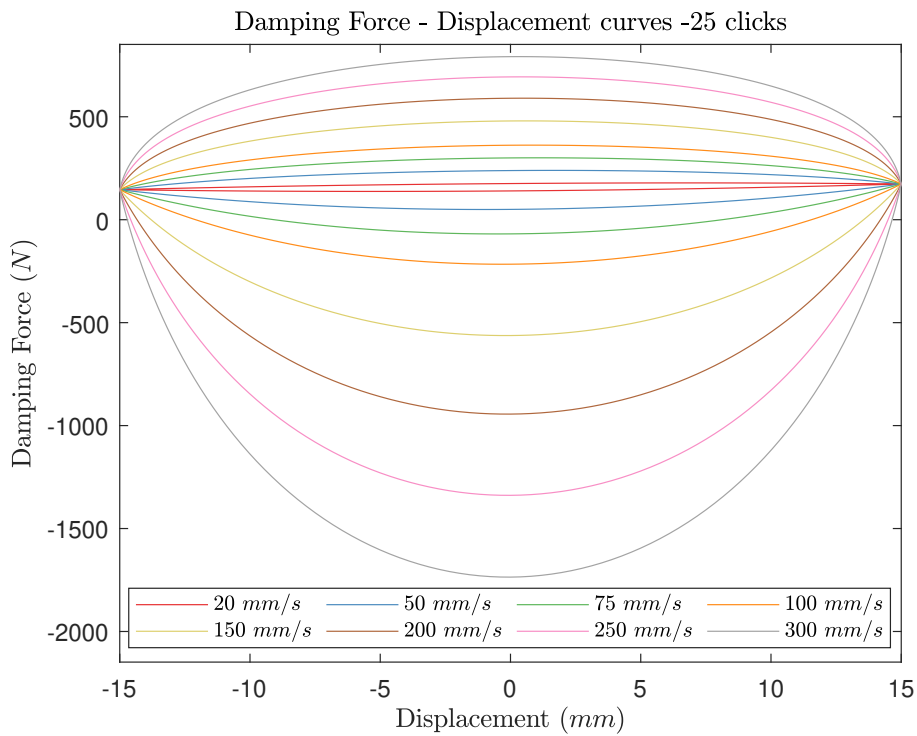


Figure 8.28: Force - Displacement curves for Bleed Fully Open

8.5 Comparison of Experimental Results with Mathematical Model

The results of the mathematical model were compared with experimental values. The mathematical model was run with the following values of the salient model coefficients:

Parameter	Value
$C_{D_{valve}}$	0.5
$C_{D_{bleed}}$	0.7
Shim Stiffnesses	As per Force method (Table. 8.3)

Table 8.4: Model coefficients used in numerical simulations of the tests

8.5.1 Force-Velocity Plots

Figures 8.29 to 8.36 display the comparison of Damping Force vs. Velocity data for all tested bleed orifice openings:

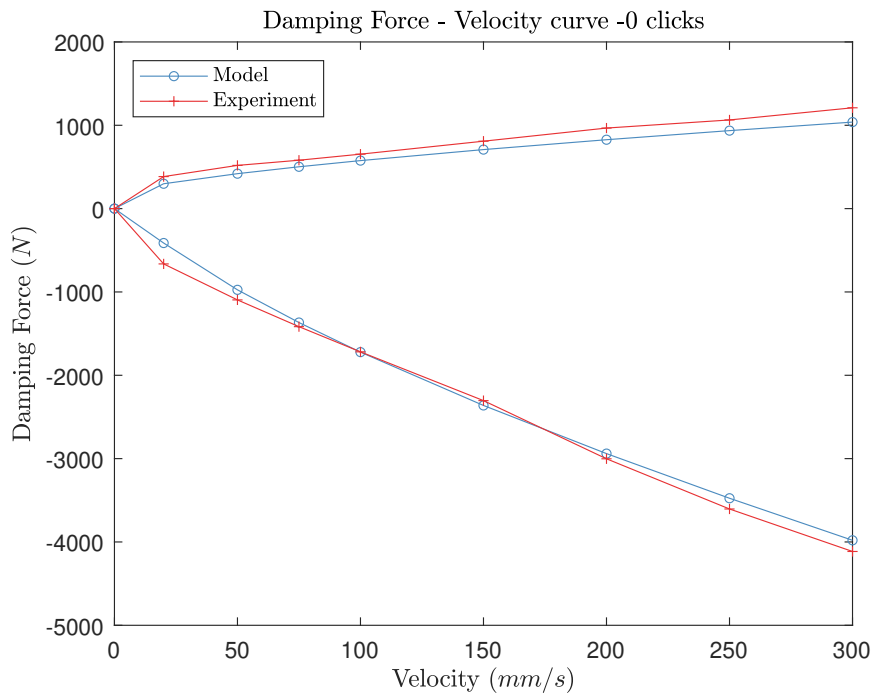


Figure 8.29: Comparison of Force - Velocity curves from experiment and the developed mathematical model for Bleed Fully Closed

8.5. COMPARISON OF EXPERIMENTAL RESULTS WITH MATHEMATICAL MODEL

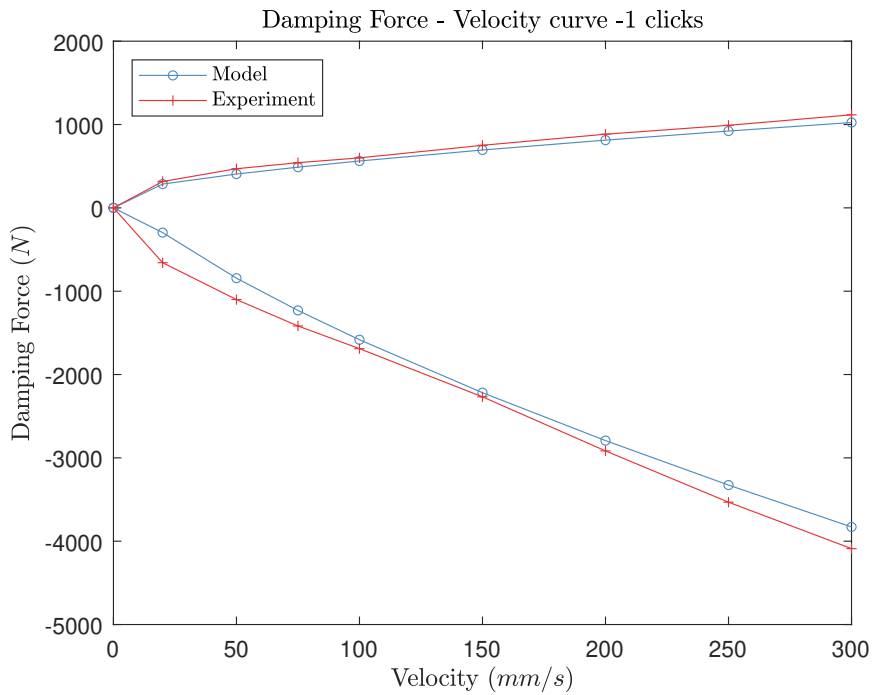


Figure 8.30: Comparison of Force - Velocity curves from experiment and the developed mathematical model for Bleed at 1 click

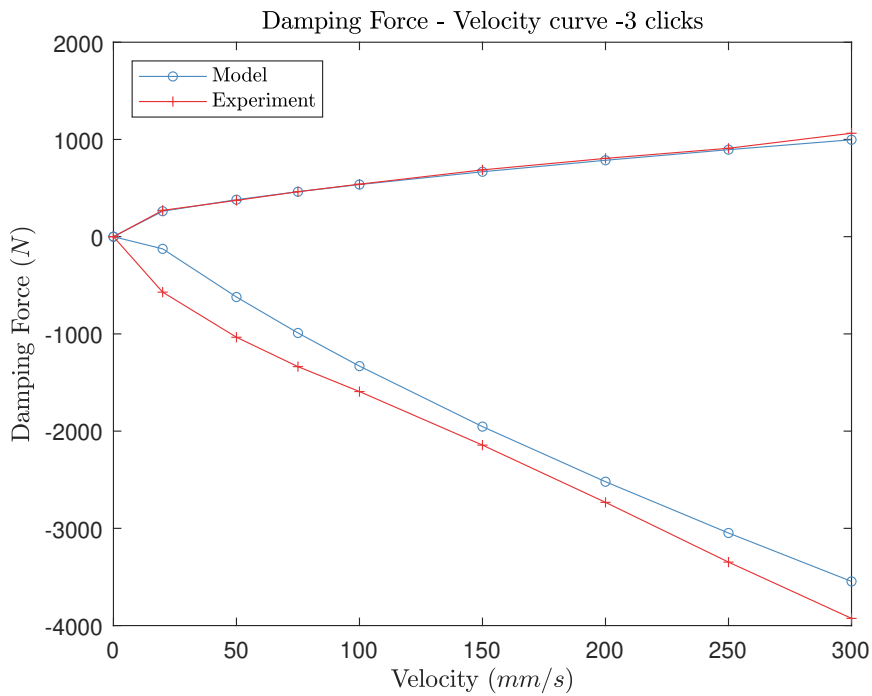


Figure 8.31: Comparison of Force - Velocity curves from experiment and the developed mathematical model for Bleed at 3 clicks

8.5. COMPARISON OF EXPERIMENTAL RESULTS WITH MATHEMATICAL MODEL

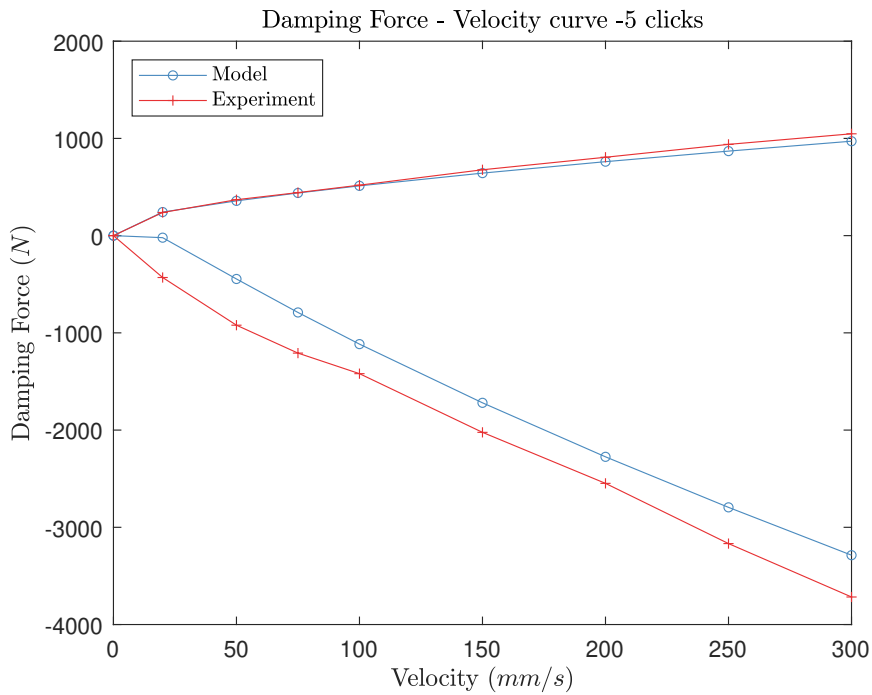


Figure 8.32: Comparison of Force - Velocity curves from experiment and the developed mathematical model for Bleed at 5 clicks

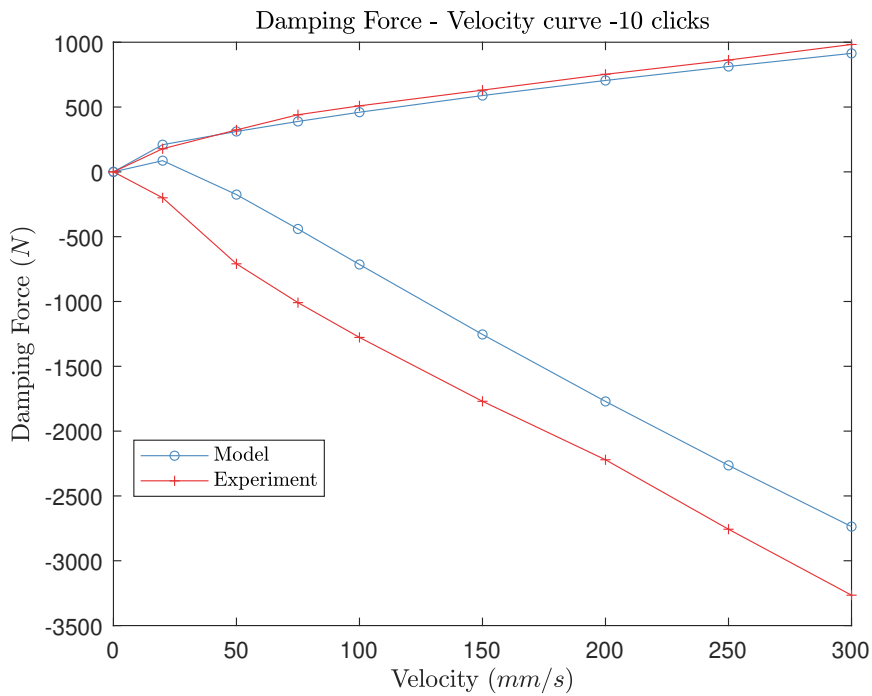


Figure 8.33: Comparison of Force - Velocity curves from experiment and the developed mathematical model for Bleed at 10 clicks

8.5. COMPARISON OF EXPERIMENTAL RESULTS WITH MATHEMATICAL MODEL

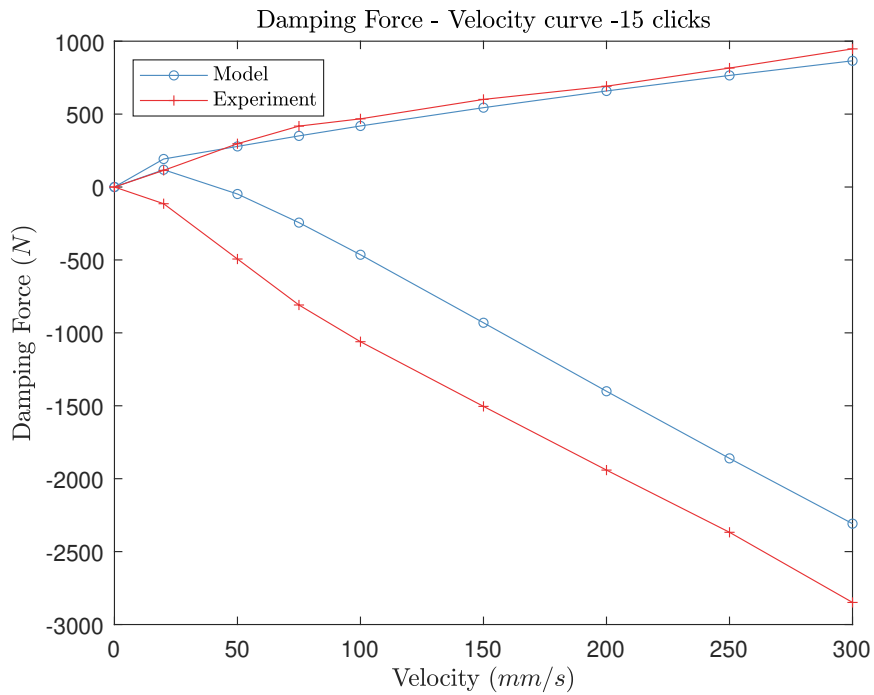


Figure 8.34: Comparison of Force - Velocity curves from experiment and the developed mathematical model for Bleed at 15 clicks

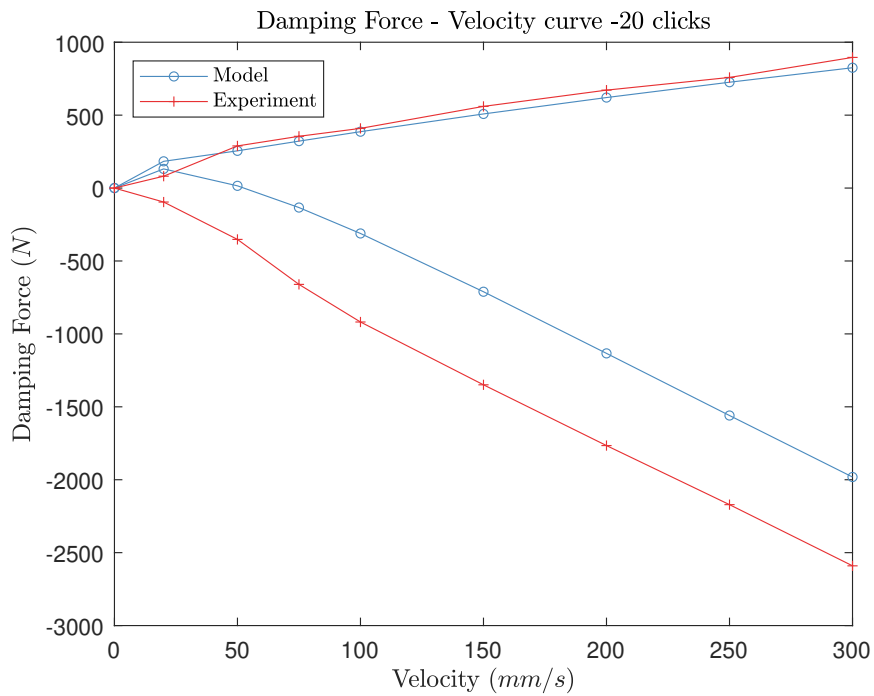


Figure 8.35: Comparison of Force - Velocity curves from experiment and the developed mathematical model for Bleed at 20 clicks

8.5. COMPARISON OF EXPERIMENTAL RESULTS WITH MATHEMATICAL MODEL

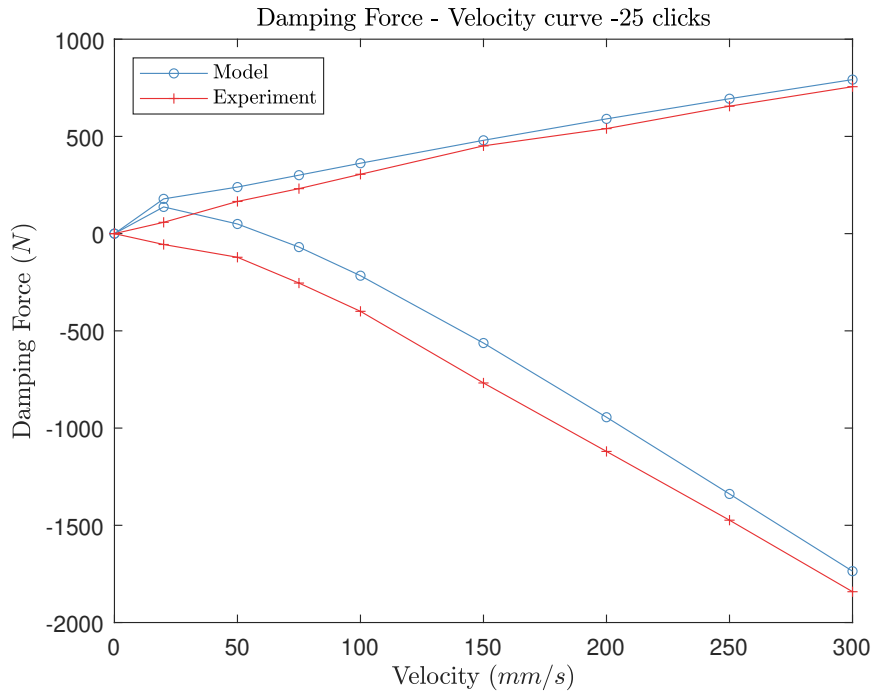


Figure 8.36: Comparison of Force - Velocity curves from experiment and the developed mathematical model for Bleed Fully Open

During experimental trials, the gas chamber pressure was measured and compared to numerical results. The plot for the bleed valve fully closed for a velocity of 20 mm/s are shown below in Fig. 8.37:

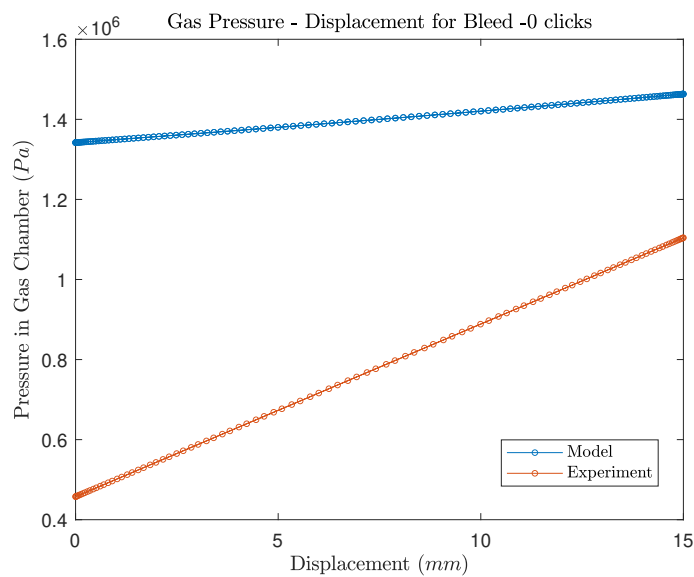


Figure 8.37: Comparison of Gas Chamber Pressure for Bleed Fully Closed

It is observed that the model computed pressure is higher than the experimental value. Also, there exists a difference in the trend of the gas chamber pressure with piston displacement.

8.5.2 Analysis

The developed mathematical model displays the same trend in force-velocity and force-displacement plots as the experimental data. This indicates that the physics have been modelled in a good manner. The difference in values may be attributed to lack of available data for the model coefficients, particularly discharge coefficients for both the bleed flow path and the shim flow path.

The model displays good agreement at low bleed valve openings and large discrepancies at high bleed valve openings, pointing to inaccuracies in the model of the bleed valve flow path. The area variation of the bleed orifice with the number of clicks as well as the discharge coefficient for the bleed flow path merit consideration. The model shows the best agreement with experimental data for the case of a fully closed bleed valve. It is also observed that good agreement is found at high velocities, suggesting good characterisation of the shim valve parameters, at least at low bleed valve openings. This suggests that further investigation is required in the modelling of the bleed and shim flow paths. Further CFD and FSI simulations are required in order to accurately model the flow through the shim valves, thus improving the accuracy of the mathematical model.

The comparison of gas chamber pressure data showed no variation with set velocity or bleed valve position. It must be noted that variations in measured gas chamber pressure are induced due to changes in temperature internally in the damper, which is a potential source of discrepancies, given that temperature differences either from standard chemical conditions nor temperature transients are accounted for in the mathematical model. It is observed that the mathematical model has a tendency to over-predict the pressure in the gas chamber, leading to an under-prediction of pressure in the rebound chamber. This behaviour is responsible for the anomalous positive damping forces at low velocities and high bleed valve openings as observed in Figs [8.36](#), [8.35](#), [8.34](#) and [8.33](#).

Conclusions and Recommendations

9.1 Conclusions

A parametric mathematical model was developed using MATLAB to model a generic monotube automotive damper. This mathematical model was compared to experimental results. The model displayed a good agreement in physical trend but requires further study to quantify the model parameters in order to improve the model accuracy. In the absence of FSI-generated data for the tested damper, constant values were used and compared against experimental results.

An attempt was made to study the internal flow field and shim valve dynamics using Fluid-Structure Interaction (FSI) simulations in order to quantify discharge coefficients. Initial trials of FSI simulations using the OpenFOAM-preCICE-CalculiX combination showed promising results. This solver combination showed good agreement with experimental results when used to simulate a cylinder-plate geometry. Trials performed on a single orifice and shim geometry showed expected results. With the inclusion of contact modelling and with sufficient computational power, FSI simulations could be the optimal methodology to measure discharge coefficients and to characterise shim stack behaviour, given the high costs involved in performing experiments for these parameters and the over-simplification of currently used analytical models.

One of the greatest challenges to improving the mathematical model is the lack of experimental data of the principal parameters. Since damper development has been mostly empirical in nature, experiments have sought to measure solely the damping force, thus denying the insight into the validity and accuracy of the individual sub-models. Performing experiments that provide data on operational variables will greatly enhance the accuracy and hence applicability of mathematical models such as the one presented in this work.

9.2 Recommendations

Due to paucity of time, further development and improvement in the models could not be carried out. However, these considerations will remain as recommendations for future work:

- **Detailed FSI simulations** - The strong coupling between the flow field and shim deflection is evident throughout this work and two-way coupled simulations will provide a much better understanding of the dynamics of this coupling, compared to one-way coupled analytical models.
- **Pressure transducers** - The model coefficients have been modelled primarily in terms of compression and rebound pressures and performing experiments on dampers instrumented with pressure transducers will enable better modelling of these coefficients as well as provide insight into the sources of error in the model.
- **Transparent dampers** - In order to better understand the structural dynamics of the shim stack, it is recommended to perform experiments with transparent dampers and high speed cameras. This information may be then used to improve analytical models.
- **Detailed analysis of the bleed flow path** - The bleed orifice flow path plays a crucial role in damper operation. In this work, no simulations were performed on this flow path. It is recommended to study the flow dynamics of the bleed orifice to improve the fidelity of the damper model.
- **Hysteresis Modelling** - Hysteresis plays a very important role in damper performance and hence merits modelling. This would however require implementation of a transient model with dynamic model coefficients. In addition to analysis hysteresis of the damper system as a whole, it is recommended to also investigate the hysteresis of the shim valves themselves.
- **Neural Networks** - Neural networks may be used to model complex phenomena such as compressibility effects based on experimental data, as done by Barethiye et al. [43]. In addition, neural networks may be used to improve interpolation between the model data points, resulting in a better resolved model.
- **Quarter Car Model Integration** - The damper model may be integrated with a quarter car or motorcycle dynamic model in order to simulate vehicle dynamical behaviour.

Bibliography

- [1] Michael S. Talbott and John Starkey. An experimentally validated physical model of a high-performance mono-tube damper. *Proceedings of the 2002 SAE Motorsports Engineering Conference and Exhibition*, 3337(01):382, 12 2002. ISSN 0148-7191. doi: 10.4271/2002-01-3337. URL <https://doi.org/10.4271/2002-01-3337>.
- [2] Paulius Skačkauskas, Vidas Žuraulis, Vaidas Vadluga, and Saulius Nagurnas. Development and verification of a shock absorber and its shim valve model based on the force method principles. *Eksploatacja i Niezawodność - Maintenance and Reliability*, 19:126–133, 12 2016. doi: 10.17531/ein.2017.1.18.
- [3] Gerasimos Chourdakis. *A general OpenFOAM adapter for the coupling library pre-CICE*. PhD thesis, Technical University of Munich, 10 2017.
- [4] John C. Dixon. *The Shock Absorber Handbook, 2nd Edition*. John Wiley & Sons, Sussex, West Sussex, Oxford, England, 2007. ISBN 978-0-470-51020-9.
- [5] Koni. <http://www.koni.com/en-US/Cars/Technology/Working-Principles/>, 2021. [Accessed February 25th, 2021].
- [6] Nitin Satpute, Shankar Singh, and Suresh Sawant. Fluid flow modelling of a fluid damper with shim loaded relief valve. *International Journal of Mechanical Engineering*, 2:65–74, 01 2013. ISSN 2319-2240.
- [7] Shimrestackor. <http://www.shimrestackor.com/index.htm>, 2021. [Accessed February 25th, 2021].
- [8] Koenraad Reybrouck. A non linear parametric model of an automotive shock absorber. In *SAE Technical Paper*. SAE International, 03 1994. doi: 10.4271/940869. URL <https://doi.org/10.4271/940869>.
- [9] Kirk Shawn Rhoades. Development and experimental verification of a parametric model of an automotive damper. In *Development and experimental verification of a parametric model of an automotive damper*, 2006.
- [10] Tommy Nilsson. 2-way fsi simulations on a shock absorber check valve. Master’s thesis, KTH, Mechanics, 2014.
- [11] Ansys. <https://www.ansys.com/>, 2021. [Accessed February 25th, 2021].
- [12] Piotr Czop, Damian Sławik, Śliwa P, and Grzegorz Wszolek. Simplified and advanced models of a valve system used in shock absorbers. *Journal of Achievements in Materials and Manufacturing Engineering*, 33, 2009.
- [13] Alireza Farjoud, Mehdi Ahmadian, Michael Craft, and William Burke. Nonlinear modeling and experimental characterization of hydraulic dampers: Effects of shim stack and orifice parameters on damper performance. *Nonlinear Dynamics*, 67, 06 2012. doi: 10.1007/s11071-011-0079-2.

BIBLIOGRAPHY

- [14] R.G. Budynas and A.M. Sadegh. *Roark's Formulas for Stress and Strain, 9E*. McGraw-Hill Education, 2020. ISBN 9781260453768. URL https://books.google.se/books?id=dE_VDwAAQBAJ.
- [15] Matlab. <https://it.mathworks.com/products/matlab.html>, 2021. [Accessed February 25th, 2021].
- [16] Simulink. <https://it.mathworks.com/products/simulink.html>, 2021. [Accessed February 25th, 2021].
- [17] Singiresu S. Rao. Chapter 1 - overview of finite element method. In Singiresu S. Rao, editor, *The Finite Element Method in Engineering (Fifth Edition)*, pages 3–50. Butterworth-Heinemann, Boston, fifth edition edition, 2011. ISBN 978-1-85617-661-3. doi: <https://doi.org/10.1016/B978-1-85617-661-3.00001-5>. URL <https://www.sciencedirect.com/science/article/pii/B9781856176613000015>.
- [18] Henk Kaarle Versteeg and Weeratunge Malalasekera. *An introduction to computational fluid dynamics - the finite volume method*. Addison-Wesley-Longman, 1995. ISBN 978-0-582-21884-0.
- [19] Tayfun E. Tezduyar Yuri Bazilevs, Kenji Takizawa. *Governing Equations of Fluid and Structural Mechanics*. John Wiley & Sons, Ltd, 2013. ISBN 9781118483565. doi: <https://doi.org/10.1002/9781118483565.ch1>. URL <https://onlinelibrary.wiley.com/doi/abs/10.1002/9781118483565.ch1>.
- [20] Sang Truong Ha, Long Cu Ngo, Muhammad Saeed, Byoung Jin Jeon, and Hyoungwon Choi. A comparative study between partitioned and monolithic methods for the problems with 3d fluid-structure interaction of blood vessels. *Journal of Mechanical Science and Technology*, 31(1):281–287, Jan 2017. ISSN 1976-3824. doi: [10.1007/s12206-016-1230-2](https://doi.org/10.1007/s12206-016-1230-2). URL <https://doi.org/10.1007/s12206-016-1230-2>.
- [21] Alexander Lozovskiy, Maxim A Olshanskii, and Yuri V Vassilevski. Analysis and assessment of a monolithic FSI finite element method. *Computers & Fluids*, 179:277–288, 2019. ISSN 0045-7930. doi: <https://doi.org/10.1016/j.compfluid.2018.11.004>. URL <https://www.sciencedirect.com/science/article/pii/S0045793018308491>.
- [22] Serge Piperno. Design of efficient partitioned procedures for the transient solution of aeroelastic problems. *Revue Europeenne des Elements*, 9, 01 2000. doi: [10.1080/12506559.2000.10511480](https://doi.org/10.1080/12506559.2000.10511480).
- [23] Matthias Heil, Andrew Hazel, and Jonathan Boyle. Solvers for large-displacement fluid-structure interaction problems: Segregated versus monolithic approaches. *Computational Mechanics*, 43:91–101, 12 2008. doi: [10.1007/s00466-008-0270-6](https://doi.org/10.1007/s00466-008-0270-6).
- [24] Comsol. <https://www.comsol.com/>, 2021. [Accessed February 25th, 2021].
- [25] Adina. <http://www.adina.com/>, 2021. [Accessed February 25th, 2021].
- [26] Leon Leventhal. Cae applications in hydraulics - experimental and analytical study of a check-valve. In *SAE Technical Paper*. SAE International, 05 2003. doi: [10.4271/2003-01-1605](https://doi.org/10.4271/2003-01-1605). URL <https://doi.org/10.4271/2003-01-1605>.

BIBLIOGRAPHY

- [27] Stefano Ghelardi, Cesare Rizzo, and Diego Villa. Three-dimensional fluid-structure interaction case study on cubical fluid cavity with flexible bottom. *Journal of Marine Science and Application*, 16(4):382–394, 2017. ISSN 1993-5048. doi: 10.1007/s11804-017-1433-7. URL <https://doi.org/10.1007/s11804-017-1433-7>.
- [28] Mohamed Salim Ramadan and Sorawan Saichua. Fluid-structure interaction analysis for hydrodynamic parameters in semi-submerged axisymmetric buoy. Master’s thesis, , School of Engineering, 2010.
- [29] Han Yeh, Dana Grecov, and Satya Karri. Computational modelling of bileaflet mechanical valves using fluid-structure interaction approach. *Journal of Medical and Biological Engineering*, 34:482–486, 01 2014. doi: 10.5405/jmbe.1699.
- [30] P. C. Gomes. Numerical study of 2-d rigid and deformable fluid-structure interaction cases. In *Numerical Study of 2-D Rigid and Deformable Fluid-Structure Interaction Cases*, 2014.
- [31] Mehrzad Shams, Ebrahimi Reza, Arman Raoufi, and Behdad Jalali-Jafari. Cfd-fea analysis of hydraulic shock absorber valve behavior. *International Journal of Automotive Technology*, 8:615–622, 10 2007.
- [32] Derek Risseuw. *Fluid Structure Interaction Modelling of Flapping Wings*. PhD thesis, TU Delft, 01 2019.
- [33] Henry Weller. Openfoam. <https://www.openfoam.com/>, 1989. [Accessed February 25th, 2021].
- [34] simplefoam. <https://www.openfoam.com/documentation/guides/latest/doc/guide-applications-solvers-incompressible-simpleFoam.html>, 2021. [Accessed February 25th, 2021].
- [35] pimplefoam. <https://www.openfoam.com/documentation/guides/latest/doc/guide-applications-solvers-incompressible-pimpleFoam.html>, 2021. [Accessed February 25th, 2021].
- [36] Calculix. <http://www.calculix.de/>, 2021. [Accessed February 25th, 2021].
- [37] Lucía Cheung Yau. Conjugate heat transfer with the multiphysics coupling library precice. In *Conjugate Heat Transfer with the Multiphysics Coupling Library preCICE*, 2016.
- [38] Benjamin Uekermann, H. Bungartz, Lucia Cheung Yau, Gerasimos, Chourdakis, and A. Rusch. Official precice adapters for standard open-source solvers. In *Official preCICE Adapters for Standard Open-Source Solvers*, 2017.
- [39] precice coupling schemes. <https://www.precice.org/configuration-coupling.html>, 2021. [Accessed February 25th, 2021].
- [40] precice acceleration schemes. <https://www.precice.org/configuration-acceleration.html>, 2021. [Accessed February 25th, 2021].
- [41] Calculix convergence criteria. http://web.mit.edu/calculix_v2.7/CalculiX/ccx_2.7/doc/ccx/node144.html, 2021. [Accessed February 25th, 2021].

BIBLIOGRAPHY

- [42] Uk4kw. <https://umbriakinetics.com/>, 2021. [Accessed February 25th, 2021].
- [43] Vijay Barethiye, G. Pohit, and A. Mitra. A combined nonlinear and hysteresis model of shock absorber for quarter car simulation on the basis of experimental data. *Engineering Science and Technology, an International Journal*, 20(6):1610–1622, 2017. ISSN 2215-0986. doi: <https://doi.org/10.1016/j.jestch.2017.12.003>. URL <https://www.sciencedirect.com/science/article/pii/S2215098617308935>.